

EFFECT OF AGING ON THE MECHANICAL PROPERTIES OF BORON  
CARBIDE PARTICLE REINFORCED ALUMINUM METAL MATRIX  
COMPOSITES

A THESIS SUBMITTED TO  
THE GRADUATE SCHOOL OF NATURAL AND APPLIED SCIENCES  
OF  
MIDDLE EAST TECHNICAL UNIVERSITY

BY

MUSTAFA SERDAR KARAKAŞ

IN PARTIAL FULFILLMENT OF THE REQUIREMENTS  
FOR  
THE DEGREE OF DOCTOR OF PHILOSOPHY  
IN  
METALLURGICAL AND MATERIALS ENGINEERING

OCTOBER 2007

Approval of the thesis:

**EFFECT OF AGING ON THE MECHANICAL PROPERTIES OF BORON  
CARBIDE PARTICLE REINFORCED ALUMINUM METAL MATRIX  
COMPOSITES**

submitted by MUSTAFA SERDAR KARAKAŞ in partial fulfillment of the requirements for the degree of Doctor of Philosophy in Metallurgical and Materials Engineering Department, Middle East Technical University by,

Prof. Dr. Canan Özgen  
Dean, Graduate School of **Natural and Applied Sciences**

\_\_\_\_\_

Prof. Dr. Tayfur Öztürk  
Head of Department, **Metallurgical and Materials  
Engineering**

\_\_\_\_\_

Prof. Dr. Bilgehan Ögel  
Supervisor, **Metallurgical and Materials Engineering  
Dept., METU**

\_\_\_\_\_

Prof. Dr. Raif Orhan Yıldırım  
Co-Supervisor, **Mechanical Engineering Dept., METU**

\_\_\_\_\_

**Examining Committee Members:**

Prof. Dr. Şakir Bor  
Metallurgical and Materials Engineering Dept., METU

\_\_\_\_\_

Prof. Dr. Bilgehan Ögel  
Metallurgical and Materials Engineering Dept., METU

\_\_\_\_\_

Prof. Dr. Tayfur Öztürk  
Metallurgical and Materials Engineering Dept., METU

\_\_\_\_\_

Assoc. Prof. Dr. Gürkan Karakaş  
Chemical Engineering Department, METU

\_\_\_\_\_

Assoc. Prof. Dr. Mustafa Übeyli  
Mechanical Engineering Department, TOBB-ETU

\_\_\_\_\_

**Date:**

\_\_\_\_\_

**I hereby declare that all information in this document has been obtained and presented in accordance with academic rules and ethical conduct. I also declare that, as required by these rules and conduct, I have fully cited and referenced all material and results that are not original to this work.**

Name, Last name : Mustafa Serdar Karakaş

Signature :

## ABSTRACT

### EFFECT OF AGING ON THE MECHANICAL PROPERTIES OF BORON CARBIDE PARTICLE REINFORCED ALUMINUM METAL MATRIX COMPOSITES

Karakaş, Mustafa Serdar

Ph.D., Department of Metallurgical and Materials Engineering

Supervisor : Prof. Dr. Bilgehan Ögel

Co-Supervisor: Prof. Dr. Raif Orhan Yıldırım

October 2007, 133 pages

Metal matrix composites (MMCs) of Al - 4 wt.% Cu reinforced with different volumetric fractions of B<sub>4</sub>C particles were produced by hot pressing. The effect of aging temperature on the age hardening response of the composites was studied and compared with the characteristics exhibited by the matrix alloy. Reinforcement addition was found to considerably affect the age hardening behavior. Detailed transmission electron microscopy and differential scanning calorimetry observations were made to understand the aging response of the composites. The low strain rate and high strain rate deformation behavior of the MMCs were determined utilizing low velocity transverse rupture tests and true armor-piercing steel projectiles, respectively. Increasing the volume fraction of B<sub>4</sub>C led to a decrease in flexural strength. The flexural strength vs. strain rate plots showed a slight increase in strength followed by a decrease for all samples. The mechanical performance of the composites and the unreinforced alloy were greatly improved by heat treatment. The MMCs were found to be inferior to monolithic ceramics when used as facing plates in armors.

Keywords: Metal Matrix Composites, Aging, Strain Rate

## ÖZ

### BOR KARBÜR PARÇACIK TAKVİYELİ ALÜMİNYUM METAL ANAYAPILI KOMPOZİTLERİN MEKANİK ÖZELLİKLERİNE YAŞLANDIRMANIN ETKİSİ

Karakaş, Mustafa Serdar

Doktora., Metalurji ve Malzeme Mühendisliği Bölümü

Tez Yöneticisi : Prof. Dr. Bilgehan Ögel

Ortak Tez Yöneticisi: Prof. Dr. Raif Orhan Yıldırım

Ekim 2007, 133 sayfa

Farklı hacim oranlarında B<sub>4</sub>C parçacık takviyeli Al - ağırlık % 4 Cu alaşımlarından oluşan metal anayapılı kompozitler (MAK'ler) sıcak presleme yöntemi ile üretilmiştir. Yaşlandırma sıcaklığının kompozitlerin sertliğine olan etkisi incelenmiş, ve matris alaşımı ile kıyaslanmıştır. Takviye malzemesi ilavesinin yaşanmayı önemli ölçüde etkileyebileceği görülmüştür. Yaşlandırmanın etkilerini tespit etmek amacıyla detaylı geçirimli elektron mikroskobu incelemeleri ve diferansiyel taramalı kalorimetri analizleri yapılmıştır. Üretilen MAK'lerin ayrıca düşük ve yüksek deformasyon hızlarındaki davranışları, sırasıyla düşük hızdaki eğme deneyleri ve gerçek zırh delici mermiler ile incelenmiştir. Takviye elemanı ilavesinin eğme mukavemetinde düşüşe sebep olduğu bulunmuştur. Eğme mukavemetinin artan deformasyon hızı ile önce artış gösterdiği, ancak belirli bir değerden sonra azaldığı görülmüştür. Kompozitlerin ve takviyesiz alaşımın mekanik performansının ısıtma işlemi ile büyük ölçüde iyileştirilebilmiştir. Zırhlarda ön plaka olarak kullanılan MAK'lerin monolitik seramiklere nazaran daha zayıf olduğu tespit edilmiştir.

Anahtar kelimeler: Metal Anayapılı Kompozitler, Yaşlanma, Deformasyon Hızı

To My Parents

## **ACKNOWLEDGMENTS**

The author would like to express his deepest gratitude to his supervisor Prof. Dr. Bilgehan Ögel and co-supervisor Prof. Dr. Raif Orhan Yıldırım for their guidance, advice, criticism, encouragements and insight throughout the research.

The author also wishes to thank Prof. Dr. Tayfur Öztürk for his suggestions and comments.

Part of this study was conducted in the Ames Laboratory of the Iowa State University. Special thanks are due to Assoc. Prof. Dr. Matthew Kramer for his hospitality and guidance.

This study was supported by the State Planning Organization (DPT) Grant No: BAP-08-11-DPT-2002K120510.

## TABLE OF CONTENTS

ABSTRACT .....	iv
ÖZ.....	v
ACKNOWLEDGMENTS.....	vii
TABLE OF CONTENTS .....	viii
CHAPTER	
1. INTRODUCTION.....	1
2. LITERATURE REVIEW .....	3
2.1 Classification of Composite Materials .....	3
2.1.1 Polymer Matrix Composites.....	3
2.1.2 Ceramic Matrix Composites.....	4
2.1.3 Metal Matrix Composites.....	7
2.2 Fabrication Methods for MMCs.....	9
2.2.1 Liquid Phase Processes .....	9
2.2.2 Solid Phase Processes.....	11
2.2.3 Two Phase Processes.....	15
2.3 Ceramic/Metal Interfaces in MMCs.....	16
2.4 Strengthening Mechanisms in MMCs.....	20
2.4.1 Strengthening by Reinforcement Addition.....	20
2.4.2 Strengthening by Heat Treatment.....	22
2.4.3 Property Estimation for MMCs.....	36
2.5 The Future of MMCs.....	44
2.5.1 MMCs for Armor Applications.....	47



3. EXPERIMENTAL .....	50
3.1 Materials .....	50
3.2 Fabrication .....	53
3.2 Heat Treatments .....	56
3.3 Hardness Tests .....	57
3.4 Differential Scanning Calorimetry .....	58
3.5 Transverse Rupture Tests .....	58
3.6 Ballistic Tests .....	59
3.7 Metallography .....	63
3.8 Fractography .....	64
4. RESULTS .....	65
4.1 Microstructures .....	65
4.2 Aging Studies .....	70
4.3 Differential Scanning Calorimetry .....	74
4.4 Transmission Electron Microscopy .....	75
4.5 Effects of Strain Rate .....	79
4.6 Fractography .....	82
5. DISCUSSION .....	107
6. CONCLUSIONS .....	115
REFERENCES .....	118
VITA .....	133

## **CHAPTER 1**

### **INTRODUCTION**

Metal matrix composites (MMCs) have the ability of unifying the properties of their ceramic and metal constituents, which makes them suitable materials for a variety of applications. However, the properties of MMCs greatly depend on the judicious selection of processing techniques and parameters, including the selection of the constituents, the fabrication method, and the heat treatment procedures. MMCs can be manufactured by many methods, such as powder metallurgy, spray forming, and liquid or semi-solid mixing. Powder metallurgy can produce near net shape products with superior properties. An important drawback of this method, however, is its relatively higher cost.

For achieving good mechanical properties in a composite material, the size, volume fraction, and distribution of the ceramic reinforcement is of great importance. The interfacial integrity of the reinforcement and its influence on the matrix microstructure can also considerably effect the properties of the resulting composite. Many changes in microstructural features may occur in MMCs, including changes in grain size, dislocation density, precipitation behavior and solid solubility. Knowledge and control of such features are critical for both fabrication and tailoring.

Although continuous fiber reinforced MMCs are superior in many aspects, discontinuously reinforced MMCs based on whiskers and particulates as the reinforcement are beginning to be preferred due to their comparatively lower manufacturing costs. Particle reinforced MMCs have recently emerged as

affordable material candidates for commercial and military applications. The hypothesis that MMCs exhibit excellent work hardening characteristics indicates that these materials may also have potential for lightweight ballistic applications.

Developments in MMCs have been mainly centred around the use of aluminum alloys as the matrix material due to their good strength to weight ratios. Another important advantage of aluminum alloys is low melting temperature, which decreases production costs. The present work deals with obtaining particle-reinforced age hardenable aluminum matrix composites with varying volume fractions, and examining their high strain rate behaviour.

In this study, an Al - 4 wt.% Cu alloy was chosen as the matrix because of its heat treatability, and also to achieve liquid phase sintering during production. Boron carbide ( $B_4C$ ) was chosen as the reinforcement due to its low density and high hardness. The amount of  $B_4C$  reinforcement in the matrix was varied between 0 vol.% (unreinforced) and 40 vol.%. The matrix alloy and the composites were produced by hot pressing the powder mixtures at temperatures above the solidus. After production, the samples were subjected to various heat treatments involving age (precipitation) hardening. The mechanical properties of the as-fabricated and heat treated samples were compared by hardness and transverse rupture tests. The effect of reinforcement addition on aging was studied by various methods, including hardness tests, transmission electron microscopy (TEM), and differential scanning calorimetry (DSC). The transverse rupture tests of the samples were carried out over a wide range of strain rates, and the fracture surfaces were examined by scanning electron microscopy (SEM). The heat treated samples were additionally tested at high strain rates as facing plates in composite armors with a 2024-T851 aluminum alloy as backing, and compared with a  $B_4C$  ceramic composite with the same backing material. The impact surfaces of the armors were examined and the possible deformation mechanisms were discussed and disclosed.

## **CHAPTER 2**

### **LITERATURE REVIEW**

#### **2.1. Classification of Composite Materials**

The major types of structural composites that exist today can be categorized as Polymer Matrix Composites (PMCs), Ceramic Matrix Composites (CMCs), and Metal Matrix Composites (MMCs). These three composite types are summarized below.

##### **2.1.1. Polymer Matrix Composites**

PMCs have found widespread application, and are the most developed class of composite materials today. They can be fabricated into large, complex shapes. PMCs are constructed of components such as glass or carbon fibers bound together by an organic polymer matrix, such as polyester or epoxy. For delivery purposes, the fibers that are to be used in PMC production are usually wound around a bobbin, collectively called a roving. An untwisted, unwound bundle of fibers is called a tow. The fiber in a PMC provides the high strength and modulus, while the matrix distributes the load and protects the fibers against corrosion. The strength of the composite is almost directly proportional to the basic fiber strength, and can be improved at the expense of stiffness. Various techniques can be used for the fabrication of PMCs. Some of the methods shall be described briefly.

The simplest method is hand lay-up. The fibers are laid into a mold and the resin is sprayed, brushed, or rolled on the fibers. Sometimes the resin and the fiber are sprayed into the mold together. In both cases the deposited layers are densified with rollers, and accelerators and catalysts are frequently used.

Filament winding is a process in which a resin-impregnated tow or roving is wound over a rotating or stationary mandrel with the help of a carriage unit. By controlling the motion of the carriage unit and the mandrel, the desired fiber angle is generated. Curing is done at elevated temperatures. This method is highly suitable for the production of large-volume vessels.

The pultrusion process is a process in which continuous, aligned fiber composites are made by pulling resin-impregnated fibers through a die. The method is quite similar to the drawing process in metals. As the material passes through the die, it becomes partially or completely cured, and usually does not require post-processing. Parts with constant cross-section and continuous length can be easily created by pultrusion.

The most common method for making high performance PMCs is the prepreg lay-up process. Thin sheets containing unidirectional fibers impregnated with partially cured resin, called prepregs, are stacked at appropriate orientations, vacuum bagged, and subsequently cured in an autoclave. This method is widely used in the aerospace industry. One important advantage of this process is that it permits the production of high fiber volume fraction (more than 60 %) composite parts [1], owing to the use of the prepregs.

### **2.1.2. Ceramic Matrix Composites**

Monolithic ceramics have attractive properties such as high temperature and corrosion resistance, but also have many limitations to their use due to their

lack of toughness. Ceramics are prone to catastrophic failure in the presence of internal (pores, inclusions, and microcracks) or surface (scratches or nicks) flaws. They are extremely susceptible to thermal shock and any damage done to them during their fabrication and/or service. The incorporation of a reinforcing phase, such as ceramic fiber reinforcement, can help improve the mechanical properties of the material by hindering crack propagation by fiber-matrix interfaces. CMCs belong to a class of structural materials with reinforcements such as SiC fibers embedded in a ceramic matrix such as  $\text{Al}_2\text{O}_3$ ,  $\text{Si}_3\text{N}_4$  or SiC [2]. The reinforcements can be continuous fibers, chopped fibers, small discontinuous whisker platelets, or particulates.

The distinction between CMCs and non-ceramic matrix composites arises from the fact that the matrix is capable of bearing a load that can be very close to that of the fiber. Another distinct property is the thermal mismatch between the component materials. Due to the limited ductility of both components, the thermal expansion coefficient plays a very important role in the performance of CMCs.

The fabrication of a CMC is usually conducted in a two-stage process [3]. The reinforcement is incorporated into the unconsolidated matrix, and subsequently consolidated. The incorporation of the fiber usually involves some kind of fiber alignment. The most common technique of fiber incorporation for CMCs is the slurry infiltration process. A fiber tow is passed through a slurry tank (containing the matrix powder and an organic binder in a carrier liquid,) and wound on a take-up drum and dried. This is followed by the stacking of the tows and finally consolidation. Porosity in the ceramic matrix material is a common and serious flaw. The size of the matrix powder should be smaller than the fiber diameter, and the fugitive binder should be completely removed during processing. The fibers should suffer as little damage as possible.

Another very common method utilized for the fabrication of CMCs is hot pressing. This method is expensive, but the CMCs produced by this technique have superior mechanical properties. Powder size distribution, temperature, and pressure are critical parameters that control the matrix porosity, fiber damage, and fiber/matrix bond strength. Applying too little pressure may cause porosity to develop in the matrix, while applying too much pressure may lead to fiber damage. The choice of temperature will affect the reactions and bonding at the fiber/matrix interface.

Cold pressing of the fiber and matrix powders followed by sintering is another method for CMC production. In this technique, the matrix generally tends to shrink too much during sintering, leading to the formation of many cracks that are retained in the resultant composite.

Melt infiltration, in-situ chemical reaction, and sol-gel and polymer pyrolysis are other techniques that can be used to produce CMCs. Melt processing yields a high-density, virtually pore-free matrix, and practically any reinforcement geometry can be used. The temperatures involved, however, are very high. In-situ methods are extensions of monolithic ceramic production techniques. These include chemical vapor deposition (CVD), chemical vapor infiltration (CVI), and reaction bonding. Sol-gel and polymer pyrolysis techniques have also been used to make ceramic matrix materials in a fibrous preform. Advantages of these techniques include lower processing temperatures, greater compositional homogeneity in single phase matrices, and the potential of producing unique multiphase matrix materials. Covalent ceramics can be produced by the pyrolysis of polymeric precursors at temperatures as low as 1400°C with yields greater than CVD processes. The disadvantages of these techniques are high shrinkage and low yield compared to slurry techniques. To attain a high density, repeated infiltrations and thermal decompositions are usually required.

CMCs are emerging as a class of advanced engineering structural materials. Unfortunately their current use is limited to high-temperature applications. In the future CMCs are expected to have much wider use in military, aerospace and commercial applications.

### **2.1.3. Metal Matrix Composites**

Superior mechanical properties and some unique characteristics can be obtained by dispersing the reinforcement into an alloy. Such materials, consisting of a metal alloy reinforced with fibers, whisker, or particles are called metal matrix composites (MMCs).

Most of the commercial work on MMCs is focused on aluminum as a matrix material. Its combination of light weight, corrosion resistance, and mechanical properties has made aluminum very popular. The melting point of aluminum is high enough to satisfy many application requirements, yet low enough to render composite processing reasonably convenient.

Aluminum can accommodate a variety of reinforcements. The reinforcement, characterized as either continuous or discontinuous, may constitute up to 80 vol.% of the MMC [4]. Although much of the early work on aluminum matrix composites (AMCs) were focused mainly on continuous fiber composites, most of the present studies are focused on discontinuous fiber, whisker and particle reinforced AMCs because of their greater ease of manufacture, low production costs, and relatively isotropic properties [5]. The types of reinforcement will be discussed below.

**Fibers and filaments:** Continuous or unbroken fibers have extremely high aspect ratios (the ratio of length to diameter). The diameters of fibers are usually between 3 and 30  $\mu\text{m}$  while filaments are usually greater than 100  $\mu\text{m}$ .



The typical cost for continuous fibers are around \$600/kg, and for this reason fiber-reinforced composites suffer from high cost as well as from not being amenable to many metal working operations. Recently, chopped fibers with lower aspect ratios and random orientations have also been used. Although their properties are more isotropic and the costs are lower, the use of chopped fiber reinforced MMCs are limited by their secondary fabrication options.

**Whiskers:** These are monocrystalline materials with high aspect ratios ranging from 50 to 100. Their small size makes them suitable for a variety of MMC production techniques, although powder metallurgy is the most popular. The typical cost for these reinforcements is around \$20/kg, much less expensive than fibers. Whisker reinforced MMCs can be used in the form of extrusions, forgings and rolled sheet. The properties of whisker reinforced MMC components range from isotropic to slightly anisotropic, and their costs range from moderate to high, depending on the mechanical and physical properties.

**Particles:** Particles or particulates have low aspect ratios, generally between 1 and 5. Their typical costs are around \$10/kg, which makes them relatively inexpensive. Particle reinforcements encompass everything from polycrystalline microspheres to grinding grit to monocrystalline platelets. One of the most important advantages of particle reinforced MMCs are their suitability for standard metalworking operations.

The ability of an MMC to unify the properties of the ceramic phase with that of the metal matrix greatly depends on the careful selection of materials, processing technique, and heat treatment procedures.

## 2.2. Fabrication Methods for MMCs

The various processing methods for particle reinforced MMCs can be categorized regarding the temperature of the matrix phase during processing. Accordingly, the processes can be classified as liquid-phase, solid-phase and two-phase processes. All three methods will be discussed below.

### 2.2.1. Liquid Phase Processes

The liquid phase processes for MMC manufacture include the vortex method and liquid metal infiltration.

**i. The Vortex method.** This simple mixing method, first demonstrated by researchers in India, involves the simple procedure of adding ceramic particles through the sides of a vortex [6] created in the melt with a mechanical impeller. Fig. 2.1 is schematic diagram of the equipment used. Because most metals do not wet ceramic particles, early attempts for incorporating ceramic particles into metallic melts had limited success. The use of a high processing temperature (e.g. more than 900°C for aluminum) usually causes the melt to react with the reinforcement, thereby enhancing the wetting between the metal and the ceramic. This reaction must be constrained so as to be sufficient to wet the reinforcement to promote bonding without causing excessive degradation of the reinforcement. In some cases, wetting agents such as Mg or Cu can also be added to the aluminum melt to improve wetting.

Disadvantages of the vortex method can be summarized as reinforcement clustering and/or damage during mechanical agitation, settling of the ceramic particles (mostly due to density differences), segregation of secondary phases in the metal matrix, and extensive interfacial reactions. In some cases,

however, reaction between the reinforcement and the matrix is intentionally allowed, causing the desired reinforcement to be formed in-situ.

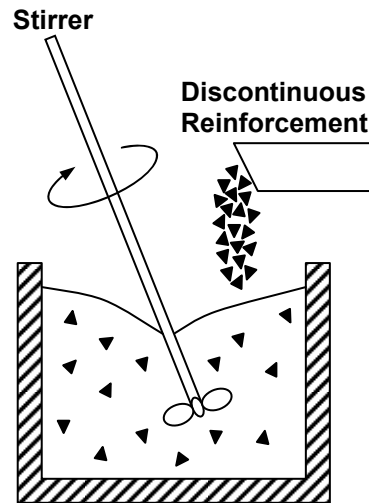


Fig. 2.1. Schematic of the Vortex method

**ii. Liquid metal infiltration:** This technique can be used to produce complex shapes containing high volume fractions of reinforcement, typically greater than 50 vol.% [7-10]. In this method the molten alloy is forced into the interstices left between the powders, whiskers or fibers packed in a self supporting preform.

Either a pressurized gas (Fig. 2.2a) or piston (Fig. 2.2b) is utilized to inject the molten metal into the preform. While gas-driven devices are restricted to below 10 MPa, piston driven devices can deliver about 100 MPa of pressure. The pressure required for combining the matrix and the reinforcement is a function of the effects of reinforcement is a function of friction effects arising from the viscosity of the molten metal as it fills the preform. Wetting of the ceramic preform by the liquid alloy is again an issue, depending on several competing factors such as alloy composition, nature of the ceramic preform, ceramic

surface treatment, surface geometry, interfacial reactions, surrounding atmosphere and time. Recently, pressureless metal infiltration processes have been developed, in which deliberate alterations in the chemistry of the molten alloy and the surrounding environment allow the preform to be infiltrated spontaneously by the liquid metal. The elimination of tooling requirements makes pressureless infiltration a preferred method for composite manufacture.

Despite its many advantages, liquid metal infiltration has many drawbacks as well. Its primary disadvantages include reinforcement damage, compression of the preform, microstructural heterogeneity, coarse grain size, mutual contact between the reinforcements, and undesirable surface reactions.

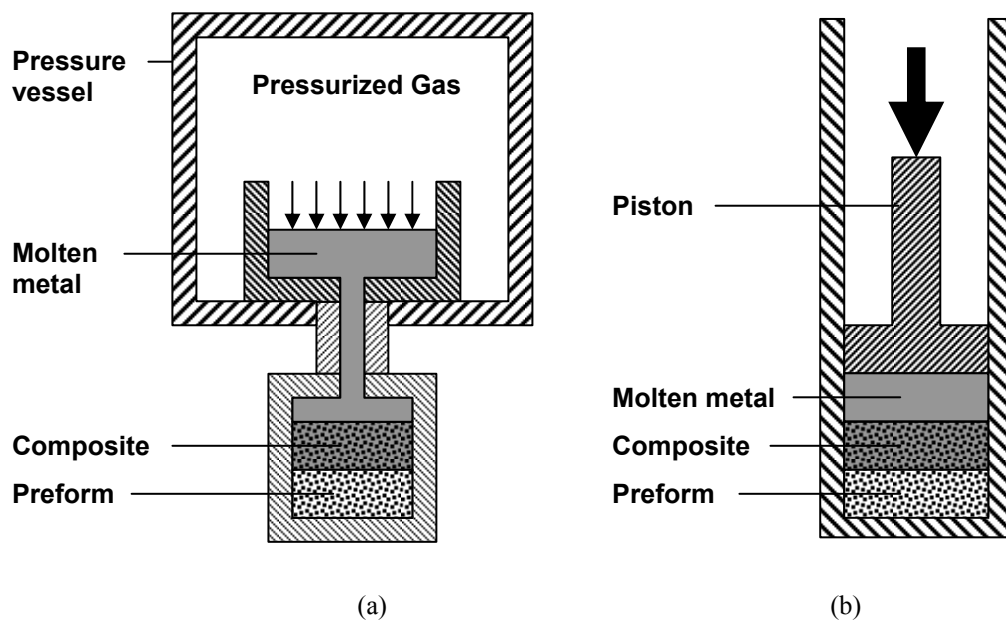


Fig. 2.2. Liquid melt infiltration: (a) Gas-driven melt infiltration and (b) Squeeze casting.

### 2.2.2. Solid Phase Processes

Because of the difficulty in wetting ceramic particles with molten metal, the powder metallurgy process was the first method developed [4,7,8]. The

essential features of the powder metallurgy method are shown in Fig. 2.3. The method involves: (1) The blending of a gas atomized matrix alloy and reinforcement in powder form; (2) cold compaction of the homogeneous blend to approximately 80% density; (3) Hot pressing, forging, or extruding the cold-compacted billet to full density.

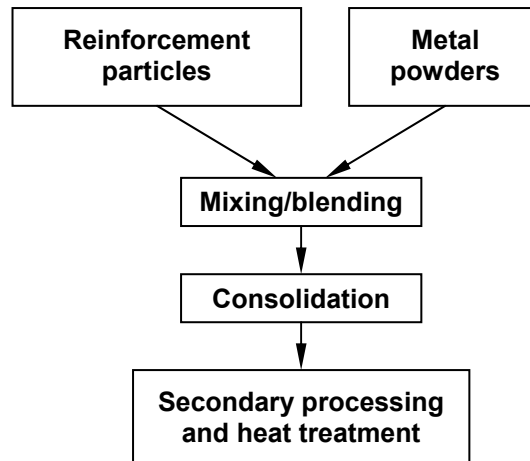


Fig. 2.3. Flowchart for powder metallurgy MMC fabrication.

The powder metallurgy route has many advantages. Because the reaction at the reinforcement/matrix interface is minimal, any matrix alloy/reinforcement combination can be chosen for production. Relatively high volume fractions of reinforcement can also be achieved, which maximizes the modulus and minimizes the coefficient of thermal expansion (CTE). With proper choice of particle sizes, clustering of the reinforcement can also be minimized.

The kinetics of densification can be improved using liquid phase sintering (LPS). Reaction can readily occur at the interface between the reinforcement and the liquid phase, and interfacial strength may be improved. However, excess reaction at the interface may also result in the formation of undesirable compounds. LPS may also degrade the microstructure of the rapidly solidified

powder particles by generating coarse eutectic intermetallic phases in the melted regions. Therefore, careful control of temperature is crucial for the liquid phase sintering of alloys and composites.

In the powder metallurgy processing of an MMC, a critical value of reinforcement size [11] exists for the uniform distribution of reinforcement, considering the size difference effect between the matrix powder and the reinforcement particles. A uniform distribution of reinforcement could be expected only when the reinforcement size is not less than a critical value which is a function of matrix powder size and volume fraction.

Assuming spherical reinforcements distributed uniformly in the matrix, shown schematically in Fig. 2.4, the volume fraction is

$$V_f = \frac{\pi d_r^3}{6(\lambda + d_r)^3} \quad (2.1)$$

where  $d_r$  is the reinforcement size and  $\lambda$  is the interparticle spacing.

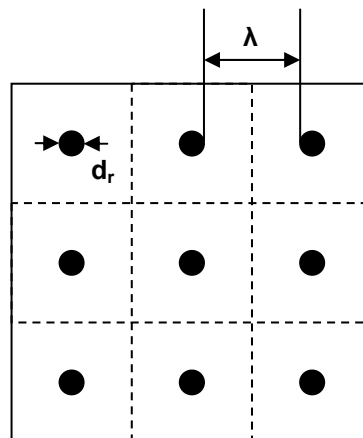


Fig. 2.4. The ideal condition: spherical reinforcements uniformly distributed in the matrix.

The dependence of interparticle spacing on size and volume fraction of reinforcement can be derived as

$$\lambda = d_r \left[ \left( \frac{\pi}{6V_f} \right)^{1/3} - 1 \right]. \quad (2.2)$$

Ideally the interparticle spacing decreases with decreasing reinforcement size and increasing volume fraction.

Sintered aluminum powder (SAP) alloys have properties that are in many ways different from those fabricated by conventional methods. The oxide that immediately forms on the surface of aluminum is not reduced back to metallic form during sintering, and the resulting powder product therefore contains a substantial amount of oxide [12]. This oxide impedes grain growth and movement of dislocations at or through its boundaries, and thus produces high strength, high creep resistance and insensitivity to high-temperature exposure.

The natural oxide that forms on the surface of the powder is some 100 Å thick, is amorphous, and contains absorbed water. The amount of oxide in aluminum powder can be as much as 20 vol.% Al<sub>2</sub>O<sub>3</sub> in flake powder. In atomized powders (which are spherical or rounded) the volume fraction of oxide is only a few percent. Electrolytic powders are known to have intermediate amounts. Ball milled powders generally consist of small particles that are welded together so that the oxide is present not only at the surface but also within the particles.

The properties of SAP depend on the amount of naturally formed oxide. Heating the powder to increase the thickness of the oxide film, or the addition of Al<sub>2</sub>O<sub>3</sub> particles prior to sintering generally does not increase the strength and only reduces ductility. Artificial SAP-type products can be made by dispersing

$\text{Al}_2\text{O}_3$  powder into molten aluminum with ultrasonic vibration or by blowing reducible oxides of high melting point metals into the aluminum melt. Powders that are milled wet with hydrocarbons will contain  $\text{Al}_4\text{C}_3$  in addition to oxide.

Absorbed water within the powder reacts with the metal to form additional oxide and release hydrogen. The hydrogen may produce porosity at the grain boundaries and cracking or blistering. The higher the amount of oxide, the more hydrogen is released and the more pronounced the embrittlement and defect formation, especially with cyclic heating and cooling. Vacuum treatment or high temperature sintering before complete compacting reduces hydrogen content and eliminates most if not all of the cracking. Small additions of aluminum fluoride have also proven useful in reducing the effect of hydrogen.

The oxide in SAP is present as finely dispersed particles, which interact with vacancies and dislocations and prevent their easy movement. The oxide effect persists even above the melting point of aluminum.

Along with its numerous benefits, the powder metallurgy method also has some disadvantages. It involves the handling of highly reactive, potentially explosive powders, and the manufacturing route is relatively complex. The resulting product is also generally expensive compared to conventional wrought aluminum alloys.

### **2.2.3. Two Phase Processes**

**i. Spray deposition:** Spray deposition is a technique developed by Osprey Metals in the United Kingdom [1]. Reinforcements are introduced into a stream of molten alloy which is subsequently atomized by jets of an inert gas. The sprayed mixture is collected on a substrate in the form of a reinforced metal matrix billet. Hybrid rapid solidification is achieved; the metal experiences a



rapid transition through the liquidus to the solidus, followed by slow cooling from the solidus to room temperature, with a refined grain structure as a result. This process is cost-efficient because the blending and consolidation steps of the powder method are combined in a single step. Although initially developed for difficult-to-cast steels, nickel superalloys and copper, aluminum developments are now showing considerable promise.

**ii. Compcasting:** Compcasting is a variation of the rheocasting procedure in which ceramic particles are stirred into a liquid melt in the semi-solid (mushy) state of the metal [1,4]. Particles and discontinuous fibers have been successfully incorporated into vigorously agitated partially solidified aluminum alloys by this technique. The discontinuous reinforcement is mechanically trapped between the solid phase present in the alloy slurry which is carefully held between the liquidus and solidus temperatures. Under mechanical agitation, the possibility of agglomeration, settling and floatation is avoided. The solid metal particles in the slurry have a non-dendritic rounded form that permits the slurry to be shaped by casting, preferably using pressure/shear to ensure the flow of the viscous material. The mixture exhibits thixotropy in that the viscosity decreases with increasing shear rate.

### **2.3. Ceramic/Metal Interfaces in MMCs**

An interface is, by definition, a two-dimensional region through which a discontinuity in one or more material parameters exists [18]. In reality there is always some volume associated with this interface region over which a gradual transition occurs.

The interface region is extremely important in determining the ultimate properties of the composite. Its importance is due to the fact that (i) the interface occupies a very large area, and (ii) the reinforcement and the matrix

are generally not in equilibrium. Some bonding must exist between the ceramic reinforcement and the metal so that load transfer from matrix to reinforcement can occur. The reaction at the interface can usually be observed by electron microscopy or secondary ion mass spectroscopy.

For the control of the extent of interface reaction, common practices include shortening or lengthening the processing time, coating the reinforcements with materials of different reactivities, and adding alloying elements to the matrix [19]. Different types of interfacial reactions may occur for the same composite system depending on the temperatures involved during both fabrication and application. However, the thermodynamic equilibrium phase diagrams – including binary, ternary, or even higher order systems – only provide the trend for the reaction. The actual products formed at the interface depend on the diffusion path of the constituents of the composite. Such kinetic factors must be determined experimentally. Greater knowledge of thermodynamics and kinetics of multicomponent systems offers better hope for designing MMCs for high-temperature applications.

Important material parameters involved in the transition at the interface are elastic moduli, chemical potential, and the coefficient of thermal expansion (CTE). The discontinuity in chemical potential is likely to cause chemical compound formation or the formation of an interdiffusion zone. The discontinuity in the thermal expansion coefficient may cause high residual stresses to develop when the composite is cooled from its bonding temperature.

One of the most important problems in the fabrication of MMCs relates to the residual stress remaining in the bonded product due to thermal expansion mismatch. The thermal expansion coefficients of metals are generally higher than those of ceramics. The differences in thermal expansion may cause high residual stresses to develop when the bonded product is cooled from the bonding temperature. The tensile stresses that build up on the ceramic may

cause the ceramic to break. Choosing a soft metal, such as aluminum, is the typical method for minimizing such internal stresses.

An additional problem is wetting accompanied with interfacial reaction and material transition on the interface. The reactivity between the metal and the ceramic depends primarily on the temperature. The estimate of reactivity can be obtained by the study of the standard free energy of formation calculations. Some mutual reaction of both materials is necessary for bonding, but a very strong reaction is generally undesirable. The interfacial layer usually has an optimal thickness value, and therefore a certain degree of wetting between the ceramic and the liquid metal [13-17] is necessary. Unfortunately, most ceramic materials are not wetted by liquid metals. The basic reason for this is that ceramics are ionic or covalent in nature and are incompatible with the metallic species.

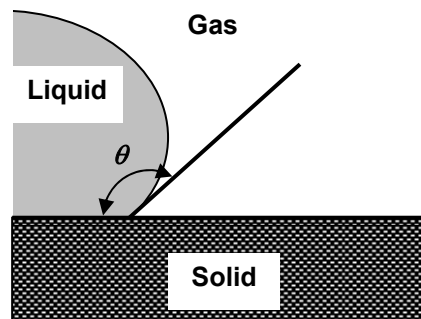


Fig. 2.5. Schematic of a liquid drop resting on a solid surface, showing the contact angle  $\theta$

The wettability of a solid by a liquid is indicated by the contact angle  $\theta$  defined in Fig. 2.5. This angle is related to the three surface tensions  $\gamma_{sg}$ ,  $\gamma_{sl}$ , and  $\gamma_{lg}$  of the solid-gas, solid-liquid, and liquid-gas interfaces, respectively, by the well known Young-Dupré equation

$$\gamma_{lg} \cos \theta = \gamma_{sg} - \gamma_{sl} \quad (2.3)$$

Ideal wetting will occur when the contact angle  $\theta$  is close to zero, although contact angles less than  $90^\circ$  are also sufficient for wetting to occur. A contact angle of  $180^\circ$  defines complete non-wettability

$$D_f = \gamma_{sg} - \gamma_{sl} \quad (2.4)$$

It is sometimes helpful to think of the interface tension  $\gamma_{sl}$  with reference to the tensions  $\gamma_{sv}$ , and  $\gamma_{lv}$  of the surfaces of the solid and liquid in vacuum. The work of adhesion is then defined as

$$W_a = \gamma_{sv} + \gamma_{lv} - \gamma_{sl} \quad (2.5)$$

which is equal to the work that must be spent in order to separate one unit of surface area between the two phases in vacuum. It is therefore a measure of binding between the two phases. Since  $\gamma_{sg} = \gamma_{sv}$  in a vacuum, using the above equation one can write

$$D_f = -(\gamma_{lv} - W_a) \quad (2.6)$$

and

$$W_a = \gamma_{lv}(1 + \cos \theta). \quad (2.7)$$

When the surface tension  $\gamma_{lv}$  of the liquid phase is known, the work of adhesion can thus be experimentally determined from the measurement of contact angle at the edge of a sessile drop of liquid metal resting on a flat surface, provided that the conditions of vacuum and absence of contamination of the solid surface are fulfilled.

## **2.4. Strengthening Mechanisms in MMCs**

The strength of a particle reinforced MMC depends on many factors, such as the reinforcement volume fraction, heat treatment, and strain history. In the following two sections the effects of reinforcement addition and heat treatment will be discussed and disclosed.

### **2.4.1. Strengthening by Reinforcement Addition**

The strengthening in MMCs caused by ceramic particle additions has been extensively studied in the past; however no consensus has yet been reached regarding its origin. Many dislocation models that were originally developed for dispersion and precipitation hardened alloys have been modified and others specifically designed for predicting the strengthening in this class of materials [20-25]. Most of these models tend to underestimate the strengthening of the metallic matrix caused by the presence of the ceramic phase. This is primarily because of the neglect of the “load sharing” contribution to composite strengthening.

The volume fraction of the reinforcement in MMCs is relatively high compared to precipitation or dispersion hardened alloys, and therefore a significant amount of strengthening arises from the fact that the matrix sheds load to the reinforcement during straining. Load sharing is a concept central to continuum mechanics, which proposes models like unit-cell, modified shear lag theory and different homogenization models [26-30] to predict strengthening in particle reinforced composites based on the knowledge of the bulk metal matrix properties, and the volume fraction, aspect ratio and spatial arrangement of the particles.

The strengthening of the MMC is dependent on the size of the reinforcement. Several continuum models [31-35] have been reasonably successful in predicting the mechanical properties of high strength aluminum alloys reinforced with relatively large particles that have a mean diameter of 50  $\mu\text{m}$  or larger. In such MMCs the microstructural length scale that determines the deformation behavior of the unreinforced alloy does not significantly change in the presence of reinforcement. For unreinforced precipitation hardened alloys the inter-precipitate distance is an important parameter for deformation. In the presence of the reinforcement, the size of the precipitates are considerably smaller than the reinforcing particles, thus the interaction with dislocation motion remains dominant.

When the matrix of the composite is a pure metal or low strength alloy, and/or the size of the reinforcement is significantly reduced to below 10  $\mu\text{m}$ , classic continuum theories break down since in this case there is a strong dependence of composite properties on reinforcing particle size [22,24,36-40]. Modelling the constitutive behaviour of such composites has renewed interest in a dislocation approach to strengthening in particle reinforced composites due to its inherent dependence on length scale.

Most of the literature on strengthening in particle reinforced composites reveals a certain polarization regarding the approach used. In the continuum approach, dislocation effects are generally not considered; and in dislocation-based models, the load sharing term of strengthening is often neglected. A combinatory effect from both mechanisms appears to be more likely for the strengthening of particle reinforced composites. Hybrid approaches, which relate the key features of dislocation density to continuum mechanics [41-45], have proven to be quite successful [46-52], and recent developments in strain gradient plasticity [53,54] have provided an alternative means to incorporate microstructural length scales to composite constitutive modeling.

### 2.4.2. Strengthening by Heat Treatment

When a binary phase diagram of an alloy has a high solid solubility at high temperatures but decreases markedly with decreasing temperature, that alloy is considered to have potential for age hardening. The Al - 4 wt.% Cu alloy is a perfect example [55,56]. Wrought 2000 series aluminum alloys are age hardenable alloys which have originated from the age hardenable Al-Cu alloys, and have additional alloying elements, such as magnesium. The additional alloying elements in these alloys improve the mechanical properties by modifying the precipitates that are formed during ageing.

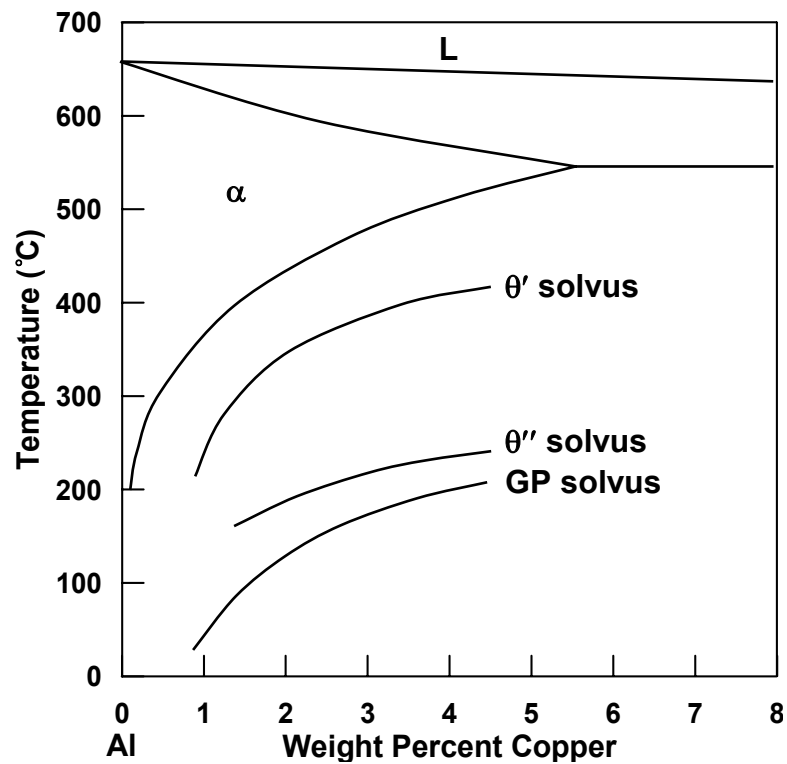


Fig. 2.6. The aluminum end of the Al-Cu phase diagram [55].

The Al-rich part of the Al-Cu phase diagram is given in Fig. 2.6. The diagram tells us that the solubility limit of copper in aluminum decreases from 4 wt.% at 500°C to about 0.1 wt.% at room temperature.

The Al - 4 wt.% Cu alloy consists of a single phase in the range of 500 to 580°C. The copper dissolves in aluminum to give a random substitutional solid solution  $\alpha$ . Below 500°C, the alloy enters the two-phase  $\alpha + \theta$  ( $\text{CuAl}_2$ ) region. As the temperature decreases the amount of  $\theta$  increases, such that at room temperature about 7 wt.% of  $\theta$  exists in the microstructure.

Under slow cooling, the driving force for the precipitation of  $\text{CuAl}_2$  is small and the nucleation rate is low; and the few nuclei that do form grow into large precipitates of  $\text{CuAl}_2$  that were spaced well apart. The large interparticle spacing is far from interacting with dislocations and the alloy is therefore soft. At higher rates of cooling, a much finer structure can be obtained; the nucleation rate is high, and many closely spaced precipitates are formed. The small interparticle spacing is effective as a barrier for moving dislocations, and this makes the alloy harder. There are limits to precipitation hardening that can be produced by direct cooling. If the cooling rate is too high, a supersaturated solid solution with no precipitates will be produced, and the alloy will be soft again. Therefore a series of heat treatments have to be applied [57-59] to reach the peak hardness of the alloy.

The standard heat treatment of the Al - 4 wt.% Cu alloy consists of three steps. The first step is called the solutionizing heat treatment. The alloy is heated to a temperature between 515°C and 550°C, bringing all of the Cu to solid solution.

In the second step the alloy is cooled rapidly to room temperature by quenching into water or oil. The quenching rate is high enough to miss the nose of the C-curve in the TTT diagram (Fig. 2.7), hence a supersaturated solid solution is obtained.



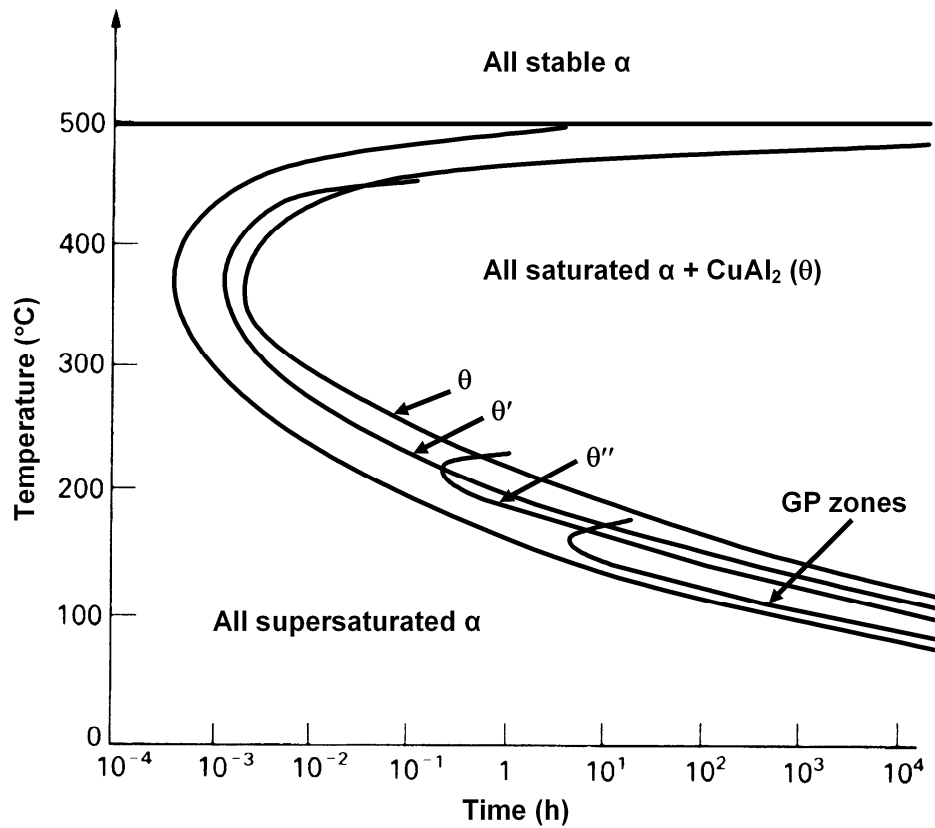


Fig. 2.7. The TTT diagram for the Al – 4 wt.% Cu alloy [62].

In the last step, the alloy is heated isothermally at a lower temperature, usually between 100°C and 180°C, in which the supersaturated solid solution gradually transforms to the equilibrium mixture of  $\alpha + \theta$ . As the transformation takes place at a low temperature, the  $\theta$  phase cannot separate itself from supersaturated  $\alpha$  at one step. Instead, the transformation takes place in 4 distinct stages. The sequence in which precipitation occurs is as follows:

Supersaturated solid solution  $\rightarrow$  GP zones  $\rightarrow \theta''$  (GP2)  $\rightarrow \theta' \rightarrow \theta$

Precipitation generally occurs in the above order, but there is disagreement as to whether they are successive steps of transformation from the supersaturated solid solution or that they are independently nucleated competing structures. The metastable solvus curves for the GP zones,  $\theta''$  and  $\theta'$  precipitates are shown in Fig. 2.6.

After quenching, aluminum alloys contain some  $10^{-4}$  to  $10^{-5}$  vacancies per atom, provided that the quench is reasonably rapid. During ageing, disc-shaped GP zones initially begin to nucleate homogeneously from the supersaturated solid solution [60]. The excess vacancies produced by quenching are thought to play an important role in their formation. The GP zone consists of one or more layers of pure copper in the (100) planes of the aluminum matrix [61]. The zone is coherent with the matrix and there is no boundary; and the Cu content of a zone depends on the number of Cu layers that are considered a part of it. GP zones have a thickness of about 1 nm and a diameter of about 10 nm. The formation and growth of GP zones is accompanied by hardening and decrease in ductility, which is attributed mainly to lattice distortion and pinning of dislocations or interference with their movement. GP zones have disc faces that are completely coherent with the matrix. The disc edges are also coherent, but a large coherency strain is present.

As ageing proceeds, some of the GP zones grow to form precipitates of  $\theta''$ , which are also referred to as GP2. There is some disagreement as to the preferred nucleation sites for  $\theta''$  precipitation, but in general they are found to nucleate at GP zones [60,62].  $\theta''$  precipitates are also in the form of discs, generally about 10 nm in thickness and 100 nm in diameter, spaced about 100 nm apart. The coherency of the  $\theta''$  precipitates in the matrix is very similar to that of GP zones: the disc faces are still completely coherent, but a large coherency strain exists on the disc edges.  $\theta''$  have a tetragonal lattice structure with  $a = 4.04 \text{ \AA}$  and  $c = 7.68 \text{ \AA}$ , consisting of two layers of copper atoms separated by three layers of aluminum atoms.

The  $\theta''$  precipitates grow at a much slower rate than the GP zones. When the stress field surrounding the  $\theta''$  extends from one precipitate to the other, peak strength is reached. If ageing is continued from this point,  $\theta'$  precipitates with a chemical formula of  $\text{CuAl}_2$  begin to nucleate preferably on dislocations. The semi-coherent  $\theta'$  precipitates have a tetragonal structure with lattice parameters  $a = 4.04 \text{ \AA}$  and  $c = 5.80 \text{ \AA}$  [63]. The orientation relationships for the  $\theta'$  precipitates are  $(001)_{\theta'} \parallel (001)_{\text{Al}}$  and  $[001]_{\theta'} \parallel [001]_{\text{Al}}$ . The average size of the  $\theta'$  precipitates depends greatly on time and temperature, and ranges from 10 nm to 1  $\mu\text{m}$  diameter with a thickness of about 10 nm. The disc faces of the  $\theta'$  precipitates are still perfectly coherent with the matrix, but the disc edges are now incoherent.

If ageing is continued even further, the  $\theta$  phase nucleates at grain boundaries and at the surfaces of the  $\theta'$  precipitates. All of the  $\theta'$  precipitates dissolve, and transfer copper to the growing  $\theta$  phase. The completely incoherent  $\theta$  precipitates have a body-centered tetragonal structure with lattice parameters of  $a = 6.07 \text{ \AA}$  and  $c = 4.87 \text{ \AA}$ . It should be noted, from Fig. 2.7, that GP zones cannot form at ageing temperatures above 180°C.

The addition of ceramic particles into a metal alloy can markedly influence the age hardening response of a metal alloy. Upon quenching from the solutionizing temperature, the mismatch of the coefficient of thermal expansion (CTE) existing between the matrix alloy and the reinforcement creates thermal stresses, which cause local plastic deformation in the matrix. Consequently, dislocations are created at or near the particle/matrix interface. These dislocations can act as heterogeneous nucleation sites for the precipitation during the aging treatment. Precipitation is also affected by the vacancies produced during quenching. These quenched-in vacancies actually compete with the CTE dislocations and can also affect the aging response considerably.

The earliest publication reporting CTE induced dislocations in MMCs was that of Chawla and Metzger [64]. They noted that the Cu-W composite as fabricated contained enhanced dislocation density compared to the unreinforced alloy. A large difference in CTE, a high cooling rate, and a soft single crystal matrix amplified this effect.

Several models have been developed to estimate the dislocation density caused by the misfit strains of CTE mismatch in MMCs. Arsenault and Shi [20] conducted *in situ* high voltage electron microscopy (HVEM) experiments on SiC platelet reinforced 6061 aluminum alloys to observe the CTE dislocations and proposed a model in which prismatic punching of dislocations occurs at the ceramic/matrix interface. They noted that strengthening in the composites was not only due to CTE dislocations but also due to reduced subgrain size. The intensity of dislocation generation at the interface was found to be related to the size and shape of the SiC particles, and was lowest for small, spherical particles. The observed dislocation densities in the *in situ* experiments were lower than the actual densities because dislocations were lost through the surfaces of the thin HVEM foils during cooling.

These results were confirmed by Vogelsang et al. [65] in SiC whisker reinforced 6061 alloys. In contrast, however, they found that subgrain growth was not enhanced but hindered by the SiC particles.

Calorimetric techniques are also useful for understanding age-hardening reactions in aluminum alloy composites. Age-hardening sequences, the identity of the intermediate phases, the precipitate volume fractions and the reaction kinetics can be compared. Papazian [66] used differential scanning calorimetry (DSC) analyses to evaluate the effects of reinforcement addition in various aluminum alloys and their composites. He noticed accelerated kinetics of GP zone formation and intermediate phase formation in powder metallurgy control samples as well as the composites. The microstructural features introduced by

the powder metallurgy method (larger constituent and dispersoid particles, solute segregation, continuous oxide films formed around the reinforcement, finer grain size) greatly contributed to the acceleratory effect.

Transmission electron microscopy (TEM) studies of SiC whisker reinforced 2124 Al alloy composites by Christman and Suresh [67] revealed a significantly higher level of dislocation density compared to the unreinforced matrix alloy. The matrix microhardness curves of the composite displayed a threefold reduction in peak aging time. Precipitates were found to form preferentially at dislocation sites. No preferential precipitation or precipitate free zones were detected near the interfaces. It was also noted in this study that the difference in solute content between the composite and the control alloy would not affect the mechanisms underlying accelerated aging.

Dutta and Bourell [68] have indicated that both the residual stress state and the presence of CTE dislocations are both important contributors to accelerated aging.

Suresh et al. [69] evaluated the changes in microhardness of the composite matrix as a function of systematic and controlled aging treatments for several volume fractions of reinforcement in SiC particle reinforced Al-3.5 wt.% Cu composites. The unreinforced alloy and the matrix of the composites exhibited essentially the same matrix microhardness in the solutionized and as-quenched condition. However, the peak aging time for the matrix of the composites was approximately three times shorter when compared to the unreinforced alloy, and almost independent of volume fraction. A volume fraction of 6 vol.% was found to be high enough for the generation of CTE dislocations for accelerated aging. The results also showed that the presence of the excess CTE dislocations do not markedly contribute to strengthening despite the pronounced effect on aging.

The aging kinetics of Al-Cu alloys are found to be very sensitive to the aging temperature. Chawla et al. [70] studied the aging response of Al 2014 and the matrix of SiCp/Al 2014 at different aging temperatures. The reinforced alloy aged much faster than the unreinforced alloy at 195°C. However, the difference in aging between the matrix and the unreinforced alloy was minimal at 150°C. At aging temperatures of 165°C and above, the high dislocation density provided a short-circuit path for heterogeneous nucleation and the fast growth of the precipitates resulted in accelerated aging of the matrix. As the aging temperature is decreased, the difference in aging kinetics between the reinforced and unreinforced materials diminishes, due to homogeneous nucleation of GP zones and the decrease in the growth rate of the precipitates.

Lin and Wu [71] studied the aging kinetics of ingot-cast 2024 aluminum alloys reinforced with 14  $\mu\text{m}$  SiC particulates with volume fractions ranging from 5 to 20%. The time for peak hardness for the SiC/2024 composites decreased linearly with increasing volume fraction. DSC thermal analyses revealed that the addition of SiC did not change the sequence of the precipitation reactions in the alloy, but rather accelerated the process of aging. The DSC peak temperature for the S' precipitation reaction was also found to decrease linearly with increasing volume fraction.

Most studies regarding the aging of MMCs draw conclusions about the aging behavior from only one or two aging temperatures. Thomas and King [72] carried out aging experiments on SiC particle reinforced 2124 Al alloys over a wide range of temperatures, between 110 and 210°C. They observed accelerated aging in the MMC compared to the unreinforced alloy. The nucleation of GP zones was accelerated, but the growth of the zones was delayed. The enhanced diffusion of solute and increased density of heterogeneous nucleation sites increased the nucleation and growth of the S' precipitates.

When macrohardness measurements are made on particle-reinforced MMCs, the hardness contribution of the reinforcement will shift the whole aging curve to a higher hardness level. During aging, the reinforcement is not affected, and its effect on hardness is constant and no shift in the aging curve with time should occur, other than that caused by the matrix. The aging curves of the MMCs are therefore suitable for Arrhenius analyses, since only time and temperature are the only values used for activation energy calculations.

If it is assumed that (i) the peak hardness corresponds to the same level of transformation in each case and (ii) aging temperatures are low enough for the transformation to be diffusion controlled, then the activation energy for diffusion can be determined from the time to peak hardness. According to the Arrhenius equation for diffusion, for a given temperature, the diffusion coefficient is given by:

$$D = D_0 \exp\left(\frac{-Q}{RT}\right) \quad (2.8)$$

where  $D_0$  is a material constant,  $Q$  is the activation energy for diffusion,  $R$  is the universal gas constant, and  $T$  is the temperature. This can be rewritten as

$$\log D = \log D_0 - \frac{Q}{2.3RT} \quad (2.9)$$

The diffusion coefficient  $D$  may be replaced with  $1/t$  where  $t$  is the time to reach peak hardness, so that a plot of  $\log(1/t)$  against  $1/T$  over a range of temperatures should be linear with the gradient  $-Q/2.3R$ , allowing the calculation of the activation energy  $Q$ .

Using microhardness, electrical resistivity, differential scanning calorimetry and transmission electron microscopy, Dutta et al. [73] showed that the addition of Al<sub>2</sub>O<sub>3</sub> particle reinforcement into 2014 Al alloys accelerated the kinetics of GP zones and  $\theta'$  precipitation and decelerated the kinetics of  $\lambda'$  formation. The accelerated  $\theta'$  precipitation was the primary cause of the overall hardening kinetics of the composites. The peak matrix microhardness of the composite was actually lower than the monolithic alloy, due to the decrease in the volume fraction of  $\lambda'$  precipitates, and also due to interface reactions that depleted the amount of solute in the matrix. The accelerated aging was believed to be primarily caused by enhanced nucleation at CTE dislocations, and the pipe-diffusion-enhanced growth of  $\theta'$  precipitates.

In contrast, Dutta and Surappa [74] detected an acceleration of the room temperature aging response in a hot extruded Al-Cu/SiC composite by microhardness measurements, and interpreted this effect by considering the quenching stress. The quenching stress unlocked vacancies from vacancy-solute clusters, and led to the formation of excess vacancies. These excess vacancies helped GP zone formation and accelerated the natural aging kinetics of the composite when compared to the unreinforced alloy.

Badini et al. [75] used DSC curves in combination with Ozawa plots to study the aging kinetics of Al-Cu-Mg alloys and their composites. The addition of the SiC reinforcement shifted all of the transformations in the thermograms to lower temperatures. The total enthalpy for precipitation of the semicoherent phases was also lowered in the MMCs.

Increasing the reinforcing particle size increases the hardening rate during underaging while peak and overaging are not affected. Sannino and Rack [76] monitored the effect of SiC particle size on the age hardening response of 2009 aluminum by utilizing hardness, electrical conductivity, and differential scanning calorimetry data. GP zone formation was observed in the composite



containing 29  $\mu\text{m}$  SiC particles. The formation of these zones was eliminated in the composite containing 4  $\mu\text{m}$  particles. The decrease in reinforcement size increased the amount SiC/matrix interfaces. These interfaces acted as vacancy sinks, decreasing the vacancy supersaturation following quenching. This consequently decreased the formation of the GP zones.

Both particle size and volume fraction affect precipitation in particle reinforced aluminum alloys. Janowski and Pletka [77] examined the precipitation kinetics of SiC particle reinforced aluminum alloys in which they systematically varied both the particle size (24-142  $\mu\text{m}$ ) and volume fraction (9-27 vol.%) . In the 9 vol.% composites, the aging behavior was essentially the same as that of the unreinforced alloy, independent of particle size. The amount of thermal expansion misfit dislocations that were generated was insufficient to affect the aging behavior. The addition of 18 vol.% SiC accelerated the aging response in the composites, except for the 142  $\mu\text{m}$  composite, which roughly followed the aging curve of the unreinforced alloy. At 27 vol.% SiC, all of the composites showed similar accelerated aging behavior, such that a single curve could be drawn through the data points. It was concluded that small particles and high volume fractions were more effective in altering the aging behavior of the composites. Reinforcement additions exceeding a specific value led to a decrease in initial hardening due to the suppression of the GP zones.

Shakesheff [78] studied the tensile properties and aging behavior of Al-Cu-Mg and Al-Cu based alloys reinforced with 20 wt.% SiC particles. He observed higher strengths and moduli in the MMCs. Reductions in copper and magnesium levels in reinforced Al-Cu-Mg alloys from 4 to 2 % and 1.5 to 1 % respectively appeared to have no effect on the rate of age hardening, but resulted in lower peak strength values. The tensile properties were much less sensitive to accelerated aging effects, while grain refinement did not affect the tensile properties of the MMCs. However, for grain refinement, the addition of 0.6 % manganese seemed to be more effective as a grain refiner than the 0.12

% Zr addition. Notched tensile tests revealed that the Al-Cu MMCs were much tougher than the Al-Cu-Mg MMCs, due to the increased ductility of the Al-Cu matrix.

Using thermoelectric power (TEP) and internal friction measurements, Parrini and Schaller [79] concluded that the effect of the reinforcement was not to suppress GP zone formation, but to delay their precipitation. The capture of vacancies by the CTE dislocations present in the matrix was found to be the cause of delayed GP zone formation.

Chen and Chao [80] investigated the aging behavior of unreinforced 2024 alloys and 2024 alloy composites reinforced with 9 and 14 vol.% alumina fibers using DSC, TEM and microhardness data. They observed the suppression of GP zone formation in the composites, and attributed this behavior to the fiber-matrix interface acting as a vacancy sink during quenching. Rodlike undissolved phases were observed in both the unreinforced 2024 alloy and its composites. This undissolved phase was identified as a  $\text{Cu}_2\text{Mn}_3\text{Al}_{20}$  phase. DSC measurements indicated that GP zone formation was inhibited in the composites. No significant difference between the grain size of the unreinforced alloys and the composites could be observed, which indicated that a constant grain boundary "vacancy-sink" potential was existent for both the alloy and the composites. It was therefore clear that the fiber-matrix interfaces were responsible for the increased vacancy sink potential in the composites. The quenching of the composites into an ice-brine solution ( $-17^\circ\text{C}$ ) decelerated the diffusion to the sinks at the fiber-matrix interfaces, and GP zone formation increased. Microhardness results indicated that the composites and the unreinforced alloy reached peak hardness at the same time. The value of peak microhardness of the matrix (aged at  $190^\circ\text{C}$  for 8 hours) decreased with increasing volume fraction of fiber reinforcement. The reason was believed to be due to the suppression of the GP zone and  $S'$  phase formation in the matrix of the composites. In the DSC traces, both the composite and the

unreinforced 2024Al showed an S' phase formation peak at the same temperature, which indicated that the presence of reinforcement did not alter the kinetics of aging in the composites.

Massardier et al. [81], using thermoelectric power (TEP) and hardness measurements in combination with DSC experiments, found that the addition of alumina platelets into Al-Cu alloys significantly retards but does not suppress GP zone formation. The precipitated volume fraction was not affected by the presence of the platelets. It was proposed that the size of the zones were significantly altered in the composites. The delay in GP zone formation was also attributed to CTE dislocations and the reinforcement/matrix interface which acted as vacancy sinks.

Massardier and Merle [82] investigated the effects of the presence of ceramic particles in Al-Cu and 6061 (Al-Mg-Si) alloys. They noted that the modification of the precipitation kinetics of coherent phases due to the presence of reinforcement may depend on the nature of the alloying elements contained in the matrix. The introduction of alumina platelets in the Al-Cu alloy and in the 6061 Al alloy led to two separate effects. The GP zone formation in the Al-Cu/Al<sub>2</sub>O<sub>3</sub> composite was delayed, while a very slight modification was observed in the precipitation kinetics in the 6061/Al<sub>2</sub>O<sub>3</sub> composite.

The only important interactions for GP-zone formation appear to be those between the quenched-in vacancies and the sinks present in the matrix. These include interactions between the vacancies and the dislocations and/or interfaces, the vacancies and the solute atoms, the vacancies and GP zones and lastly the solute atoms and the dislocations. The interaction between the vacancies and the solute atoms was found to be an important factor. This interaction was weak in Al-Cu alloys, and the excess vacancies were free and mobile. As a result, the vacancies were easily trapped by the sinks within the

alloy. Precipitation kinetics from the quenched state was much slower in the matrix of the Al-Cu composite than in the unreinforced matrix. In 6061 Al alloys, the vacancy-solute interaction was strong, and vacancies associated with solute atoms and formed solute-vacancy pairs, which were less mobile than the free vacancies. In this case, precipitation kinetics was governed by the competition between the entrapment of these pairs by the sinks contained within the matrix and their entrapment by the zones. The latter process was predominant in the 6061 Al alloys. The defects introduced by the reinforcement were found to affect the precipitation only slightly.

While the tensile strength of a composite can increase with aging, the tensile ductility shows a different trend. Zhou and Duszczyk [83] found that the tensile ductility continuously decreased with aging time. They concluded that the  $\theta'$  phase was responsible for fracture as the size and number of the  $\theta'$  particles increase with aging time.

The kinetics of quenched-in vacancies and dislocation generation caused by thermal expansion mismatch may not be identical. In fact, the formation of precipitates involves the competition between CTE dislocations and vacancies as nucleation sites. Varma et al. [84] studied the effect of solutionizing time on the age hardening response of 2014 aluminum alloy composites and compared the results to the monolithic alloy. They observed larger grain sizes in the composites containing lower volume fractions of reinforcement. The time required for achieving peak hardness values in the unreinforced alloys and the composites increased with decreasing aging temperatures and increasing volume fraction. Increasing the solutionizing time for the unreinforced 2014 alloy decreased the time for peak-aging. However, for the composites, inconsistent behavior was observed. This behavior was again attributed to the competition between the quenched-in vacancies and the CTE dislocations.

Miserez et al. [85] studied the influence of heat treatment and particle shape on mechanical properties of infiltrated  $\text{Al}_2\text{O}_3$  particle reinforced Al–2 wt.-% Cu alloys. The tensile properties and fracture toughness of the high volume fraction particulate MMCs depended strongly on the intrinsic particle characteristics, including shape, processing route, and size. Larger reinforcements yielded tougher composites while smaller particles increased the composite yield stress. Heat treatment affected the toughness more when compared to the tensile strength. The most significant improvement was obtained by the solutionizing heat treatment: the dissolution of the  $\theta$  phase greatly improved the mechanical properties.

Composites reinforced with sub-micron particles show similar accelerated aging behavior as well. Longtao et al. [86] examined the aging response of nearly spherical  $0.3 \mu\text{m}$   $\text{Al}_2\text{O}_3$  particle reinforced 2024Al composites. With the addition of the  $\text{Al}_2\text{O}_3$  particles, hardness was greatly improved. The hardening efficiency of the composite however was lower than that of the monolithic alloy. The formation of the GP zones were suppressed in the composite, and the activation energy for the thermal diffusion of the  $S'$  phase was increased which made the precipitation of  $S'$  more difficult. The number and size of the precipitates were also smaller.

### **2.4.3. Property Estimation for MMCs**

Low density MMCs can be readily developed by selecting low density alloys, such as those based on aluminum and magnesium for the matrix material. When structural requirements demand optimal strength to density ratios in combination with thermal stability, nickel and titanium alloys can also be selected. But before production, estimating the performance of a composite from its constituents is an important consideration.

Numerous mathematical models have been formulated regarding the prediction of properties of composites from their individual components. The simplest and most commonly used model is the rule of mixture (ROM) approximation, which assumes that the CTE, density, strength, modulus or any desired property of the MMC can be computed from the weighted average of the individual components:

$$\alpha_c = \alpha_m V_m + \alpha_r V_r \quad (2.10)$$

where  $\alpha$  is the property of interest,  $V$  is the volume fraction, and the subscripts  $c$ ,  $m$  and  $r$  refer to the composite, matrix and reinforcement, respectively. Limitations of the ROM approximation have resulted in correlations which take additional factors into account.

**i. Density:** When a volume fraction of  $V_r$  of reinforcement  $r$  (and density of  $\rho_r$ ) is mixed with a volume fraction  $V_m$  of a matrix  $m$  (and density of  $\rho_m$ ) to form a composite with no residual porosity or void-space, the composite density is given exactly by the rule of mixtures (an arithmetic mean, weighted by volume fraction)

$$\rho = V_m \rho_m + V_f \rho_f \quad (2.11)$$

**ii. Modulus:** The modulus of the composite is bracketed by the well known Voigt and Reus [87] bounds. The upper bound is obtained by postulating that, on loading, the two components suffer from the same strain; the stress is then the volume average of the local stresses and the composite modulus follows the rule of mixtures

$$E_u = V_m E_m + V_f E_f \quad (2.12)$$

Here  $E_r$  is the Young's modulus of the reinforcement and  $E_m$  is the modulus of the matrix. The lower bound is found by postulating instead that the two components carry the same stress; the strain is the volume average of the local strains and the composite modulus is

$$E_l = \frac{E_m E_r}{V_m E_m + V_f E_f} \quad (2.13)$$

There are better, more closely spaced bounds that are contained between the two given above, which are completely adequate for most cases. Bounds exist for shear moduli and Poisson's ratio as well.

**iii. Strength:** As load on a composite is increased, the load is redistributed between the components until general yield or fracture occurs. Beyond this point the composite has suffered permanent deformation or damage; we define it as the strength of the composite. The composite is strongest if both components reach their failure state at the same time (since if one fails before the other the weaker determines the strength). Thus the upper bound is, as with modulus, a rule of mixtures

$$(\sigma_f)_u = V_r (\sigma_f)_r + V_m (\sigma_f)_m \quad (2.14)$$

where  $(\sigma_f)_m$  is the strength of the matrix and  $(\sigma_f)_r$  is the strength of the reinforcement.

A lower bound is more difficult. The literature contains many models and calculations for special cases [88-91]. One model consistent with the restriction that the components of the composite do not separate at their interfaces, describes a "worst case", a continuous, ductile matrix containing strong reinforcing particles; the lower limit for the composite is then the yield strength

of the matrix enhanced slightly by plastic constraint imposed by the reinforcement:

$$(\sigma_f)_l = 1 + \frac{1}{16} \left( \frac{V_r^{1/2}}{V_m^{1/2}} \right) \quad (2.15)$$

The bounds are wide but still allow important conclusions to be reached.

**iv. Specific Heat:** The specific heats of solids at constant pressure,  $C_p$ , are almost the same as those at constant volume,  $C_v$ . If they were identical, the heat capacity per unit volume of the composite would be given exactly by the rule of mixtures

$$\rho C_p = V_r \rho_r (C_p)_r + V_f \rho_f (C_p)_f \quad (2.16)$$

where  $(C_p)_r$  is the specific heat of the composite and  $(C_p)_m$  is that of the matrix. A slight difference appears because thermal expansion generates a misfit between the reinforcement and the matrix during heating; the local pressures generated changes the specific heat. This effect is generally very small [92,93].

**v. Coefficient of Thermal Expansion:** Whereas most metallic matrices exhibit reasonably high thermal conductivities, their coefficient of thermal expansion (CTE) values are substantially higher than most of the reinforcements available. Very low CTEs can be achieved when high volume fractions of reinforcement (~40 vol.%) are used for the fabrication of the MMC. Considering the effects of isostatic stress [94], the CTE of the composite can be computed from:



$$\alpha_l = \frac{\alpha_m V_m K_m + \alpha_r V_r K_r}{V_m K_m + V_r K_r} \quad (2.17)$$

where  $\alpha_r$  and  $\alpha_m$  are the expansion coefficients and  $K_r$  and  $K_m$  are the bulk moduli of the reinforcement and the matrix, respectively. The CTE predicted by this model is significantly lower than that predicted by the ROM approximation. A more complicated model which takes into account the effects of shear stresses between the matrix and isotropic, approximately spherical reinforcements estimates the CTE as

$$\alpha_u = \alpha_m - \left( \frac{A}{B} \right) V_r (\alpha_m - \alpha_r). \quad (2.18)$$

in which

$$A = K_m (3K_r + 4\mu_m)^2 + (K_r - K_m) (16\mu_m^2 + 12\mu_m K_r) \quad (2.19)$$

and

$$B = (3K_r + 4\mu_m) [4V_r \mu_m (K_r - K_m) + 3K_m K_r + 4\mu_m K_r]. \quad (2.20)$$

where  $\mu_m$  is the shear modulus. The measured CTE values of MMCs generally lie between these two bounds.

**vi. Thermal Conductivity:** The thermal conductivity,  $\lambda$ , determines the heat flow at steady state. A composite of two materials, bonded to give good thermal contact, has a thermal conductivity  $\lambda$  which lies between those of the individual components,  $\lambda_m$  and  $\lambda_r$ . A composite containing parallel continuous fibers has a conductivity, parallel to the fibers, given by the rule of mixtures

$$\lambda_u = V_r \lambda_r + V_m \lambda_m. \quad (2.21)$$

This is an upper bound. In any other direction the conductivity is lower. The transverse conductivity of a parallel-fiber composite (again assuming good bonding and thermal contact) lies near the lower bound

$$\lambda_t = \lambda_m \left( \frac{\lambda_r + 2\lambda_m - 2V_r(\lambda_m - \lambda_r)}{\lambda_m + 2\lambda_m + V_r(\lambda_m - \lambda_r)} \right) \quad (2.22)$$

Particulate composites, too, have a conductivity near this bound [87,93,95]. Poor interface conductivity makes  $\lambda$  drop below the lower bound. Debonding or an interfacial layer between the reinforcement and the matrix can cause this. A large difference of modulus between the reinforcement and the matrix (because this reflects phonons, creating an interference impedance), or a structural scale which is shorter than the phonon wavelengths.

**vii: Thermal Diffusivity:** The thermal diffusivity

$$a = \frac{\lambda}{\rho C_p} \quad (2.23)$$

determines the heat flow when conditions are transient, that is, when the temperature field changes with time. It is formed from three of the earlier properties:  $\lambda$ ,  $\rho$ , and  $C_p$ . The second and third of these are given exactly by equations (2) and (6), allowing the diffusivity to be expressed as

$$a = \frac{\lambda}{V_r \rho_r (C_p)_r + V_m \rho_m (C_p)_m}. \quad (2.24)$$

Its upper and lower bounds are found by substituting those of  $\lambda$  from equations (11) and (12).

**viii: Toughness and Fracture Toughness:** It is difficult to model toughness for composites. The choice of fracture toughness  $K_{Ic}$  or the quasi-strain energy release rate  $J_{Ic}$  as a design property for composites is itself questionable. Particulate composites often fail by the propagation of a single crack through the matrix which is elastic except for a small zone at the crack tip; for these,  $J_{Ic}$  and  $K_{Ic}$  are meaningful [96]. But for fibre-reinforced composites, failure often occurs by multiple matrix-cracking, by crack deflection, by splitting parallel to the fibres (even when the starting crack is normal to them), by local delamination, or by the formation of extensive damage zones which diffuse the stress concentration associated with a crack or notch.

The upper and lower limits for the toughness  $J_{Ic}$  for relevant composites are widely separated because they are based on the “best” and “worst” cases. Let us consider a mode I crack in a composite with components of toughness  $(J_{Ic})_r$  and  $(J_{Ic})_m$ . The worst case is that of a crack in the component of lower toughness which is able to propagate on a path which avoids the other, tougher, component altogether. If the less tough component is thought of as the matrix, then a lower limit for composite toughness is

$$(J_{Ic})_l = (J_{Ic})_m \left( \frac{(1 + 2V_r)^{1/2}}{1 - V_r^{1/2}} \right), \quad (J_{Ic})_l < (J_{Ic})_r \quad (2.25)$$

The toughness of the composite initially increases slowly with increasing volume fraction of reinforcement. If the crack is to avoid the reinforcement, it becomes increasingly wavy, (and thus longer) and this waviness introduces some mixed mode loading, which causes the slight increase in toughness. The value of  $(J_{Ic})_l$  is cut off at the value of  $(J_{Ic})_r$  of the reinforcement since the crack will then penetrate the reinforcement. If the crack propagated instead in

the interface between the matrix and the reinforcement, an even lower toughness could result.

The upper limit is derived by considering crack bridging. Bridging is the spanning of the opening crack by restraining material: fibers which pull out, ductile particles which stretch plastically, or rigid inclusions which must be extracted from the crack faces against friction. Bridging can lead to a composite toughness which is much greater than that of either component – an effect exploited in some fiber reinforced polymers, and also in natural materials such as antler and shell. The approximate result is given by

$$(J_{1c})_u = V_r (J_{1c})_r + V_m (J_{1c})_m + \left( \frac{V_f V_m E^*}{40} \right)^2 \frac{\pi a^*}{E_u} \quad (2.26)$$

where  $E^*$  is the modulus of the bridging component, and  $2a^*$  the length of the largest acceptable crack in the component. The first two terms on the right describe a rule of mixtures; the last term is the additional energy absorbed by the work done against the bridging forces. Corresponding values of fracture toughness,  $K_{1c}$ , for a component with a maximum crack length of 10 mm, are given by

$$(K_{1c})_l = [E_l (J_{1c})_l]^{1/2} \quad (2.27)$$

and

$$(K_{1c})_u = [E_u (J_{1c})_u]^{1/2}. \quad (2.28)$$

Much detail is ignored in deriving these limits. The limits are not precise, but real data obtained would probably be bracketed by them.

## **2.5. The Future Of MMCs**

MMCs first emerged as a technology in a time when improved performance for advanced military systems was the primary motivation for materials development. In such a condition, improved affordability and more widespread commercialization followed from the knowledge gained from the engineering, production and service of these materials in military applications. While some MMC applications were established in this early period, MMCs were still a relatively less-developed technology by the early 1970s. In the late 1970s, recession in many developed countries began to reduce funding for research and development, and increased emphasis was brought to affordability. Many companies refrained from taking risks for the development of advanced high-performance materials.

The research and development of MMCs revived in the 1980s, mostly due to efforts in the field of discontinuously reinforced MMCs, which greatly expanded the scope of these materials. The improvement in performance obtained by discontinuous reinforcement was lower than that obtained by continuous reinforcement, but the affordability and processing options for these materials provided a great opportunity for their use in commercial applications. Most of the attempts in the MMC industry were focused on achieving a balance between performance and affordability, at a risk acceptable to the commercial sector. Continuously reinforced MMCs were also widely studied and developed, mostly in the support of high profile government programs.

Many new MMC applications were established in the two decades, most of them having found areas in the commercial sector. The most important MMC applications were in the ground transportation (auto and rail), thermal management, aerospace, industrial, recreational and infrastructure industries have now been enabled by functional properties that include high structural efficiency, excellent wear resistance, and attractive thermal and electrical

properties. Several technical challenges have been overcome, including compatibility between the reinforcement and the matrix, affordable primary and secondary processing techniques capable of controlling reinforcement distribution, engineering design methodologies, and characterization and control of interfacial properties. But although MMCs are now an established materials technology, the MMC sector is nevertheless a dynamic industry which has a growth depending on its applications and competing technologies.

In early applications, MMCs were selected because they offered the best overall solution in a comparison between different materials for a particular application. These applications are typically characterized as point insertion, where material substitution is made to overcome some deficiency of the original material while maintaining the overall form, fit and function of the original design. The growing commercial importance of MMCs results less from any fundamental shift in the nature or capabilities of the MMCs and more from the fact that they compete successfully in a broad range of applications.

Continued process and manufacturing improvements to lower intrinsic cost remain to be the most important issues to be overcome for expanding the commercial importance of MMCs. Established approaches include selective reinforcement, point of use MMC production, and integration of material production with component manufacture. Continued application of an integrated system design approach, complementing a point of insertion methodology, is also necessary to achieve the full commercialization of MMCs. Continued standardization, outreach and education of the engineering design community to reduce non-technical barriers to insertion which are usually the result of insufficient local knowledge and experience.

Many MMC materials that have not been investigated beyond the conceptual stage offer rich opportunities for future research and development. Metallic glasses offer compelling strength and unique properties not provided by any

other material system. However, in bulk form these materials have very limited ductility. Composite microstructures have been shown to provide dramatic improvements in ductility while retaining most of the attractive properties of the metallic glass, so that metallic glass composites offer an important opportunity. Nanostructured composites also have potential for future use: in addition to high strength, many nanostructured composites offer exceptional microstructural stability, even at very high temperatures, due to the existing secondary phases that restrict grain growth. Shape memory alloys and magnetic metals offer important functionalities. MMCs incorporating these metals are rare, but they would provide an opportunity for future multifunction applications.

The tailoring of the composite microstructure has been underutilized in the current generation of MMCs [96]. Bimodal reinforcement sizes that span length scales and influence the different mechanisms of strengthening have been introduced but have not been investigated in detail. This combination can be expanded to include the combination of dispersoids, particulates, whiskers, platelets, fibers and/or laminates to achieve simultaneous effects. Some studies have shown that intentional macroscopic heterogeneity of reinforcement volume fractions can provide unexpected improvements in fracture properties. Intentional and controlled inhomogeneity in the micro scale remains unexplored with the exception of functionally graded materials. Combined intentional heterogeneity in matrix grain size, reinforcement size and distribution provide ample opportunities for research. Foam architectures provide additional opportunities for hybrid materials and structures. Reinforced metal foams with reinforcements that span many foam cells can retard a major mode of foam deformation and failure.

### 2.5.1. MMCs for Armor Applications

Weight reduction for present and future army systems is crucial to the survivability of future army vehicles. The key element in the development of these modern armor packages is the development of composite armors. Composite armors are a class of laminated composites which usually consist of a hard frontal (facing) plate combined with a ductile and softer backing. The former is usually a ceramic (namely  $\text{Al}_2\text{O}_3$ ,  $\text{B}_4\text{C}$ ,  $\text{SiC}$ ,  $\text{TiB}_2$ ) and the latter is usually either an FRP, an MMC, Kevlar, or aluminum [97-102].

The investigation of ceramic armors against light and medium threats has a long history, dating back to the 1960s [103,104]. The principles governing the defeat mechanisms and design parameters against such threats are now generally understood. However, achieving similar armor performance against large caliber, kinetic energy (KE) penetrator threats present a difficult challenge.

The perforation of ceramic armor occurs in three distinct stages: shattering, erosion, and catching.

**i. Shattering:** In this phase, the penetrator fractures on the surface of the ceramic plate. The high compressive strength of the ceramic outmatches the load of the penetrator, and the penetrator material flows and shatters. This initial stage is followed by a period of damage accumulation in the ceramic material initiated by tensile wave reflections, and bending of the ceramic tile and the backing plate.

**ii. Erosion:** During this phase, the ceramic material is cracking, but the ceramic still contributes to the defeat of the penetrator by erosion mechanisms. The combination of the shattering and erosion phases is frequently called the “dwell” phase [104].



**iii. Catching:** In this final phase, the ceramic has lost considerable strength, but the ceramic and backing combine to reduce the velocity of the penetrator through momentum transfer mechanisms. The backup component also serves to absorb residual projectile fragments and comminuted ceramic particles.

The ballistic performance of a ceramic armor depends on its constructive environment, often called the confinement [105]. The confinement is capable of maintaining a uniform compressive state within the ceramic [106] so that highest levels of strength can be obtained.

Metal backed ceramic armors are most usually constructed using polymer adhesives. Joining with adhesives is convenient because it is performed near room temperature, in air, and is compatible with most materials. The drawbacks of adhesive bonding are the low bonding strength and the low acoustic impedance [99,106]. The combination of low modulus and low density creates a substantial impedance mismatch with the ceramic and metal substrates. The change of impedance at the adhesive layer gives rise to a strong tensile reflection into the ceramic which tends to shatter it and provide energy for ejection of the shattered material. Moreover, a strong shear wave is set up at the interface which serves to “unzip” the adhesive interface [106,107]. The class of adhesives with acoustic match nearest to metals and ceramics are known to be high-temperature use ceramic adhesives.

Other bonding methods intended for decreasing the acoustic impedance mismatch are brazing, soldering, casting, and hot isostatic pressing (HIP). However, these techniques have proven to be more expensive, compared to the aforementioned adhesive joining techniques [99-104].

For obtaining the best level of protection, it is known that using the hardest frontal material will most usually provide the best level of ballistic protection. However, a hard material is also typically brittle, and exhibits a large collateral

damage from dynamic impact. This eventually limits the point-to-point multihit capability of such an armor scheme. Recently, research has been focused on the development of MMCs for armor applications [101]. It is believed that MMCs with tailored ceramic-to-metal through-thickness gradients known as functionally graded materials (FGMs) may be attractive candidates for low-cost and near-net-shape armor applications.

## CHAPTER 3

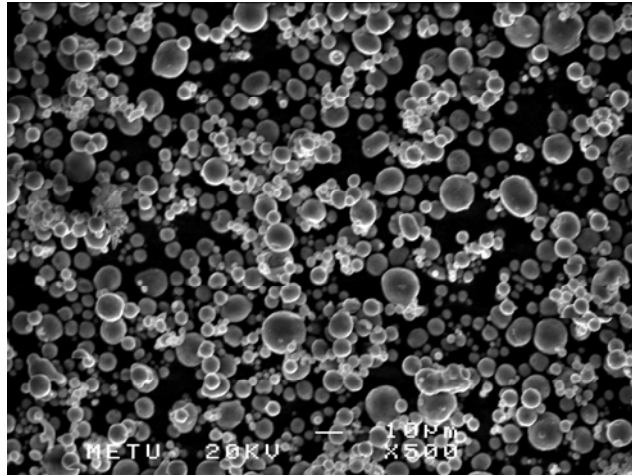
### EXPERIMENTAL

#### 3.1. Materials

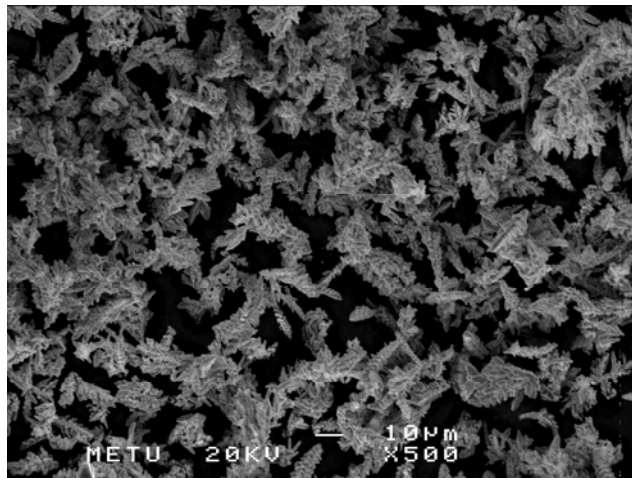
The matrix alloy and the composite materials were prepared by the powder metallurgy (P/M) methods. Aluminum powder was a commercial grade pure powder. The elemental powders of copper were obtained from Sigma-Aldrich Corporation. The boron carbide ( $B_4C$ ) powders were purchased from the Electro Abrasives Corporation. Aluminum is a popular light alloy powder used in P/M, primarily due to its low cost, and was therefore chosen as the matrix alloy.  $B_4C$  was chosen as the reinforcement due to its very high hardness (2900 HV). Also, both Al and  $B_4C$  have low densities, which is  $2.70 \text{ g/cm}^3$  for aluminum and  $2.52 \text{ g/cm}^3$  for  $B_4C$ . The age hardenable Al - 4 wt.% Cu alloy was selected as the matrix alloy for the aluminum matrix composites. The volume fraction of  $B_4C$  in the Al - 4 wt.% Cu /  $B_4C$  composites was varied from 0 vol.% to 40 vol.%.

To understand the morphology of the powders, sample powders were dropped on double-coated adhesive carbon discs and examined under a JEOL JSM-6400 electron microscope.

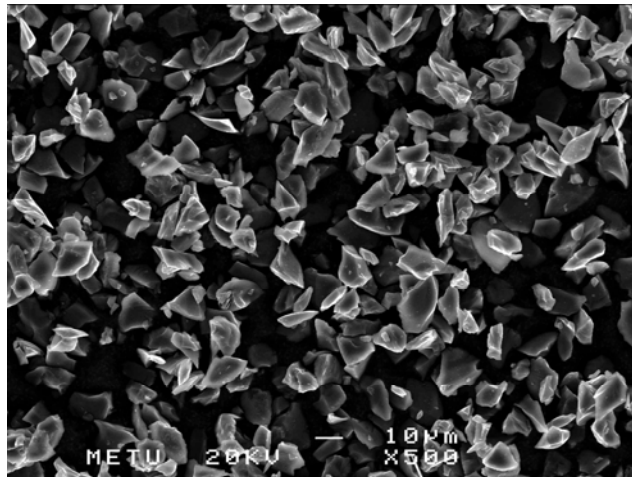
The scanning electron micrographs of the powders are shown in Fig. 3.1. The shape of the aluminum, copper, and  $B_4C$  powders were spherical, dendritic, and angular, respectively. The electron images of the powders were also useful for obtaining an estimate of average particle size.



(a)

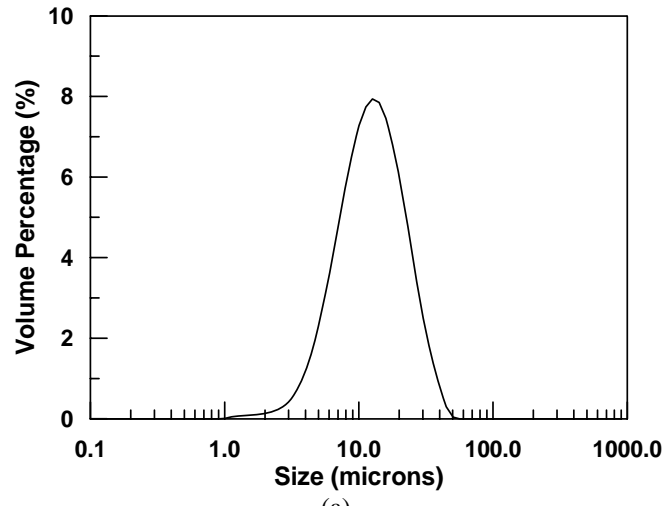


(b)

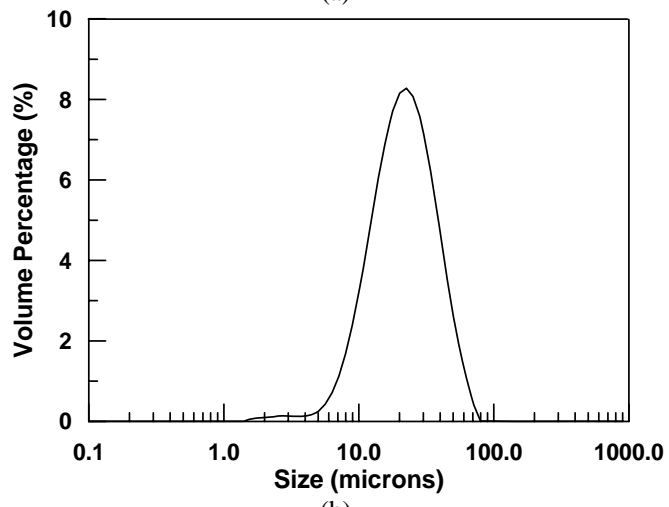


(c)

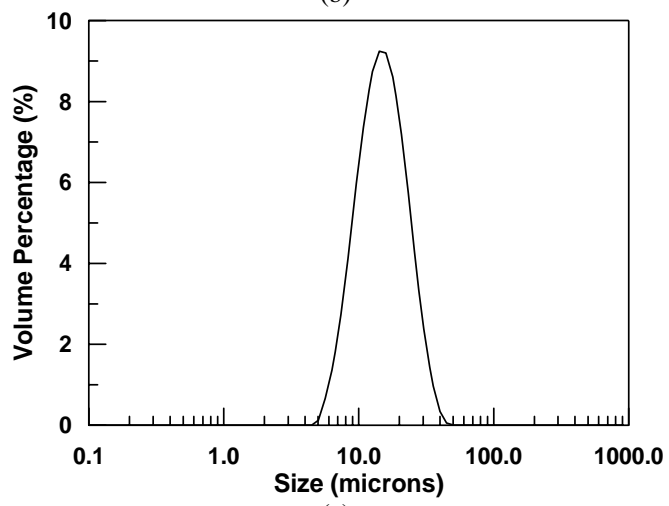
Fig. 3.1. Morphology of the (a) aluminum, (b) copper and (c) B<sub>4</sub>C carbide particles used.



(a)



(b)



(c)

Fig. 3.2. Plots showing the size distribution of the Al (a), the Cu (b), and the B<sub>4</sub>C (c) particles.

The size distribution of the particles was measured using a Malvern Mastersizer 2000 laser diffraction particle size analyzer. Three experimental runs were carried out for each powder type and then averaged. The results are shown in Fig. 3.2. The average particle sizes of the aluminum, copper and boron carbide powders were measured as 14, 24, and 14  $\mu\text{m}$ , respectively.

The average particle size measured by the laser diffraction particle size analyzer for copper was erroneous, due to the dendritic morphology of the powder. As seen in Fig. 3.1(b), the copper particles have large aspect ratios, with diameters of approximately 3  $\mu\text{m}$ . It seems that the measurement obtained from the particle size analyzer more likely reflects the length, not the diameter, of the copper particles.

### **3.2. Fabrication of the MMCs**

For the production of the composites, an electric furnace was built. The ceramic components of the furnace were made with castable alumina, which consists of alumina powder (max. 3 mm diameter) and binding agents. The casting procedure consisted of mixing the powder with an appropriate amount of water and casting the mixture into a Teflon coated mould.

After casting, the part was dried for 48 hours in air, dried at 150°C for 24 hours and sintered at 600°C for 12 hours. The cavities in the ceramic mould, which were necessary for the electrical resistance wires, were created by the lost-wax method, using wax tubes of 10 mm diameter. The photographs of the mold and the sintered ceramic are shown in Fig. 3.3.

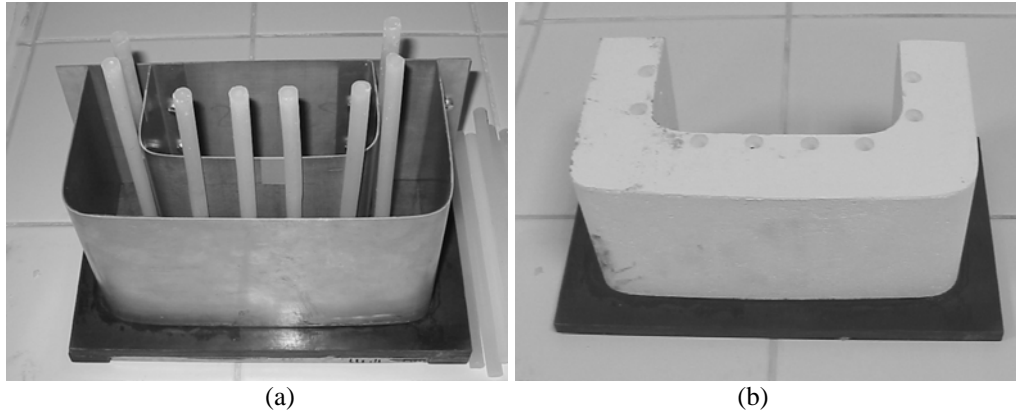


Fig. 3.3. (a) The mold for casting the ceramic and (b) the appearance of the ceramic after sintering.

After the ceramic was sintered, the 1 mm diameter electrical resistance wires were coiled to 8 mm diameter and wound through the cavities. The ceramic was then surrounded by 50 mm thick insulating fiberboards. Finally a metal case was manufactured to hold the whole system intact.

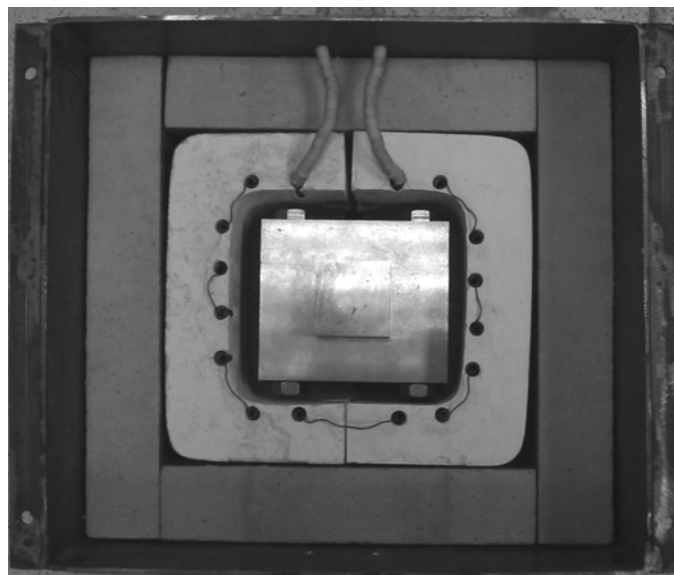


Fig. 3.4. Top view of experimental setup used for composite production.

A die with an inner square cross-section of 50 mm length made of an H13-grade hot work tool steel (hardness: 52 R<sub>c</sub>) was designed and manufactured for the cold compaction and sintering of the powders. Figure 3.4 shows the top view of the furnace along with the steel die.

The elemental powders of aluminum and copper were blended with the B<sub>4</sub>C particles in appropriate amounts in a plastic 50 mm diameter container and mixed in a variable speed horizontal ball mill at a rotation speed of 140 rpm for 1 hr.

Powder lubrication (such as the addition of zinc stearate or stearic acid) was not applied to the powders; instead, die wall lubrication was applied by brushing a high-temperature paste (Molykote P37) on the inner surfaces of the die. The die lubricant was effective in reducing the ejection (stripping) pressure and die wear.

Pressure was applied onto the die punch using a 30-ton capacity hydraulic press. The powders were initially cold compacted at a pressure of 50 MPa. Hot pressing/sintering was done at 25 MPa constant pressure for 10 min. under inert nitrogen atmosphere. The nitrogen gas was sent through inlets at the bottom of the furnace. Depending on the volume fraction of B<sub>4</sub>C, different hot pressing temperatures were chosen. These temperatures are listed in Table 3.1. The matrix alloy (the sample containing 0 vol.% B<sub>4</sub>C), the 10 vol.% and the 20 vol.% B<sub>4</sub>C composites were all hot pressed at the same temperature, i.e. at 585°C. On the other hand, the 30 vol.% and 40 vol.% composites were pressed at 590°C and 600°C respectively.



**Table 3.1.** The temperatures chosen for hot uniaxial pressing.

B <sub>4</sub> C <sub>p</sub> Volume Fraction (vol.%)	Temperature (°C)
0 vol.% (unreinforced)	585
10 vol.%	585
20 vol.%	585
30 vol.%	590
40 vol.%	600

After the pressure was released, the die - along with the specimen - was immediately taken out of the furnace and cooled in air. The final dimensions of the fabricated composites were 50 x 50 x 10 mm. After cooling, a final grinding step was applied to the composites to remove the fine scale at the surface. This scale was probably formed by reaction with the die lubricant. The final sintered dimensions of the composites were approximately 50 x 50 x 10 mm.

### 3.3. Heat Treatments

Samples having dimensions of 15 x 15 x 10 mm were cut from the original specimens and solutionized in a muffle furnace at 515°C for 12 hours. The specimens were then quenched in water, grinded and polished to a mirror finish, and aged at temperatures ranging from 100°C to 175°C, utilizing a Julabo SC-12 heating circulator (Fig. 3.5) with 0.1°C sensitivity. Aging the Al - 4 wt.% Cu alloy at a temperature above than 180°C was not attempted, as peak strength cannot be reached at this aging temperature.



Fig. 3.5. The Julabo SC-12 oil bath, used for aging treatments.

A silicon-base oil (Julabo Thermal H) was used as the aging medium. The total duration of each aging experiment was 32 hours, but hardness measurements from the specimens were taken every four hours.

### **3.4. Hardness Tests**

Vickers hardness measurements were made using an EMCO M4U-025 digital hardness testing machine under 10 kgf. load. The hardnesses were taken at every 4 hours of the aging process. The 10 kgf load ensured that the indentation was large enough not to be influenced microstructural heterogeneities. It must be noted though, that the indenter may also be influenced by subsurface particles as well. Six hardness readings were taken from the samples at each aging interval.

### 3.5. Differential Scanning Calorimetry

Differential scanning calorimeter (DSC) determinations were performed using a Perkin-Elmer Pyris 1 DSC instrument at a heating rate of 40°C/min. The specimens to be used for the DSC analyses were solutionized at 515°C for 12 hours and quenched in water. Wafers of 1 cm<sup>2</sup> area were cut from the original specimens and then ground using 600 grit abrasive papers to a thickness of 500 μm. Super purity aluminum was used as a reference. In the DSC traces the heat of evolution (or absorption) is plotted as a function of temperature, and a precipitation reaction therefore reveals itself as an exothermic peak.

### 3.6. Transverse Rupture Tests

A transverse rupture test fixture was designed for measuring the sintered strength of the MMCs, in both as-fabricated and heat treated condition, according to the ISO 3325-1975 standard [99]. Additionally, a 2024-T851 aluminum alloy (purchased from Kaiser Aluminum) was also tested for comparison purposes. The testing fixture was manufactured from a D2 grade cold work tool steel heat treated to 52 Rc, and mounted onto a 1-ton capacity Schimadzu AGS-J Autograph Tester (Fig. 3.6).

In the flexural strength tests, the maximum normal stress is calculated by the following equation:

$$\sigma_{\max} = \frac{Mc}{I} \quad (3.1)$$

where  $M$  is the moment of inertia,  $c$  is the distance from the neutral fiber to the extreme fiber, and  $I$  is the bending moment [100,101].

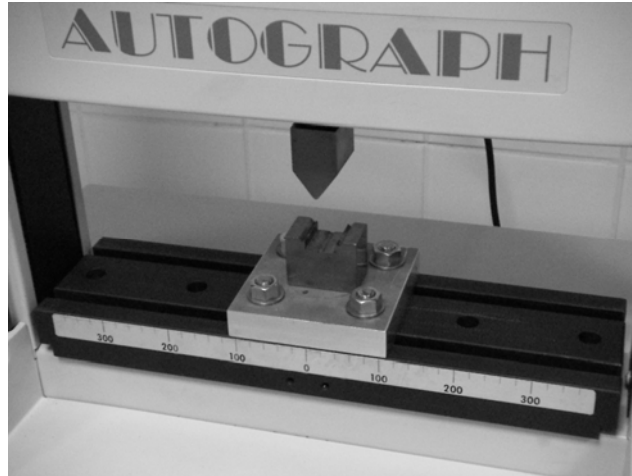


Fig. 3.6. The Shimadzu AGS-J Autograph Tester with the transverse rupture test fixture.

The strain rate at the outer fiber is determined by assuming small plastic deformation and neglecting shear [102,103], using the following expression:

$$\dot{\varepsilon} = \frac{12vc}{L^2} \quad (3.2)$$

where  $v$  is the crosshead velocity and  $L$  is the span. The composites were tested at 5 different strain rates:  $5 \times 10^{-4} \text{ s}^{-1}$ ,  $1.5 \times 10^{-3} \text{ s}^{-1}$ ,  $5 \times 10^{-3} \text{ s}^{-1}$ ,  $1.5 \times 10^{-2} \text{ s}^{-1}$ , and  $5 \times 10^{-2} \text{ s}^{-1}$ . Test specimens having dimensions of 32 x 12 x 6 mm were machined from the produced composites. Six tests were made for each experimental condition, and then averaged.

### 3.7. Ballistic Tests

The heat treated 50 x 50 x 10 mm composites were tried as frontal plates of a composite armor. 2024-T851 aluminum alloy plates of 6.35 mm thickness were purchased (from Kaiser Aluminum) to be used as backing plates for the composite armors. These plates were cut to 90 x 90 mm dimensions for testing.

Polyurethane adhesives (Sikaflex 228) were used to bind the composite plates to the 2024-T851 backing plate. Figure 3.7 shows a ready to use target armor configuration.

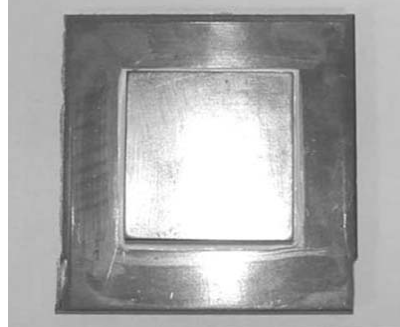


Fig. 3.7. The target armor configuration.

Target fixtures for holding the target armor in its position were made from a normalized AISI 1118 grade steel. In addition to the composites that were used as facing plates, hot-pressed B<sub>4</sub>C plates (of 50 x 50 x 10 mm dimensions) were also obtained from the Hesfibel Corporation in order to compare the results of the composites.



Fig. 3.8 The automatic G3 infantry rifle.

Ballistic tests of the composite specimens were performed in the ballistics laboratory of the Silahsan Corporation. Armour-piercing (AP) rounds of  $7.62 \times 51$  mm M61 type were fired on the composite armors utilizing a G3 infantry rifle (Fig. 3.8). A schematic of the 7.62 mm projectile is shown in Fig 3.9. The projectile consists of a jacket, and a 4.63 gr AISI E 52100 steel core with a hardness of 62 HRC. The total weight of the round was 9.75 gr. The strong penetration capability of the penetrator arises from its hard steel core.

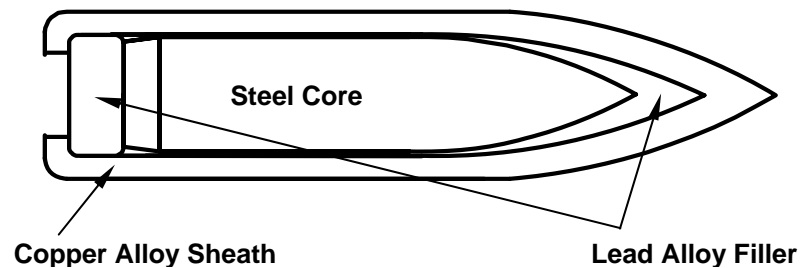


Fig. 3.9. Basic components of the 7.62 mm (0.30 caliber) AP round.

Three specimens were tested for each experimental condition and the results were averaged. The target armors were located 15 m away from the projectile exit region. The projectile velocity, which is  $805 \pm 15$  m/s, was measured utilizing light screens (Fig. 3.10), by allowing the bullet to interrupt two infrared (IR) beams at a known distance apart.



Fig. 3.10. The two light screens used for velocity measurements.

The outputs from two photodiodes illuminated by the IR beams were fed into a Drello BAL 3003 speed computer (Fig. 3.11), which measured the duration for which the bullets traveled from one beam to the next and calculated the average velocity.

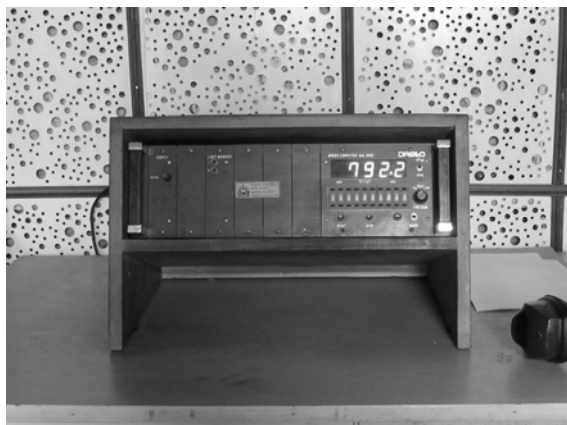


Fig. 3.11. The Drello BAL 3003 speed computer which was connected to the light screens.

The exit velocity of the projectile was also measured, utilizing a TÜBİTAK ZÖS time measurement system, which was of similar construction as the Drello BAL 3000, except the fact that it used A3 size paper screens instead of light screens. The paper screens were renewed for each ballistic test.

### **3.8. Metallography**

The samples that were used for hardness measurements were also examined in detail by optical and scanning electron microscopy (SEM). The scanning electron microscope used was a JEOL JSM-6400 model SEM equipped with a NORAN System 6 X-ray Microanalysis System. The SEM was also used for the fractography of the transverse rupture samples. The grain structure of the polished metallography samples were revealed by etching the polished surfaces with concentrated NaOH.

Transmission electron microscopy (TEM) of the aged samples were carried out in order to determine the precipitation mechanisms. Samples approximately 1 mm thick were cut with a diamond saw and mechanically ground to a thickness of less than 500  $\mu\text{m}$ . Then 3 mm diameter discs were punched out and mechanically polished to a thickness of about 30  $\mu\text{m}$  in the center using a VCR dimpler. Final thinning was carried out by argon ion plasma bombardment using a GATAN Model 600 ion miller using a liquid nitrogen stage until perforation occurred. The thinned samples were then observed in a Philips CM-30 transmission electron microscope (TEM).

### **3.9. Fractography**

The fracture surfaces of the transverse rupture specimens were observed by scanning electron microscopy. Both secondary electron and backscatter



electron imaging was utilized in order to reveal the topography and the composition of the fracture surfaces respectively.

The impact surfaces of the ballistic test samples were photographed. Both the entry and exit faces of the composite armors and the B<sub>4</sub>C ceramic armor were examined.

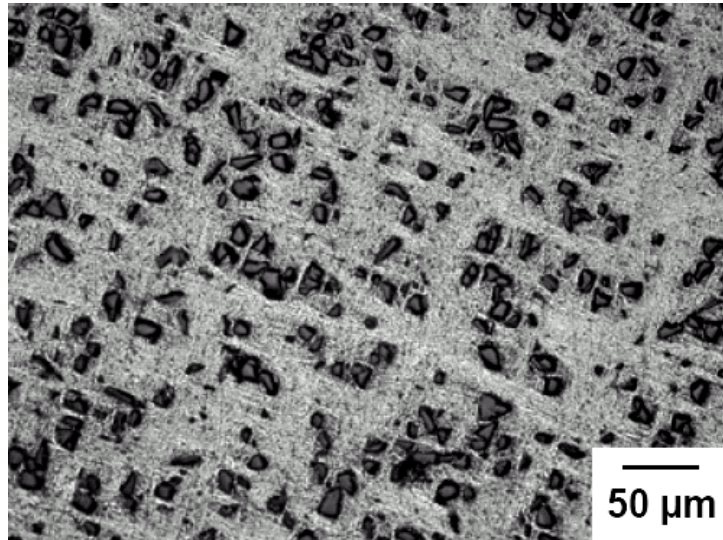
## CHAPTER 4

### RESULTS

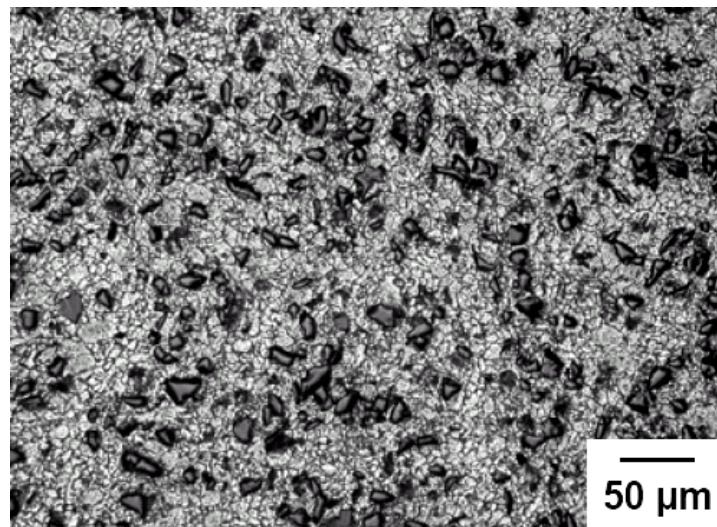
#### 4.1. Microstructures

The microstructure of the composites, in both as-polished and etched condition, are given in Figs. 4.1 to 4.4. The dark, angular particles in the micrographs are boron carbide. The matrix phase in light contrast is the Al - 4 wt.% Cu matrix alloy. All the composites showed some particle segregation. This was mainly due to the varying sizes of the chosen powders, and not due to improper mixing.

After hot pressing at 585°C, proper densification could not be achieved in the higher volume fraction 30 vol.% and 40 vol.% B<sub>4</sub>C samples. For example, the pressing of the 40 vol.% composite at 585°C yielded a completely porous, sponge-like structure. The hot pressing temperature was therefore increased for the higher volume fraction composites, up to 600°C (Table 3.1). Experiments also showed that increasing the temperature beyond 600°C produced excessive liquid which tended to escape through the clearances between the punch and the die.

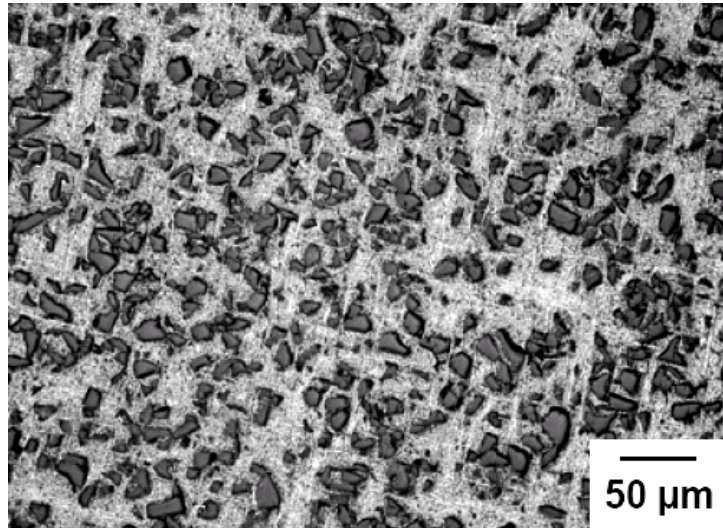


(a)

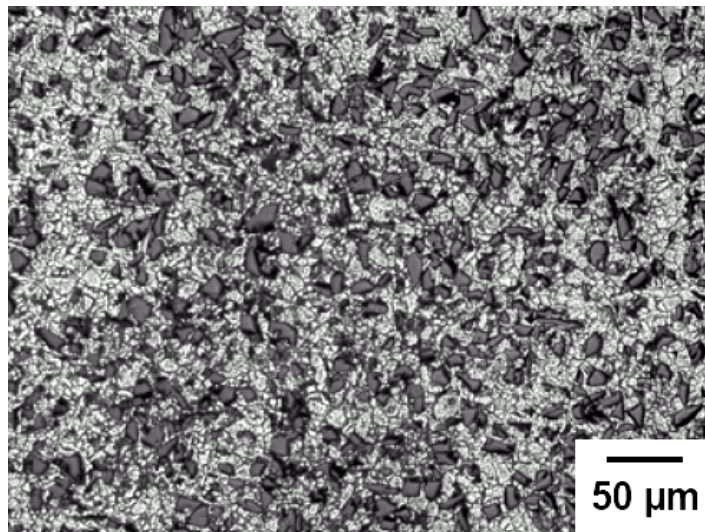


(b)

Fig. 4.1. The as-polished (a) and etched (b) microstructure of the 10 vol.% B<sub>4</sub>C composite.

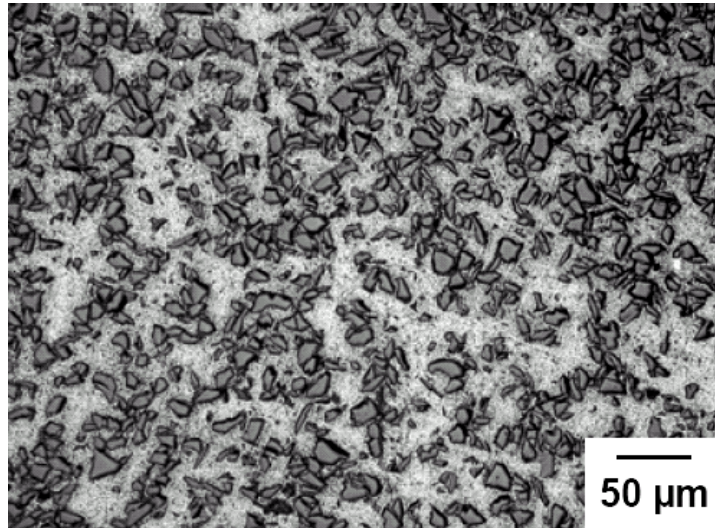


(a)

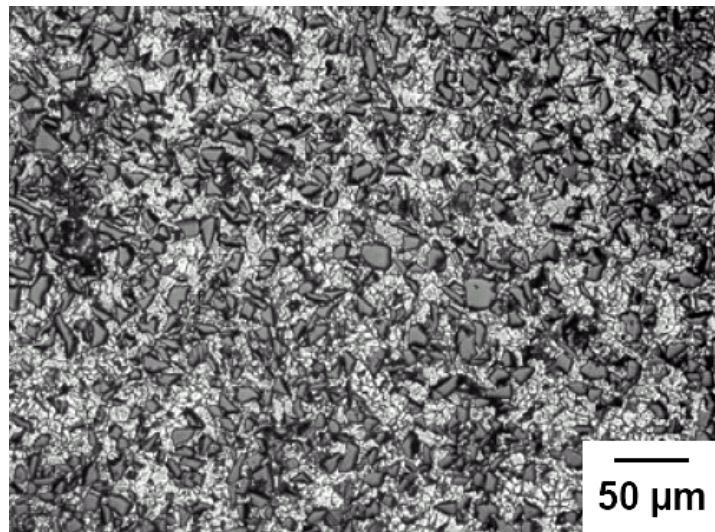


(b)

Fig. 4.2. The as-polished (a) and etched (b) microstructure of the 20 vol.%  $B_4C$  composite.

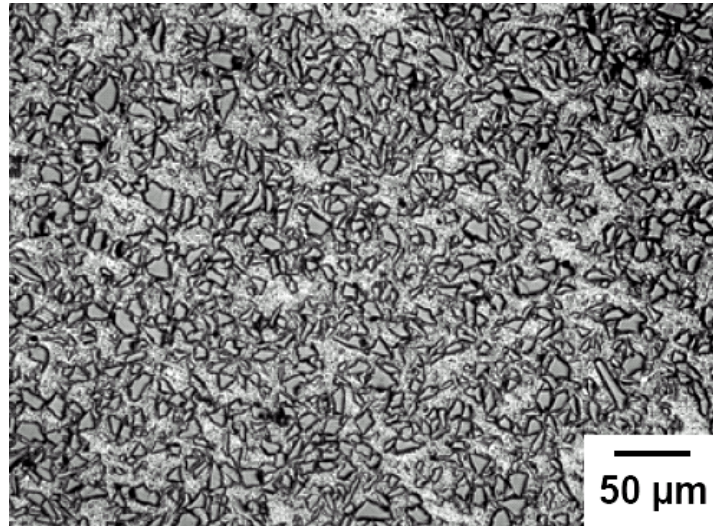


(a)

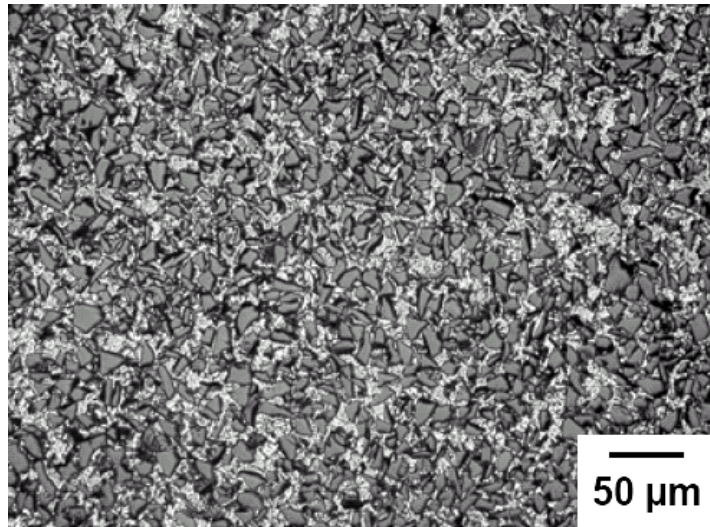


(b)

Fig. 4.3. The as-polished (a) and etched (b) microstructure of the 30 vol.% B<sub>4</sub>C composite.



(a)



(b)

Fig. 4.4. The as-polished (a) and etched (b) microstructure of the 40 vol.% B<sub>4</sub>C composite.

## 4.2. Aging Studies

The change in hardness of the Al - 4 wt.% Cu matrix alloy and its composites after aging at temperatures of 100°C, 125°C, 150°C, and 175°C are given in Figs. 4.5 to 4.8. The addition of B<sub>4</sub>C, as would be expected, increased the overall hardness values. The error bars in the hardness plots pointed out that there was a considerable scatter in hardness values. Particle clustering and local differences in particle size were most probably responsible for such variations in hardness.

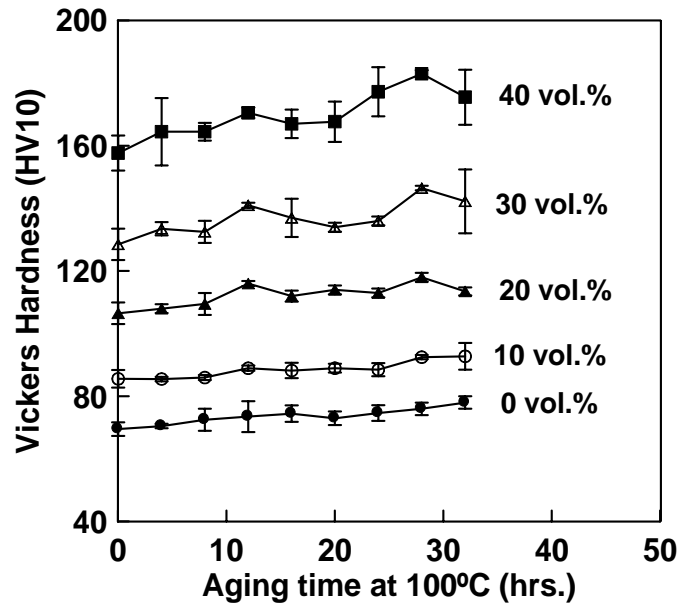


Fig. 4.5. The variation of hardness as a function of aging time at 100°C for the matrix alloy (0 vol.%) and composites.

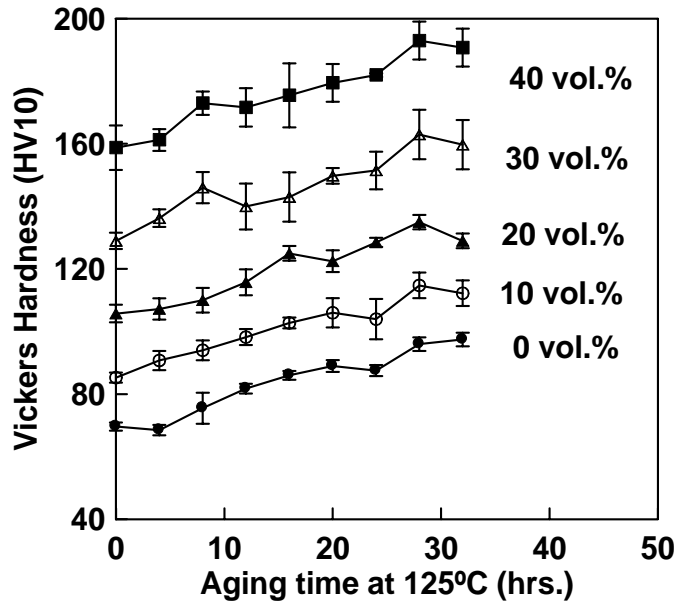


Fig. 4.6. The variation of hardness as a function of aging time at 125°C for the matrix alloy (0 vol.%) and composites.

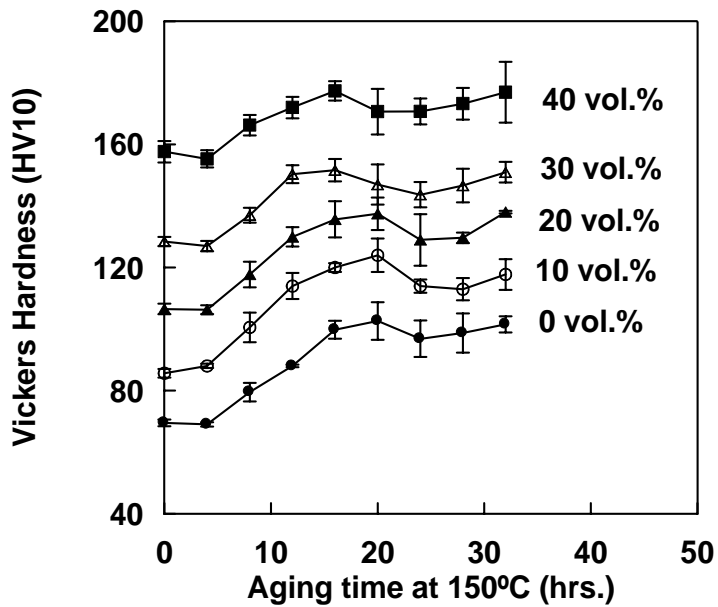


Fig. 4.7. The variation of hardness as a function of aging time at 150°C for the matrix alloy (0 vol.%) and composites.



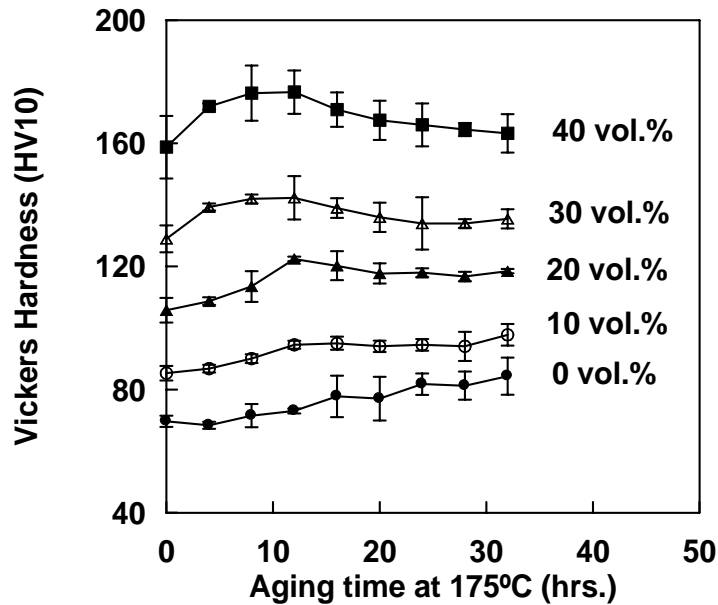


Fig. 4.8. The variation of hardness as a function of aging time at 175°C for the matrix alloy (0 vol.%) and composites.

The age hardening response of the composites and the matrix alloy were similar at aging temperatures of 100 or 125°C (Figs. 4.5 to 4.8); a steady increase in hardness with aging time was observed. At these temperatures the time to reach peak hardness was approximately the same for all samples. At an aging temperature of 100°C, the increase in hardness with aging time was very low, especially in the lower volume fraction composites and the matrix alloy. The hardness of the matrix alloy increased from 70 HV in the unaged condition to a maximum of 78 HV after aging at 100°C for 32 hours. The hardness of the 10 vol.% B<sub>4</sub>C composite increased from 86 HV in the unaged condition to a maximum of 93 HV after the same treatment.

At the beginning of the 100°C aging test, the hardness of the unaged 40 vol.% B<sub>4</sub>C composite was 158 HV; which was approximately twice the hardness of the unreinforced alloy in the same condition. Its hardness increased to 176 HV at the end of the 100°C, 32 hour aging test, shown in Fig. 4.5.

At 125°C, the samples showed increased dependence of hardness with aging time. The hardness of the matrix alloy increased from 70 HV in the unaged condition to a maximum of 98 HV after aging at 100°C for 28 hours. The hardness of the matrix alloy increased from 159 HV in the unaged condition to a maximum of 193 HV after aging at 100°C for 28 hours. Most of the highest hardness values were obtained at this aging temperature, and therefore a heat treatment of 125°C and 28 hours was chosen as the standard heat treatment for the transverse rupture tests.

At 150°C, a transition in the aging curves was observed (Fig. 4.7). The composites containing higher volume fractions of reinforcement were peak hardened more rapidly than their lower volume fraction counterparts. This accelerated aging effect was also observed at 175°C (Fig. 4.8). At this temperature, the peak hardening time for the 40 vol.% composite was only 8 hours. It was clear that above 150°C, accelerated aging dominated over the aging behavior of the composites. At the lower aging temperatures, higher peak hardness values were usually observed. This was believed to be due to the more homogeneous nucleation of precipitates.

The decrease in peak aging time due to increasing volume fraction of B<sub>4</sub>C at the aging temperature of 150°C was not significant. For example, when aged at 150°C (Fig. 4.7), the 40 vol.% B<sub>4</sub>C composite reaches peak hardness in 16 hours while the matrix alloy (0 vol.%) reaches peak hardness at 20 hours. The peak hardening times for the 10 vol.%, 20 vol.%, and 30 vol.% composites all lie between these values.

At 175°C (Fig. 4.8), the accelerated aging effect appears to be more distinct, with the 40 vol.% B<sub>4</sub>C composite reaching peak hardness at 8 hours, and the matrix alloy (0 vol.%) alloy showing a steady increase hardness over the entire

aging time of 32 hours. There was however considerable scatter in the hardness values of the matrix alloy after aging for 16 hours, which means that peak hardness may have been reached at any point beyond 16 hours.

### 4.3. Differential Scanning Calorimetry

The DSC thermograms of the as-quenched samples, taken at a heating rate of 40°C/min, are shown in Fig. 4.9. Two exothermic DSC peaks can be seen in each of the traces, and can most probably be attributed to  $\theta'$  and  $\theta$  formation. The intensity of the peaks were very faint but discernable. Increasing the heating rate to 100°C/min to separate the peaks did not give satisfactory results and are therefore not presented here.

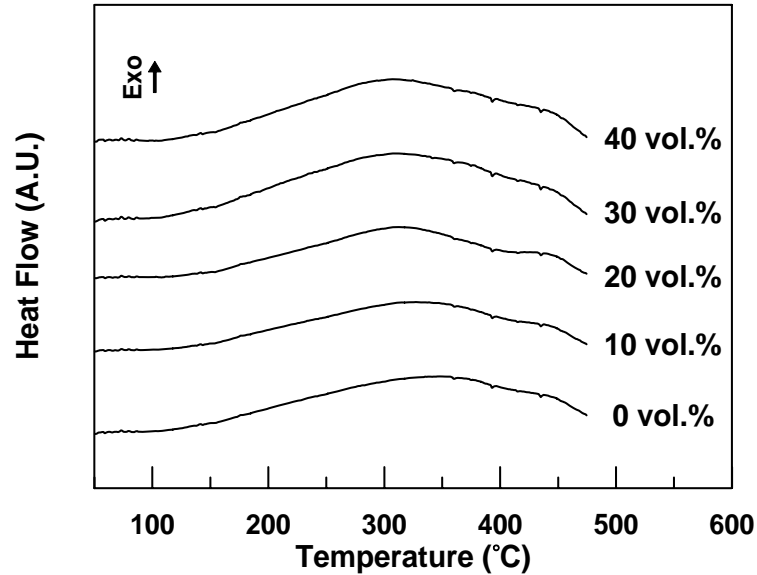


Fig. 4.9. DSC traces of the solutionized Al - 4 wt.% Cu matrix alloy and its composites

The first exothermic peak, occurring in a temperature range between 300 and 350°C, is believed to occur due to  $\theta'$  precipitation [57]. The temperature for the first exothermic peaks shifts to lower temperatures as the reinforcement volume fraction is increased. The second exothermic peak centered at about 425°C is ascribed to  $\theta$  precipitation [64], and does not seem to be affected by volume fraction of reinforcement.

#### 4.4. Transmission Electron Microscopy

Samples of the matrix alloy and the composite reinforced with 10 vol.% B<sub>4</sub>C particles were chosen for TEM studies. Although the 40 vol.% sample was also chosen, it could not be suitably prepared in the ion mill for the TEM observations. Two different aging treatments were applied: aging at 125°C for 28 hrs. and aging at 175°C for 8 hrs. The aging treatment at 125°C for 28 hrs. corresponded to the peak aging treatment. On the other hand, the aging treatment at 175°C for 8 hrs. corresponded to the peak aging treatment for the 40 vol.% composite, as seen in Fig. 4.8.

**i. Samples aged at 125°C for 28 hrs:** The bright field image of the matrix alloy in Fig. 4.10 shows fairly large  $\theta'$  precipitates (the grey, elliptic particles) compared to the composite in Fig. 4.11. The dark field image of the 10 vol.% B<sub>4</sub>C sample (Fig. 4.11) shows the precipitates existing in three different orientations. This image was taken by selecting a diffraction spot of one of the precipitates; therefore one of the three orientations of the precipitates appears white while the remaining two orientations appear dark.

Some defects were occasionally observed at the particle-matrix interface, but could not be clearly identified; EDS analyses of these regions did not show any significant change in composition. A selected area diffraction pattern (SADP)

indicated the presence of  $\theta'$  precipitates (Fig. 4.12) in both specimens. Considerable variation in size of the precipitates can be observed in both samples. Diffraction patterns indicated the presence of  $\theta''$  as well, especially in the reinforced composite. Precipitate size measurements from bright field and dark field images also confirmed the existence of both precipitate types.

**ii. Samples aged at 175°C for 8 hrs:** A bright field image of the matrix alloy and the 10 vol.% B<sub>4</sub>C composite is shown in Figs. 4.13 and 4.14, respectively. The precipitates were apparently much smaller at this aging treatment. Precipitation was enhanced in the composite, which showed a higher volume fraction of precipitates, which is a sign of higher nucleation rate. The precipitates in the composite were also slightly larger in size, with respect to the unreinforced alloy.

SADP and precipitate size measurements of both samples revealed the presence of  $\theta''$  precipitates (Fig. 4.15) and to a lesser extent, GP zones. Several undissolved  $\theta$  phase were also observed in all of the TEM samples, which were mostly found at the grain boundaries, as seen in Fig. 4.16.

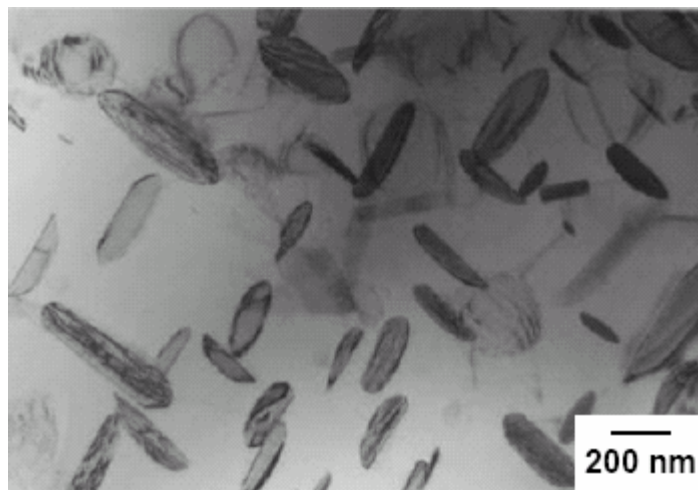


Fig. 4.10. Bright field image of the Al - 4 wt.%Cu alloy aged at 125°C for 28 hrs.

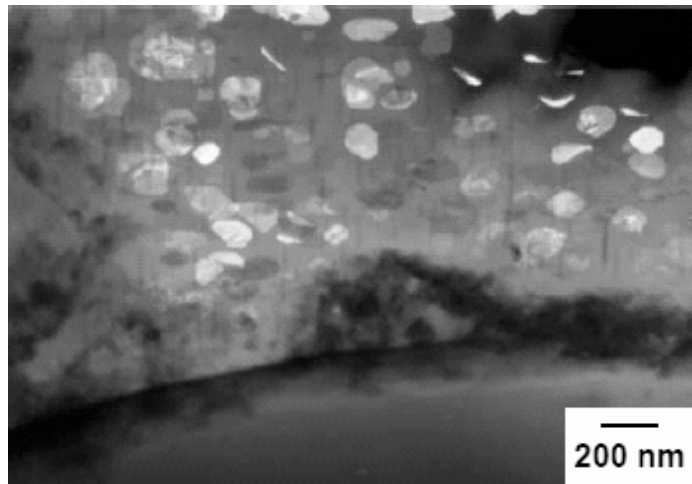


Fig. 4.11. Dark field image of the particle-matrix boundary in the 10 vol.%  $B_4C$  composite, aged at  $125^\circ C$  for 28 hrs.



Fig. 4.12. SADP of the Al - 4 wt.% Cu alloy aged at  $125^\circ C$  for 28 hrs.

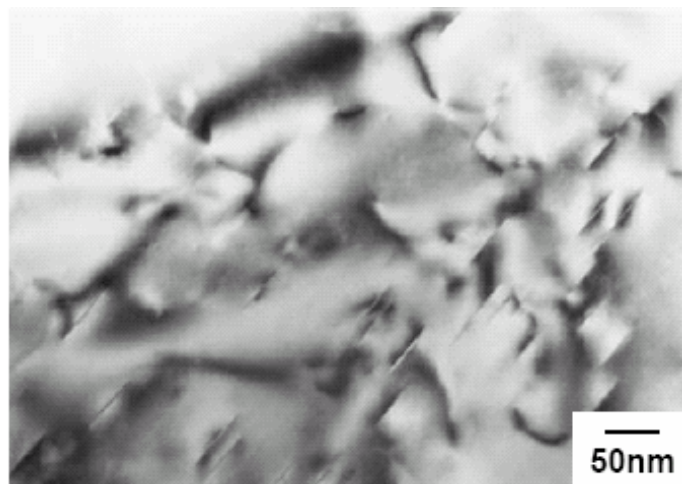


Fig. 4.13. Bright field image of the Al - 4 wt.%Cu alloy aged at  $175^\circ C$  for 8 hrs.



Fig. 4.14. Bright field image of the 10 vol.% B<sub>4</sub>C composite aged at 175°C for 8 hrs.

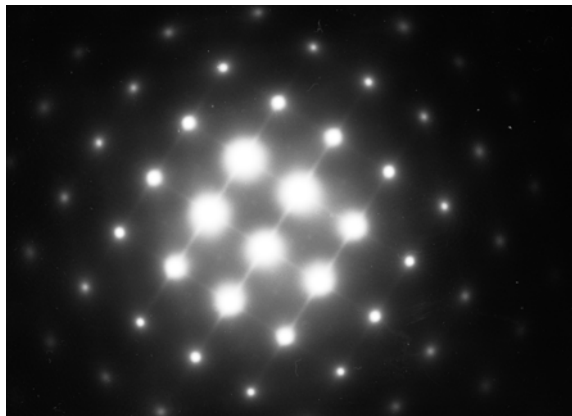


Fig. 4.15. SADP of the 10 vol.% B<sub>4</sub>C composite aged at 175°C for 8 hrs.

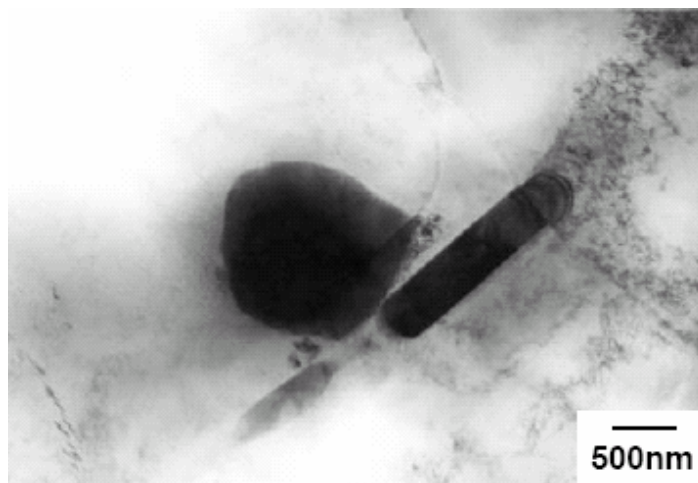


Fig. 4.16. Undissolved  $\theta$  particles in the 10 vol.% B<sub>4</sub>C composite aged at 175°C for 8 hrs.

### 4.3. Effects of Strain Rate

The flexural strengths of the samples were initially compared at a strain rate of  $5 \times 10^{-4} \text{ s}^{-1}$ , which corresponds to a rate of standard quasistatic tests. As shown in Fig. 4.17, both the as-fabricated and heat treated samples show decreasing flexural strength values with increasing volume fraction. A heat treatment operation caused a substantial increase in flexural strength of both the matrix alloy and its composites.

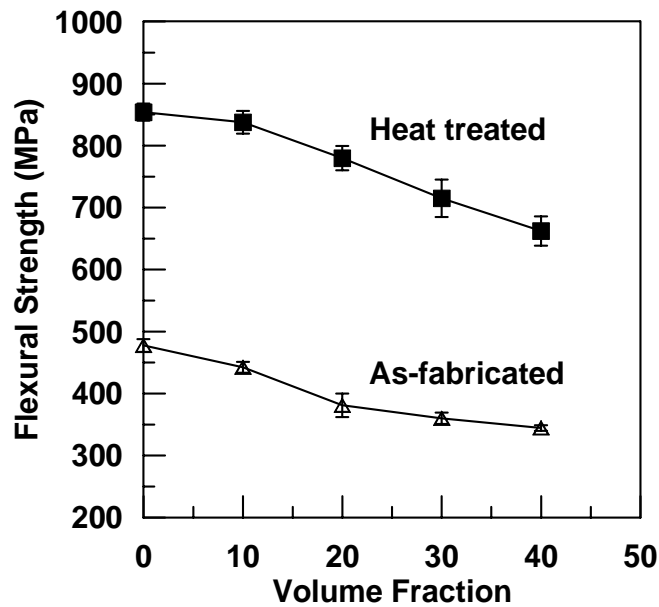


Fig. 4.17. The effect of volume fraction on the flexural strength for the as-fabricated and heat treated samples.

The flexural strength vs. strain rate curves for the specimens tested in the as-fabricated and heat-treated (125°C, 28 hrs.) condition are shown in Fig. 4.18 and Fig. 4.19, respectively. The flexural strength of all of the alloys, both the matrix alloy and the composites, first increased slightly with an increase in



strain rate, and then decreased at strain rates higher than  $10^{-2} \text{ s}^{-1}$ . For example, the strength of the matrix alloy was increased from about 477 MPa to 854 MPa at  $5 \times 10^{-4} \text{ s}^{-1}$  after an aging treatment at  $125^\circ\text{C}$ . Similar trends were also observed for the composites; the strength of the 10 vol.% composite was increased from an average of 442 MPa to 837 MPa at  $5 \times 10^{-4} \text{ s}^{-1}$  after the aging treatment. The strength of the 20 vol.% was also improved, with an increase from 381 MPa to 780 MPa at  $5 \times 10^{-4} \text{ s}^{-1}$  after aging. The improvement in strength for the heat treated 30 vol.% and 40 vol.% composites appeared to be less pronounced, which is most possibly due to the higher amount of potential defect sites.

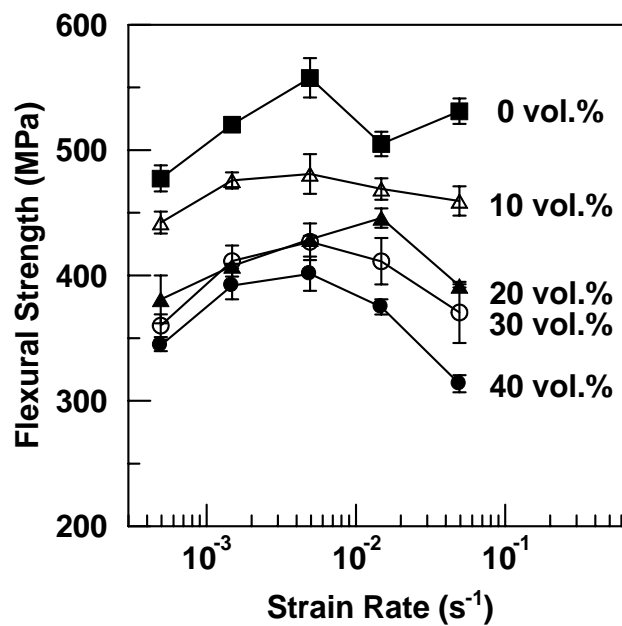


Fig. 4.18. The effect of strain rate on the flexural strength for the as-fabricated alloy and its composites.

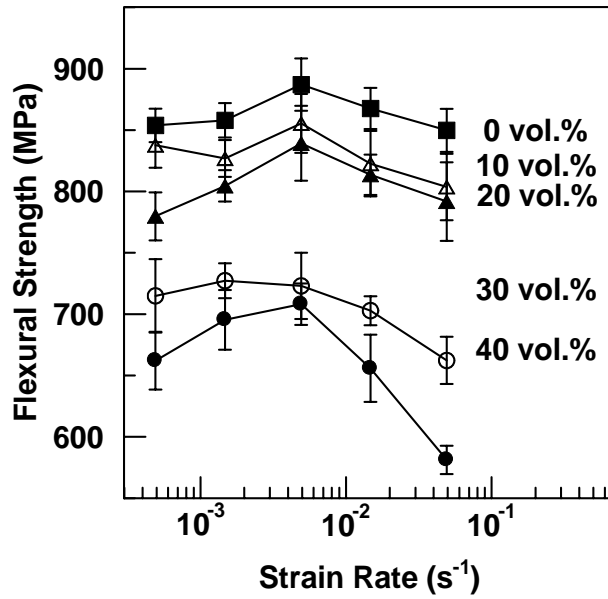


Fig. 4.19. The effect of strain rate on the flexural strength for the heat-treated alloy and its composites.

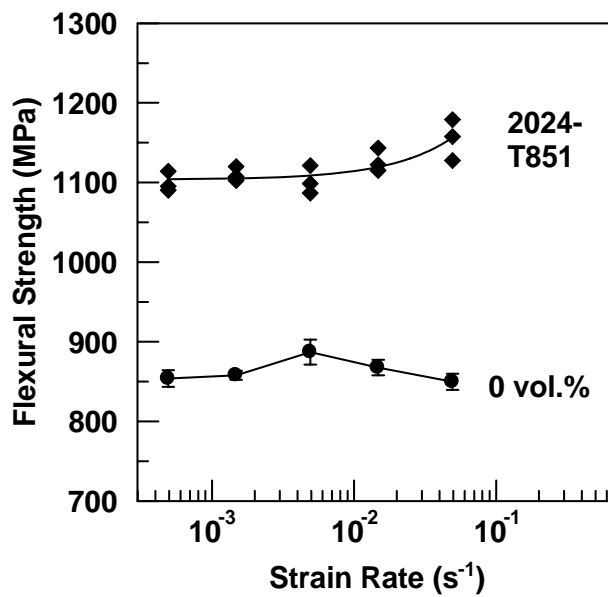


Fig. 4.20. The effect of strain rate on the flexural strength for the 2024-T851 aluminum alloy, compared with the heat treated matrix alloy.

Fig. 4.20 shows the flexural strength vs. strain rate curve for the 2024-T851 alloy which was tested in this study for comparison purposes. The results of the

heat treated matrix alloy are also shown in this figure. The wrought alloy showed considerably higher flexural strength values when compared to the P/M matrix alloy and the composites. This result was expected since the 2024-T851 is a wrought alloy and is modified with alloying additions such as magnesium, manganese and iron. The high strength of the 2024-T851 alloy is also due to its T851 temper, which means it has been solutionized, cold worked, stress-relieved, and artificially aged for optimum mechanical strength.

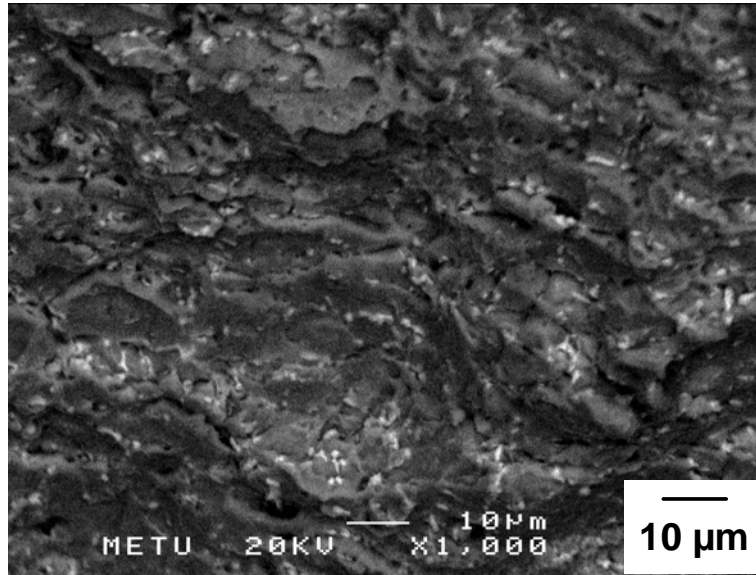
#### **4.5. Fractography**

Fracture surface examinations were made on the tensile regions of the fracture surfaces of the transverse rupture specimens tested at strain rates of  $5 \times 10^{-3}$  and  $5 \times 10^{-2} \text{ s}^{-1}$ : These two strain rates correspond to the two extremes in which the composites show high and low strength, respectively. Figures 4.21-4.30 show the backscattered electron images (BSE) of the fracture surfaces of the tested transverse rupture samples. The corresponding secondary electron images (SEI) are given in Figs. 4.31-4.40. The backscatter electron images indicate the presence of non-dissolved copper-rich phases, appearing in lighter contrast, in all of the as-fabricated samples. The grey areas belong to the aluminum alloy matrix, and the dark areas belong to the  $\text{B}_4\text{C}$  reinforcement. The occurrence of copper rich phases appear to be much less in the heat treated samples.

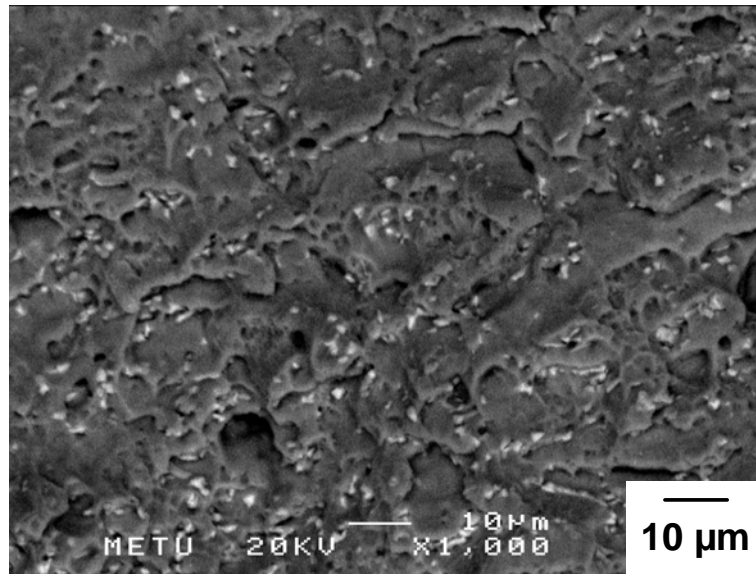
Evidence for the improvement in mechanical strength for the matrix alloy with heat treatment can be observed by comparing Figs. 4.31 and 4.32. The heat treated samples show deeper, more homogeneous and elongated dimples compared to that of the matrix alloy. Dimple fracture, involving void coalescence and growth, appears to be the fracture mechanism. Interface decohesion and particle cracking were additional mechanisms observed in the composites (compare Figs. 4.23(b) and 4.33(b)).

Ballistic testing was conducted on both the matrix alloy and its composites. A hot-pressed boron carbide ceramic armor was also tested for comparison purposes. The velocity test results, showing the change in residual velocity with volume fraction, are shown in Fig. 4.41, and photographs of the armors after ballistic testing are shown in Figs. 4.42-4.47.

With the exception of the pure  $B_4C$  ceramic armor, all of the tested armors were perforated. A considerable amount of bulging was detected on the backing plate of the  $B_4C$  ceramic armor (Fig. 4.47(b)), when compared to the MMC composite armors. Among all of the composite materials tested, the 20 vol.%  $B_4C$  composite was most effective in decreasing the velocity of the AP projectile. The 20 vol.%  $B_4C$  composite was also the composite with the highest volume fraction of reinforcement capable of stopping radial crack propagation (Fig. 4.44(a)), which is in good agreement with the velocity plots. Whereas deformation was localized to a small area in the MMC composite armors, a more widespread deformation was observed in the  $B_4C$  ceramic armor.

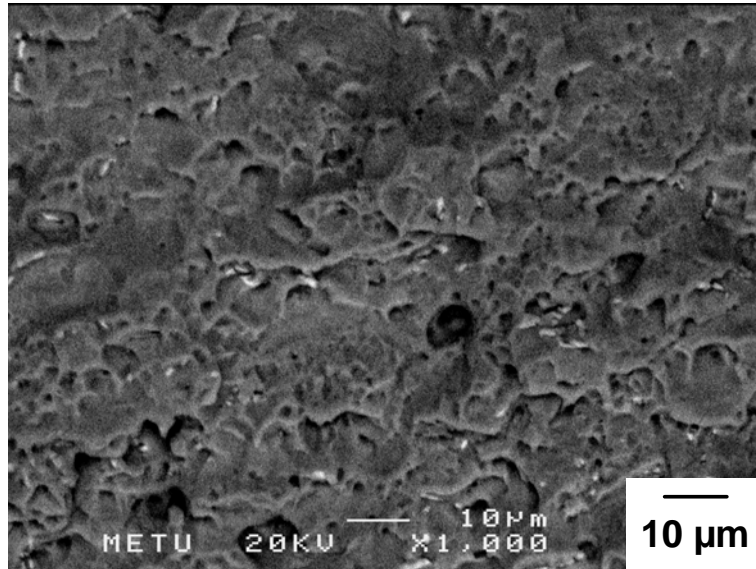


(a)

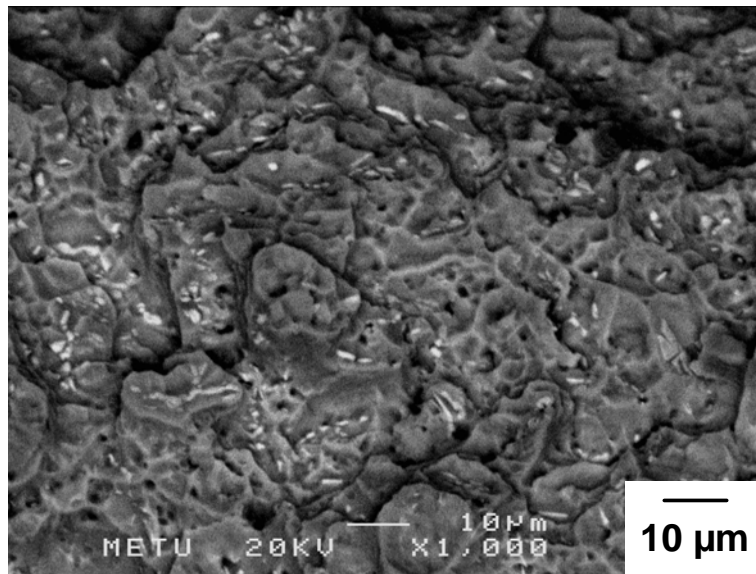


(b)

Fig. 4.21. BSE fractograph of the as fabricated Al - 4 wt.% Cu matrix alloy, tested at a strain rate of (a)  $5 \times 10^{-3}$  and (b)  $5 \times 10^{-2} \text{ s}^{-1}$ .

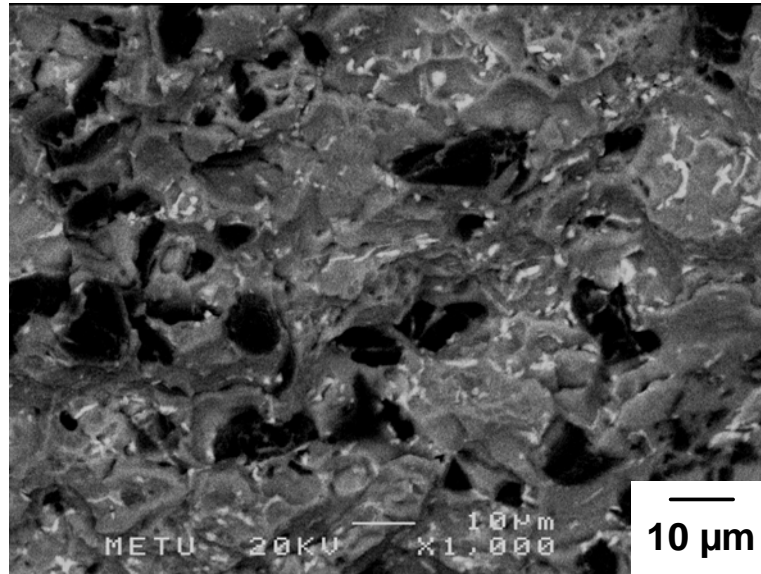


(a)

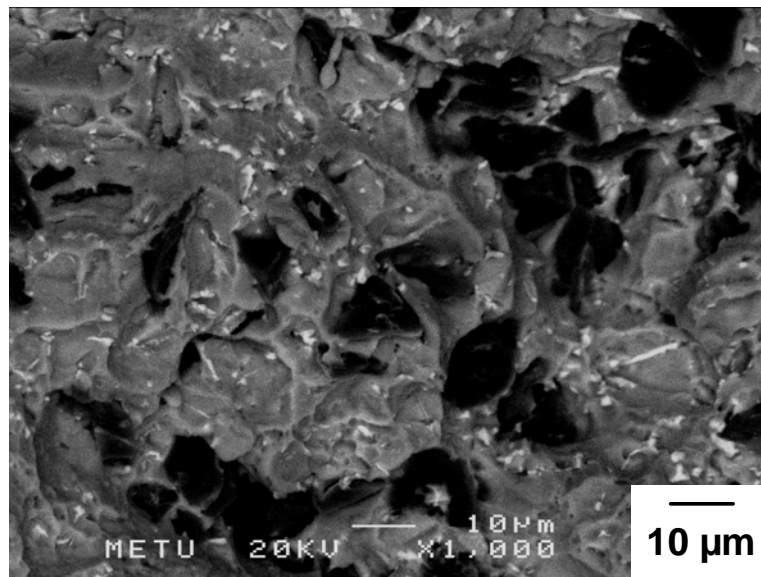


(b)

Fig. 4.22. BSE fractograph of the heat treated Al - 4 wt.% Cu alloy, tested at a strain rate of (a)  $5 \times 10^{-3}$  and (b)  $5 \times 10^{-2} \text{ s}^{-1}$ .

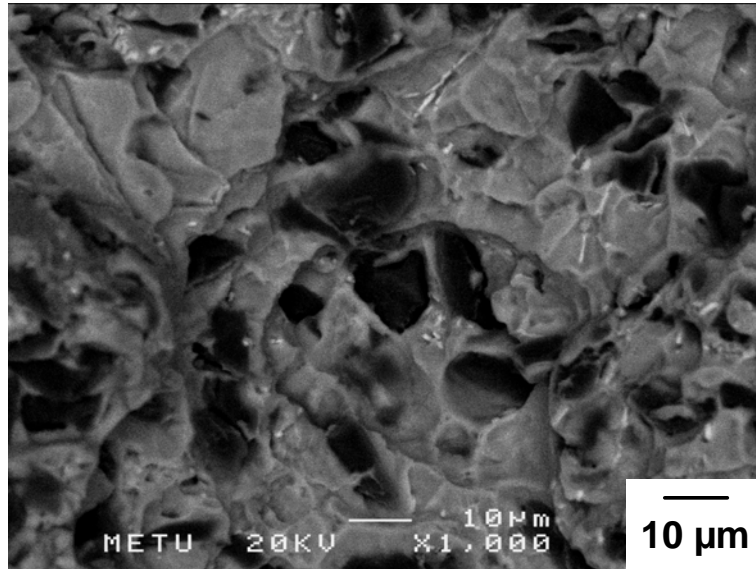


(a)

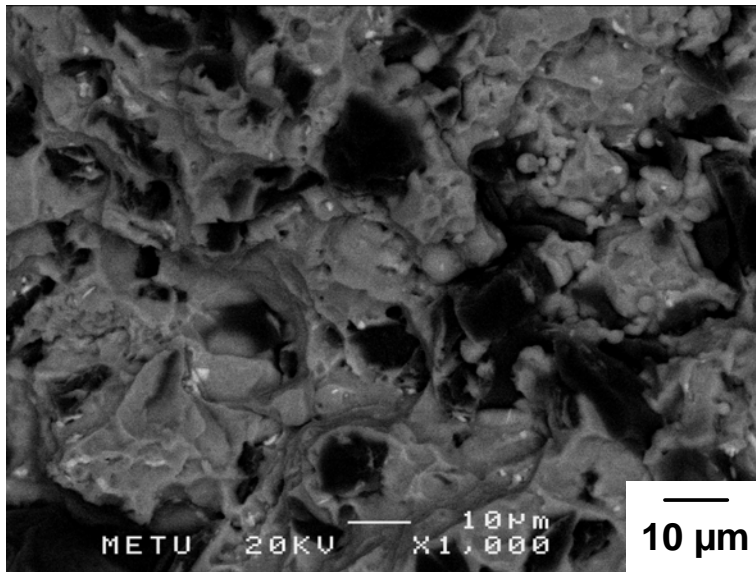


(b)

Fig. 4.23. BSE fractograph of the as fabricated 10 vol.% composite, tested at a strain rate of (a)  $5 \times 10^{-3}$  and (b)  $5 \times 10^{-2} \text{ s}^{-1}$ .



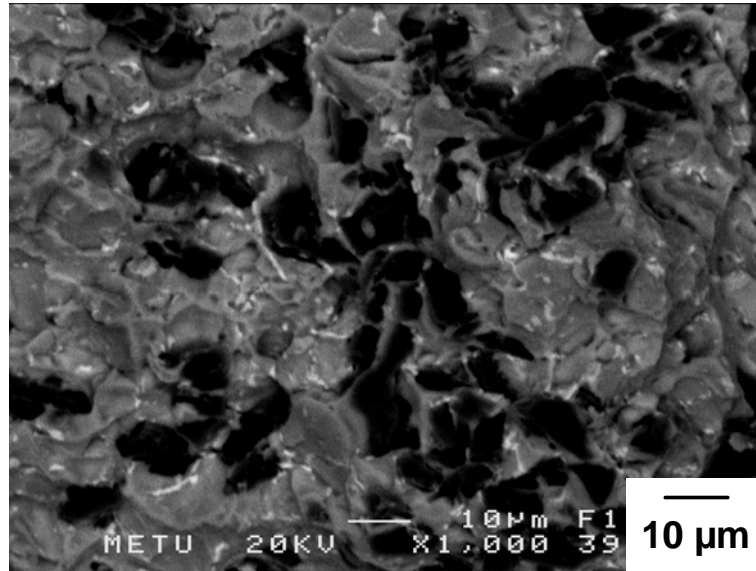
(a)



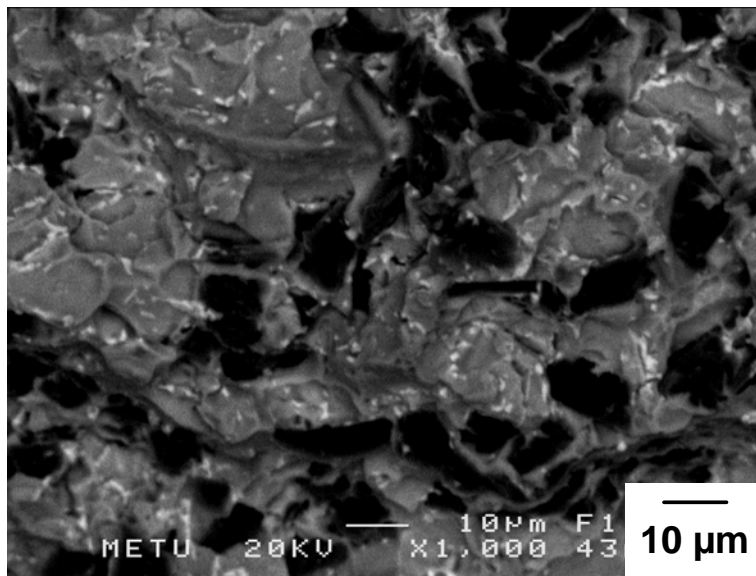
(b)

Fig. 4.24. BSE fractograph of the heat treated 10 vol.% composite, tested at a strain rate of (a)  $5 \times 10^{-3}$  and (b)  $5 \times 10^{-2} \text{ s}^{-1}$ .



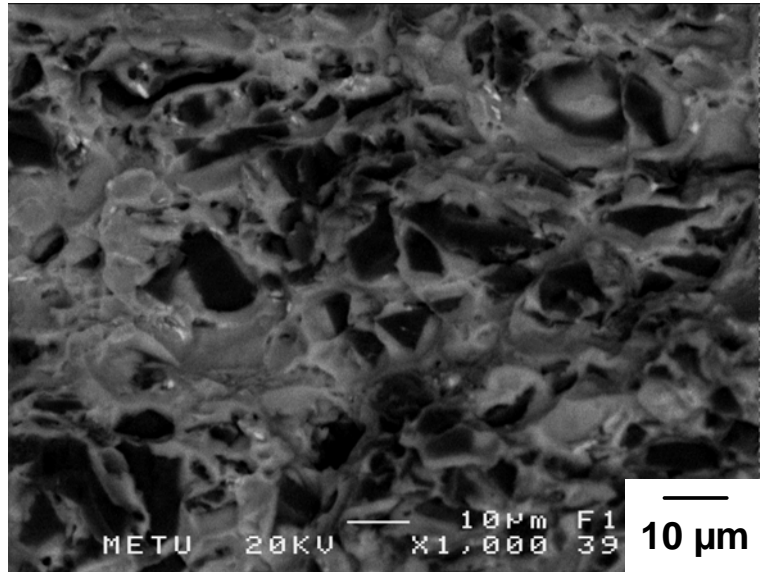


(a)

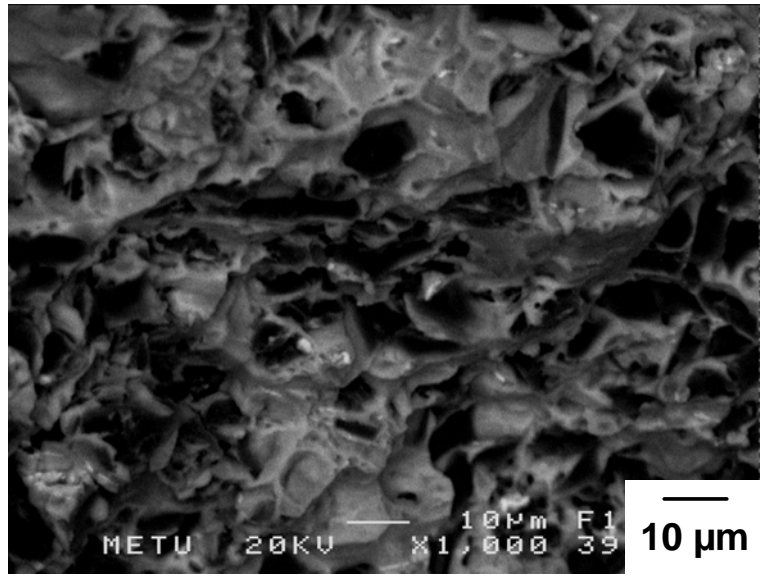


(b)

Fig. 4.25. BSE fractograph of the as fabricated 20 vol.% composite, tested at a strain rate of (a)  $5 \times 10^{-3}$  and (b)  $5 \times 10^{-2} \text{ s}^{-1}$ .

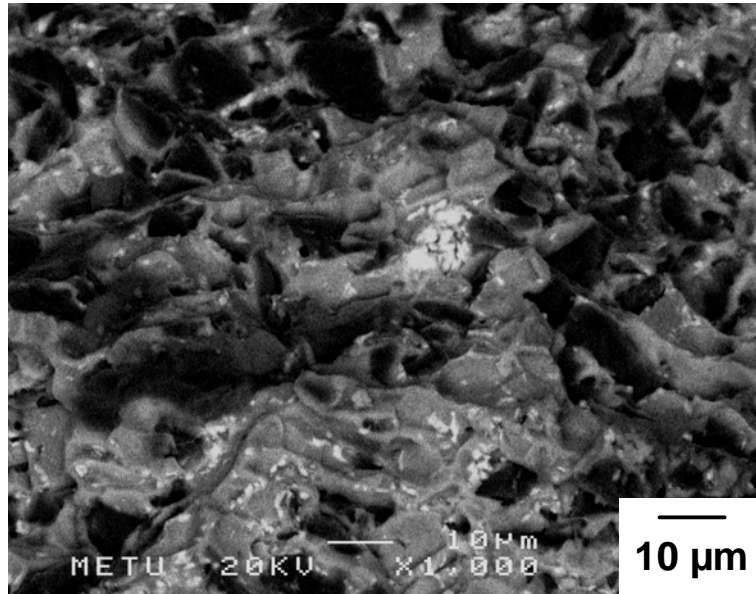


(a)

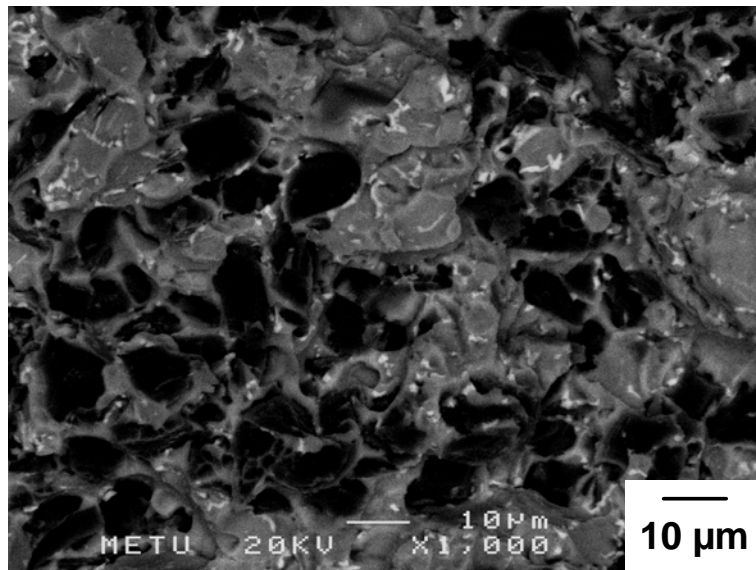


(b)

Fig. 4.26. BSE fractograph of the heat treated 20 vol.% composite, tested at a strain rate of (a)  $5 \times 10^{-3}$  and (b)  $5 \times 10^{-2} \text{ s}^{-1}$ .

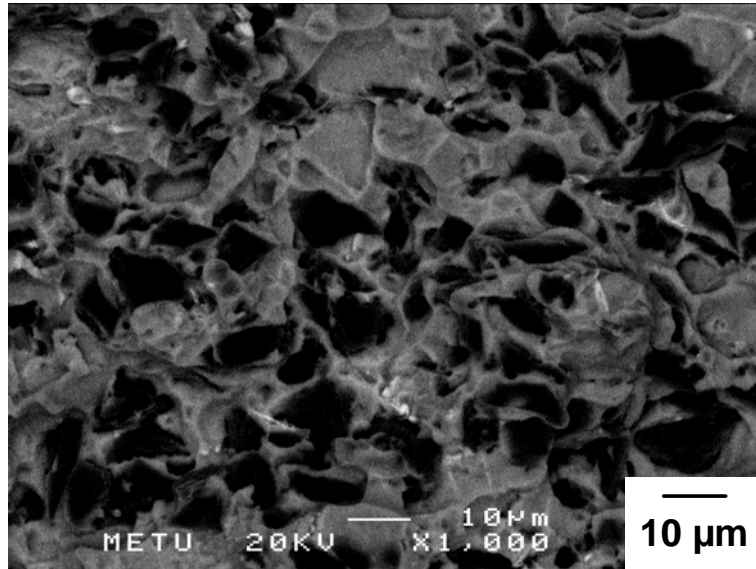


(a)

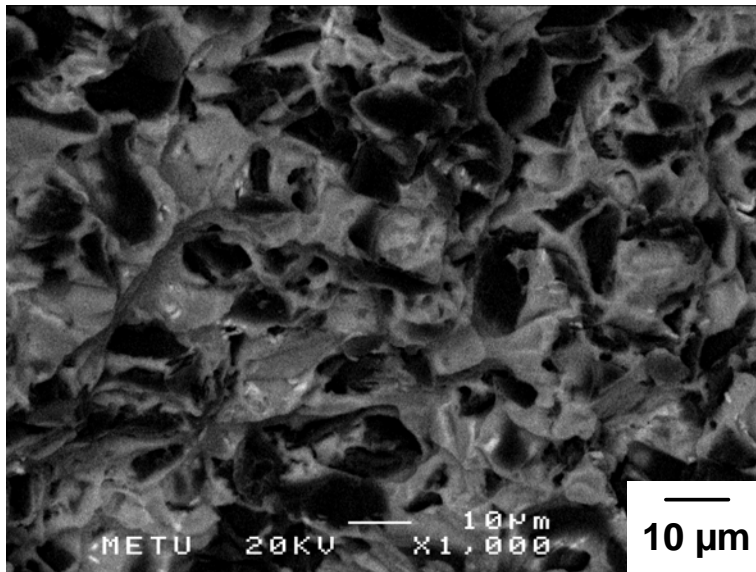


(b)

Fig. 4.27. BSE fractograph of the as fabricated 30 vol.% composite, tested at a strain rate of (a)  $5 \times 10^{-3}$  and (b)  $5 \times 10^{-2} \text{ s}^{-1}$ .

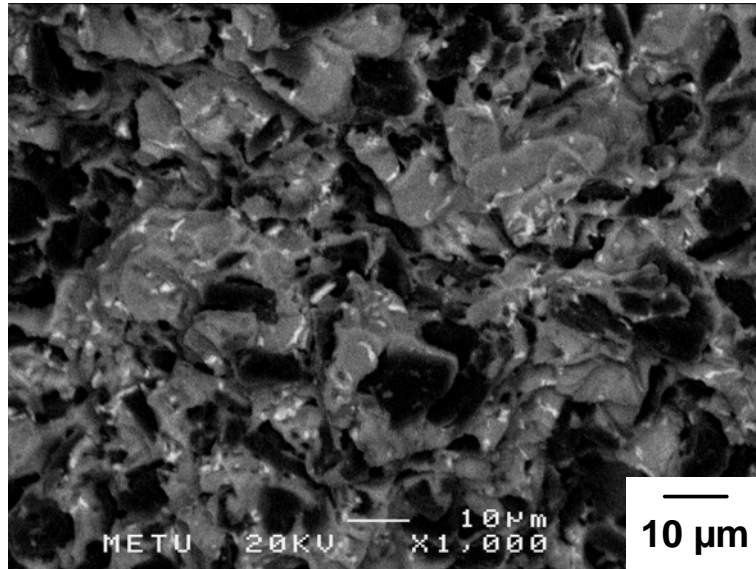


(a)

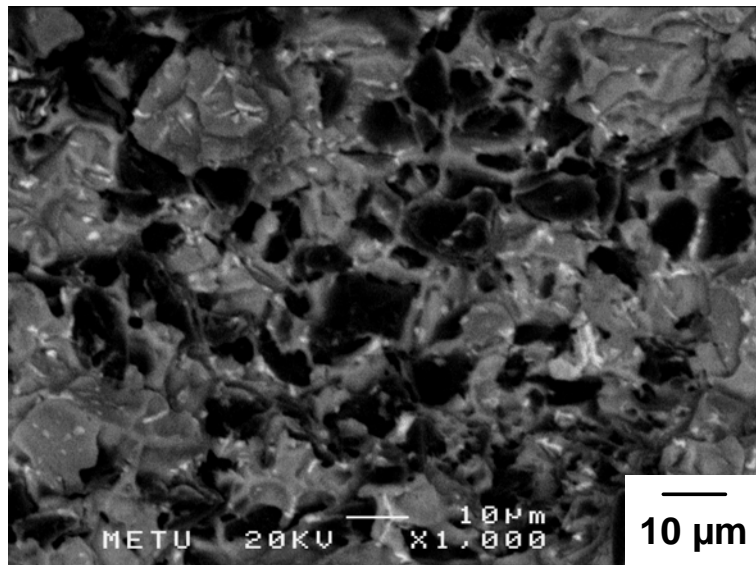


(b)

Fig. 4.28. BSE fractograph of the heat treated 30 vol.% composite, tested at a strain rate of (a)  $5 \times 10^{-3}$  and (b)  $5 \times 10^{-2} \text{ s}^{-1}$ .

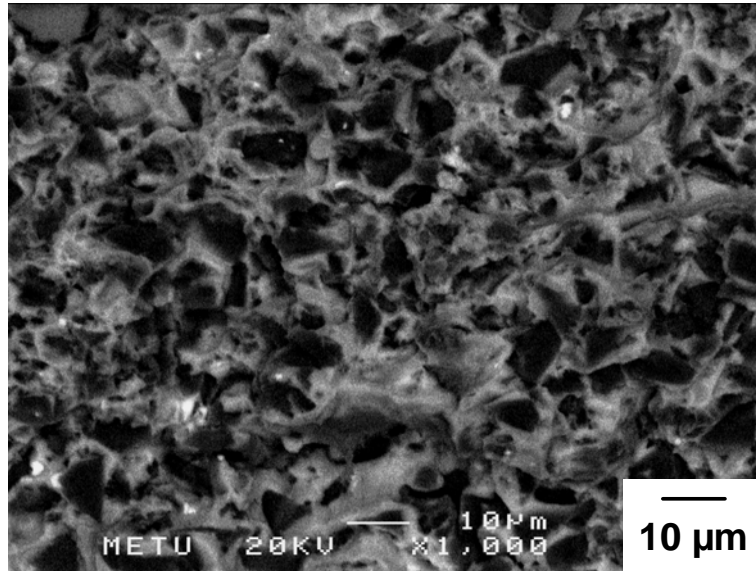


(a)

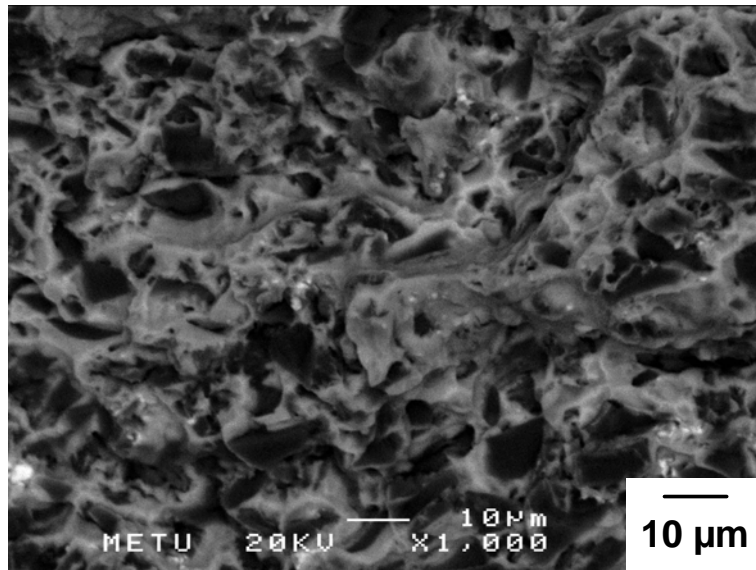


(b)

Fig. 4.29. BSE fractograph of the as fabricated 40 vol.% composite, tested at a strain rate of (a)  $5 \times 10^{-3}$  and (b)  $5 \times 10^{-2} \text{ s}^{-1}$ .

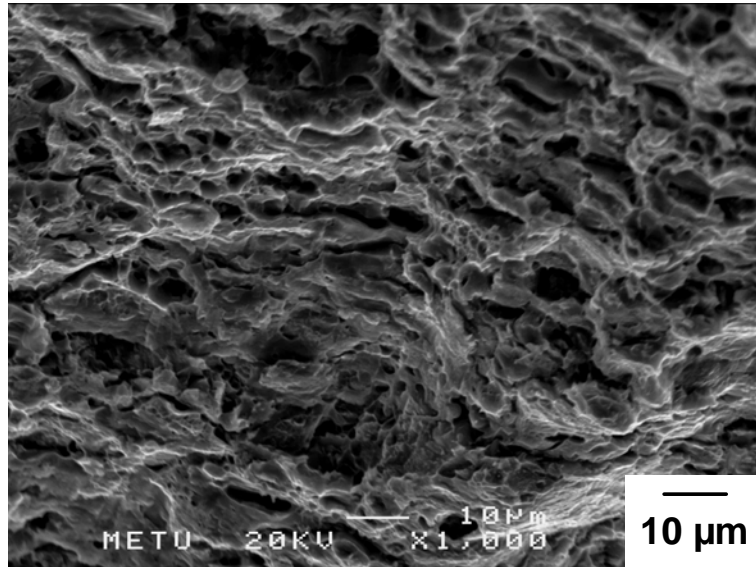


(a)

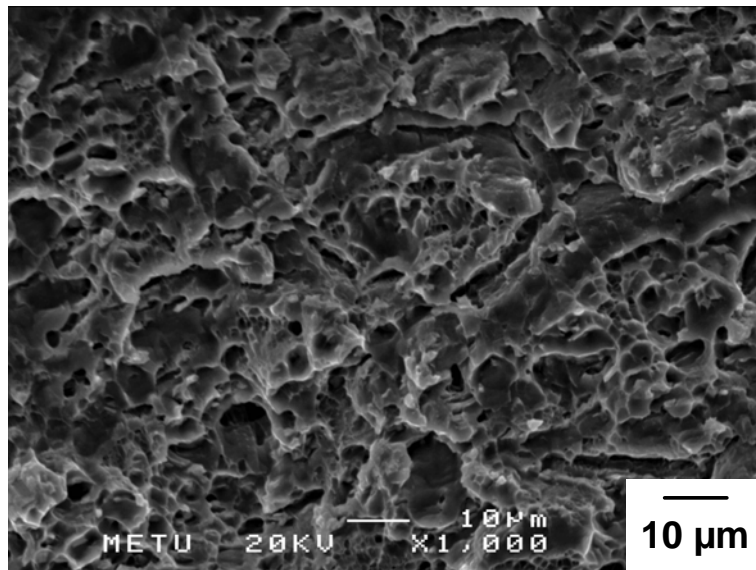


(b)

Fig. 4.30. BSE fractograph of the heat treated 40 vol.% composite, tested at a strain rate of (a)  $5 \times 10^{-3}$  and (b)  $5 \times 10^{-2} \text{ s}^{-1}$ .

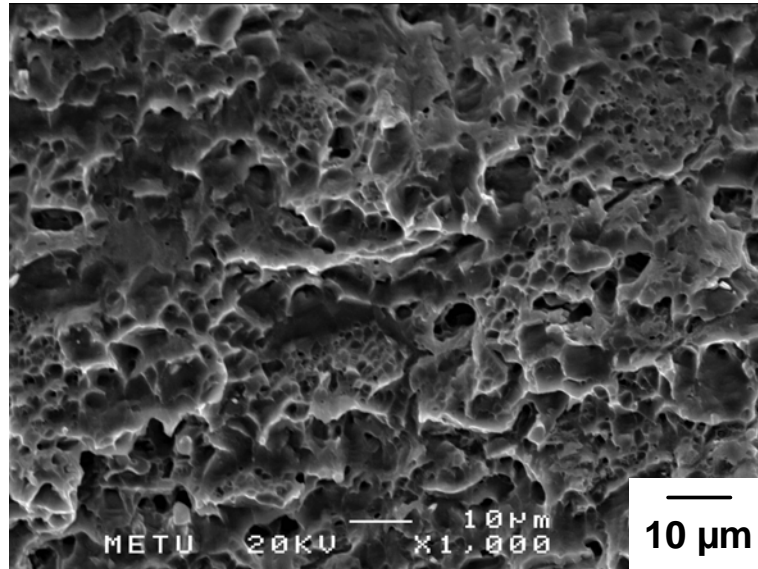


(a)

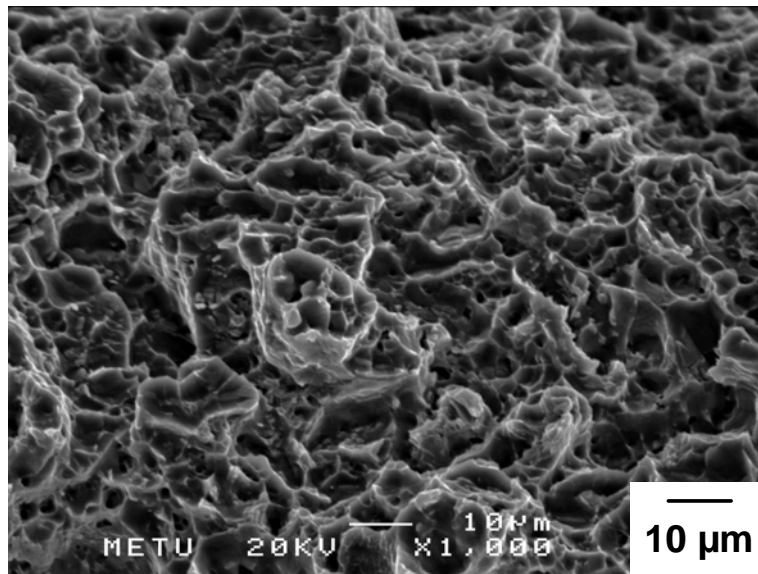


(b)

Fig. 4.31. SEI fractograph of the as fabricated Al-4 wt.% Cu matrix alloy, tested at a strain rate of (a)  $5 \times 10^{-3}$  and (b)  $5 \times 10^{-2} \text{ s}^{-1}$ .



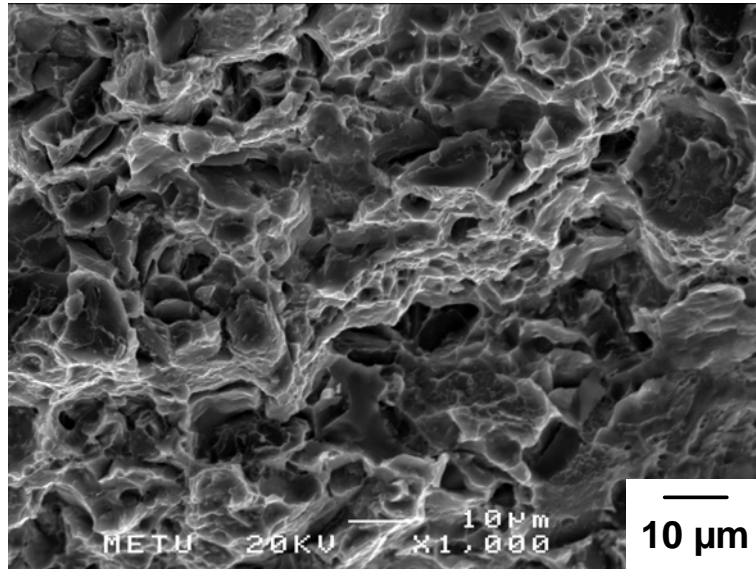
(a)



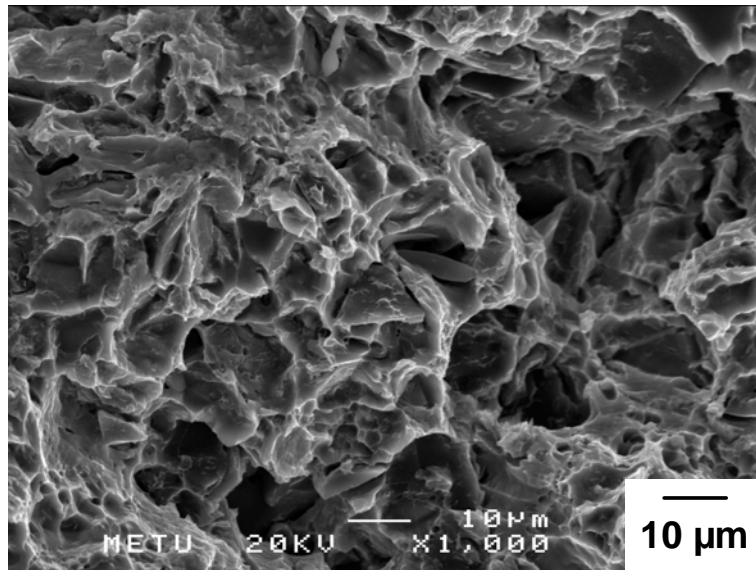
(b)

Fig. 4.32. SEI fractograph of the heat treated Al-4 wt.% Cu alloy, tested at a strain rate of (a)  $5 \times 10^{-3}$  and (b)  $5 \times 10^{-2} \text{ s}^{-1}$ .



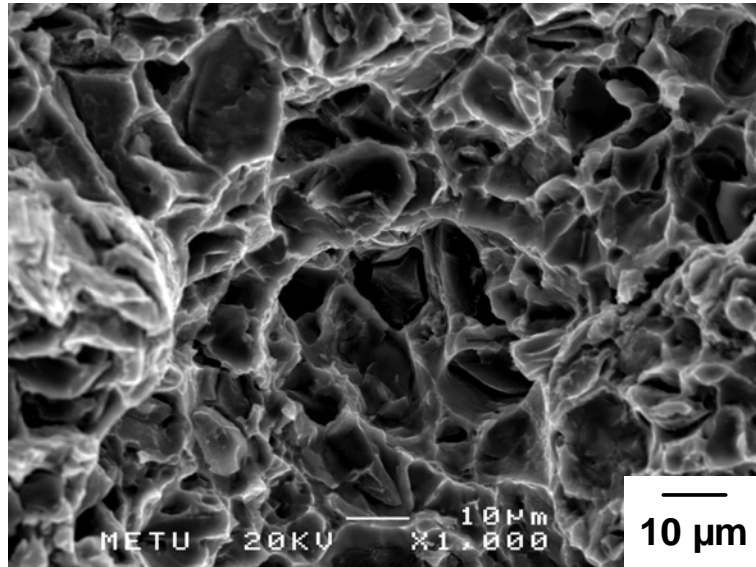


(a)

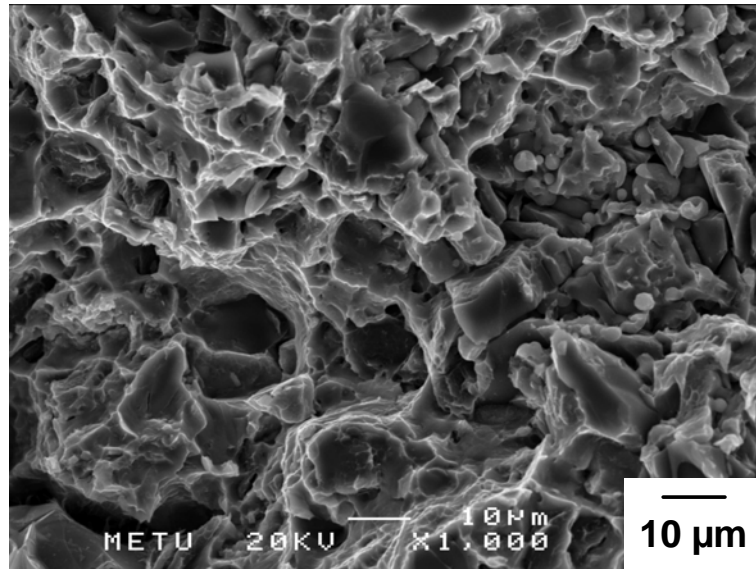


(b)

Fig. 4.33. SEI fractograph of the as-fabricated 10 vol.% composite, tested at a strain rate of (a)  $5 \times 10^{-3}$  and (b)  $5 \times 10^{-2} \text{ s}^{-1}$ .

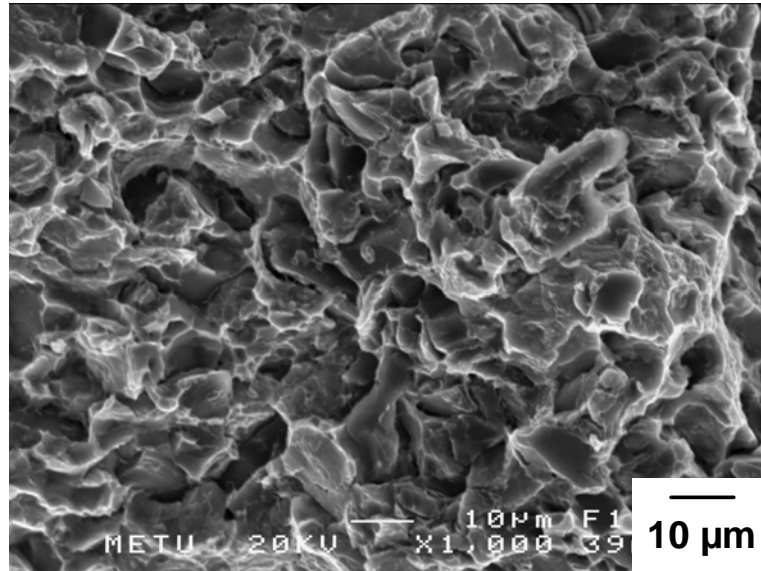


(a)

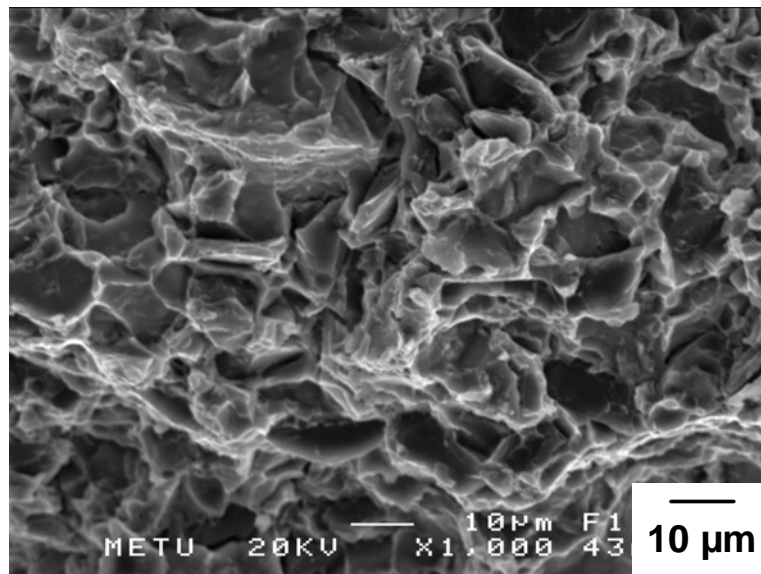


(b)

Fig. 4.34. SEI fractograph of the heat treated 10 vol.% composite, tested at a strain rate of (a)  $5 \times 10^{-3}$  and (b)  $5 \times 10^{-2} \text{ s}^{-1}$ .

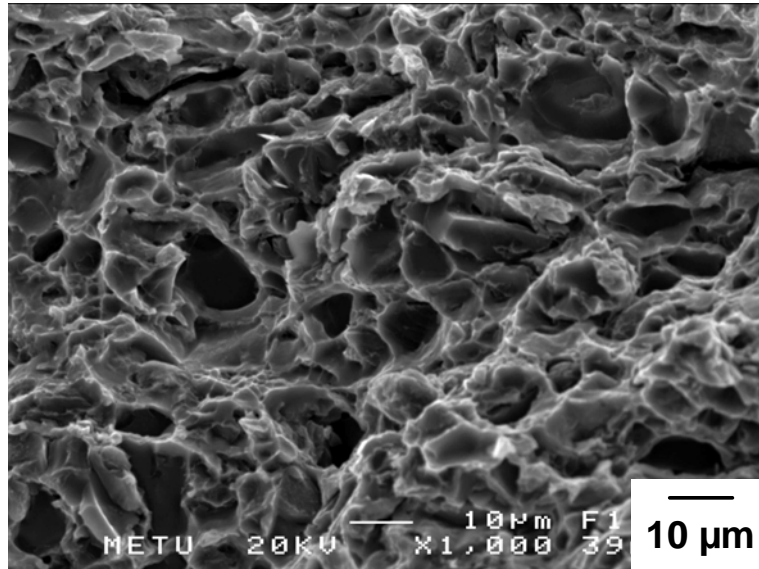


(a)

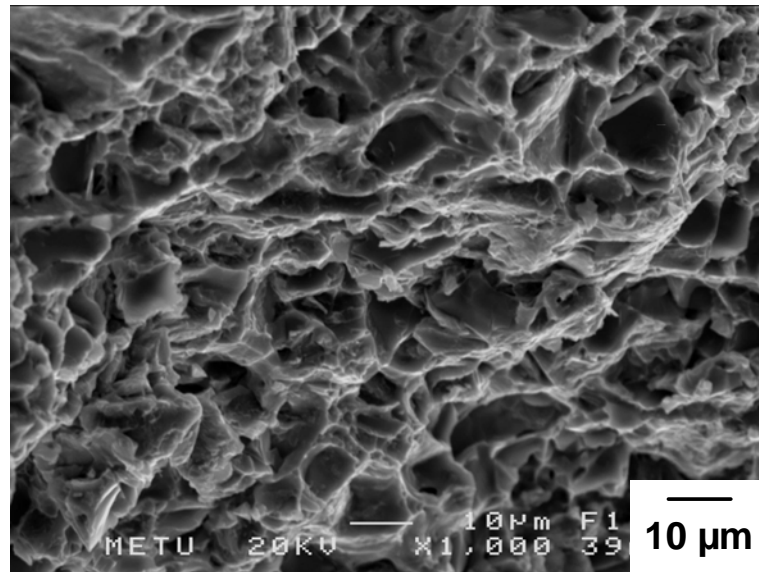


(b)

Fig. 4.35. SEI fractograph of the as-fabricated 20 vol.% composite, tested at a strain rate of (a)  $5 \times 10^{-3}$  and (b)  $5 \times 10^{-2} \text{ s}^{-1}$ .

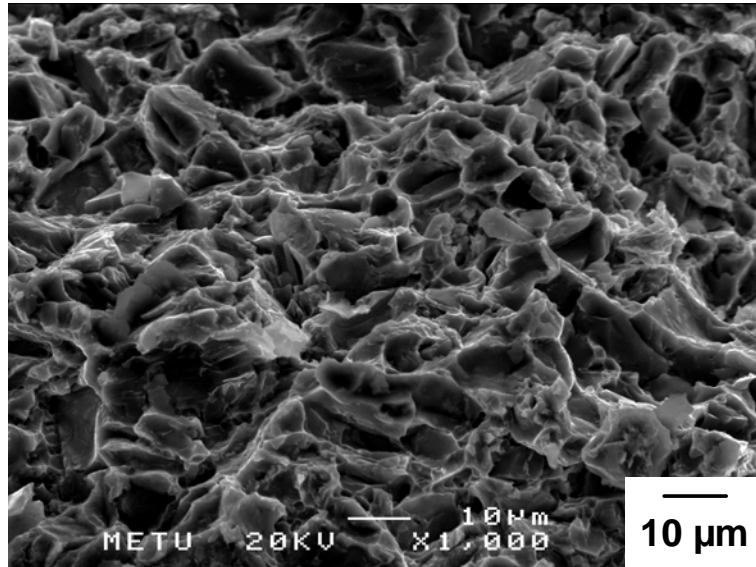


(a)

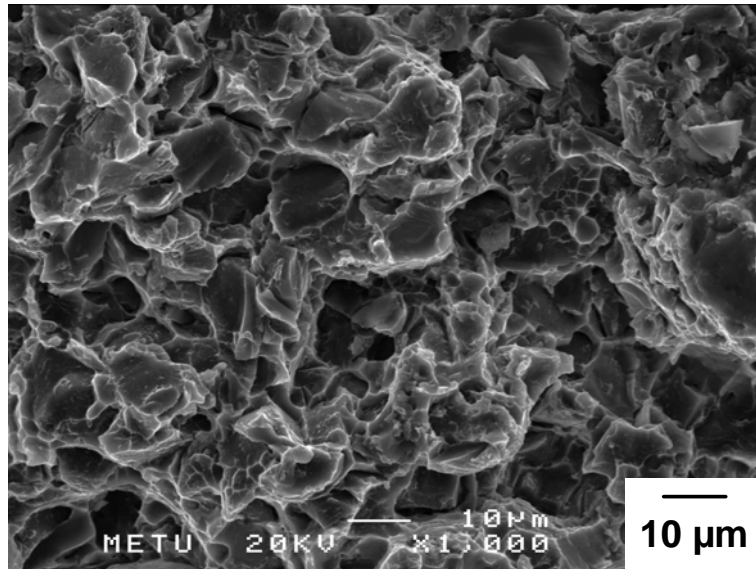


(b)

Fig. 4.36. SEI fractograph of the heat treated 20 vol.% composite, tested at a strain rate of (a)  $5 \times 10^{-3}$  and (b)  $5 \times 10^{-2} \text{ s}^{-1}$ .

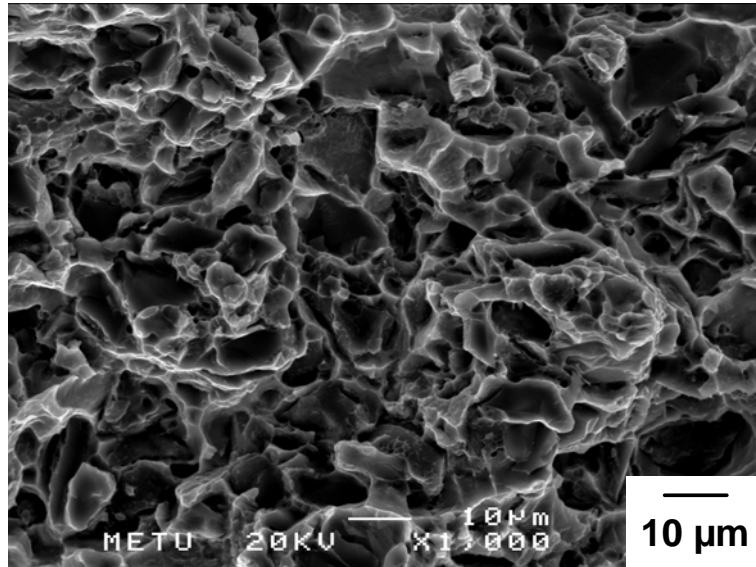


(a)

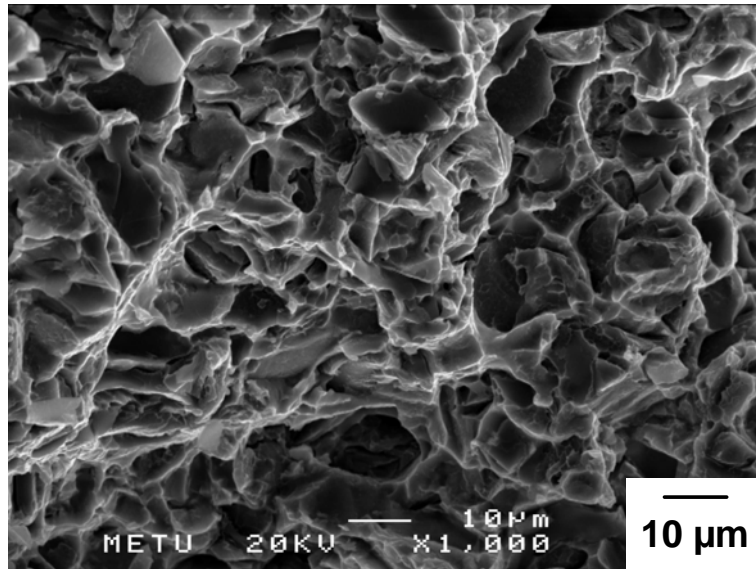


(b)

Fig. 4.37. SEI fractograph of the as fabricated 30 vol.% composite, tested at a strain rate of (a)  $5 \times 10^{-3}$  and (b)  $5 \times 10^{-2} \text{ s}^{-1}$ .

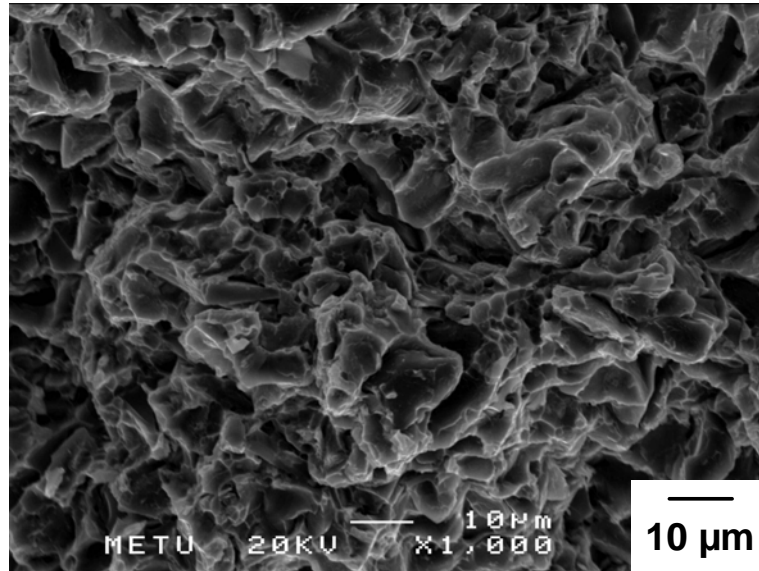


(a)

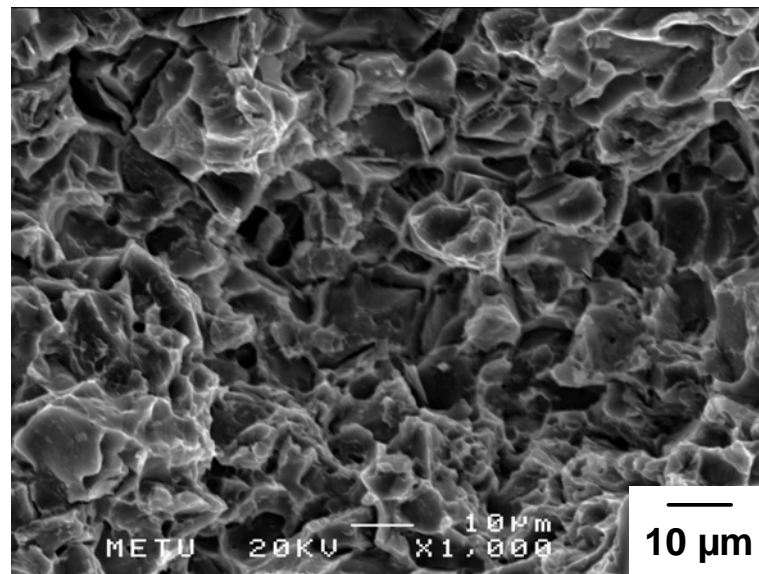


(b)

Fig. 4.38. BSE fractograph of the heat treated 30 vol.% composite, tested at a strain rate of (a)  $5 \times 10^{-3}$  and (b)  $5 \times 10^{-2} \text{ s}^{-1}$ .

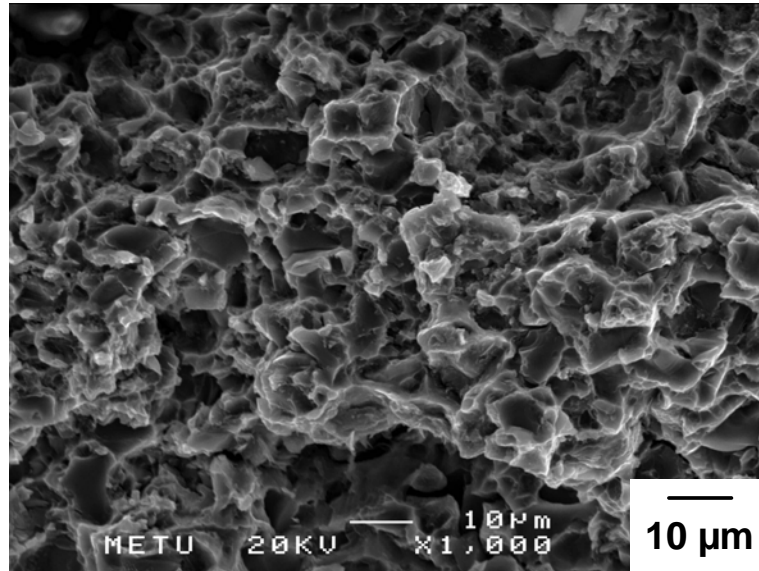


(a)

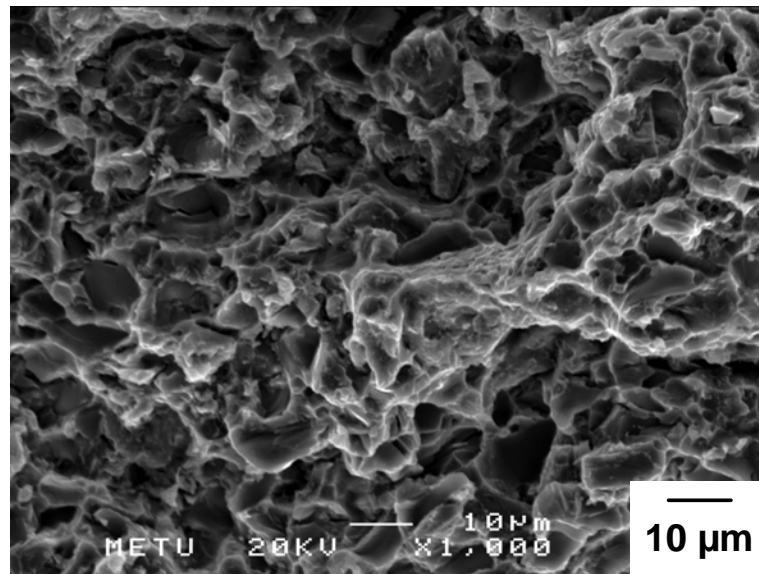


(b)

Fig. 4.39. SEI fractograph of the as fabricated 40 vol.% composite, tested at a strain rate of (a)  $5 \times 10^{-3}$  and (b)  $5 \times 10^{-2} \text{ s}^{-1}$ .



(a)



(b)

Fig. 4.40. BSE fractograph of the heat treated 40 vol.% composite, tested at a strain rate of (a)  $5 \times 10^{-3}$  and (b)  $5 \times 10^{-2} \text{ s}^{-1}$ .



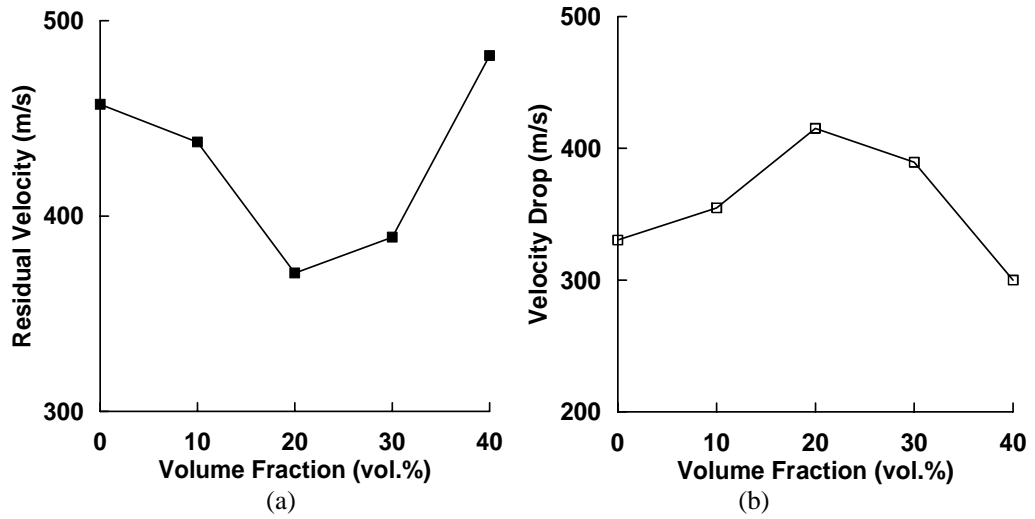


Fig. 4.41. Ballistic test results obtained by projectile residual velocity measurements: (a) Residual velocity vs. B<sub>4</sub>C volume fraction, (b) Velocity drop vs. B<sub>4</sub>C volume fraction.

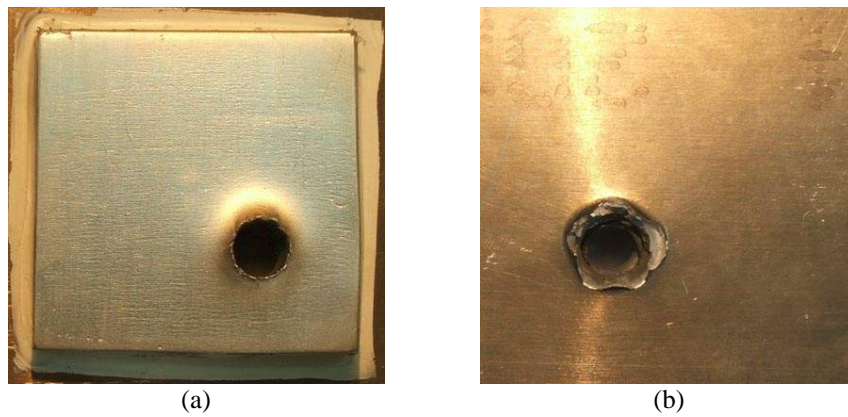
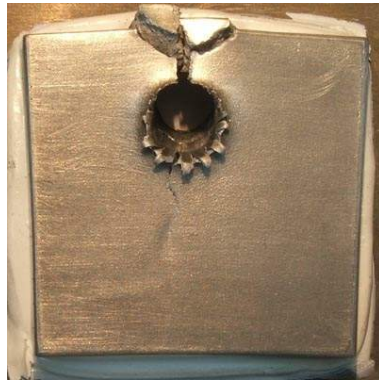


Fig. 4.42. Photograph of 10 mm Al - 4 wt.% Cu matrix alloy, backed with 6.35 mm 2024 T851 aluminum alloy after the ballistic test.

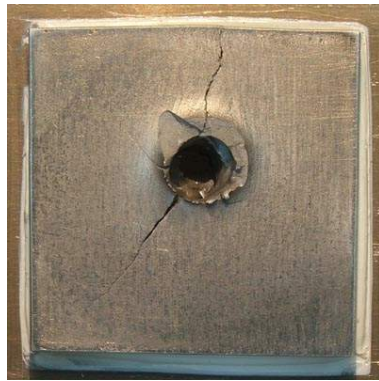


(a)

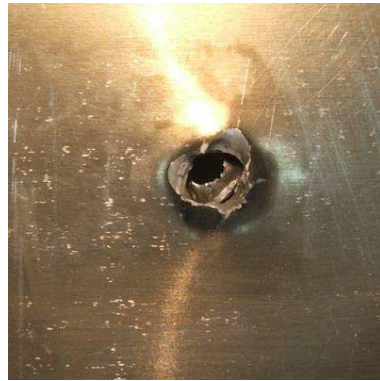


(b)

Fig. 4.43. Photograph of 10 mm 10 vol.% composite, backed with 6.35 mm 2024 T851 aluminum alloy after the ballistic test: (a) entry side, (b) exit side.



(a)



(b)

Fig. 4.44. Photograph of 10 mm 20 vol.% composite, backed with 6.35 mm 2024 T851 aluminum alloy after the ballistic test: (a) entry side, (b) exit side.



(a)



(b)

Fig. 4.45. Photograph of 10 mm 30 vol.% composite, backed with 6.35 mm 2024 T851 aluminum alloy after the ballistic test: (a) entry side, (b) exit side.

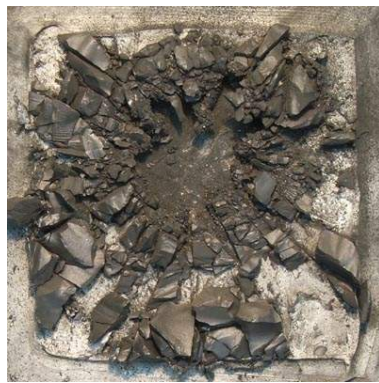


(a)



(b)

Fig. 4.46. Photograph of 10 mm 40 vol.% composite, backed with 6.35 mm 2024 T851 aluminum alloy after the ballistic test: (a) entry side, (b) exit side.



(a)



(b)

Fig. 4.47. Photograph of 10 mm hot-pressed  $B_4C$ , backed with 6.35 mm 2024-T851 aluminum alloy after the ballistic test: (a) entry side, (b) exit side.

## CHAPTER 5

### DISCUSSION

The primary aim of this thesis was to investigate the effects of aging treatment, volume fraction and strain rate on the mechanical properties of metal matrix composites (MMCs) produced by hot pressing. On another level, the ballistic performance of composite armors prepared with MMCs as facing plates were compared to ceramic armors with monolithic ceramic facing plates. The effects of aging were studied by hardness measurements, DSC analyses and TEM observations. The low strain rate and high strain rate deformation behavior of the MMCs were determined utilizing low velocity transverse rupture tests and true armor-piercing steel projectiles, respectively.

The microstructures of the composites indicated that the composites were hot pressed to near full density, with only very little porosity remaining. Higher sintering temperatures were required for the 30 vol.% and 40 vol.% B<sub>4</sub>C composites, most likely because of the necessity of a larger amount and/or increased fluidity of the liquid phase needed to fill the gaps between the B<sub>4</sub>C particles.

The matrix alloy and the composites were isothermally aged at temperatures ranging from 100°C to 175°C. When aged at either 100 or 125°C, the composites and the matrix alloy showed similar aging behaviour - a steady increase in hardness with aging time was observed (Figs. 4.5 and 4.6). The final hardness values obtained for the samples aged at 125°C were

considerably higher than those obtained at 100°C. This result indicated that the total aging time of 32 hours at 100°C was insufficient to reach peak hardness.

When the aging temperature was increased to 150°C, the MMCs with higher volume fraction of reinforcement reached peak hardness more rapidly compared to their lower volume fraction counterparts and the matrix alloy (Fig. 4.7). This “accelerated aging” effect was also observed when the aging temperature was increased further to 175°C (Fig. 4.8). The peak hardness values obtained when at the aging temperatures of 150°C and 175°C were generally lower than those obtained at 125°C.

When an MMC is quenched from the solutionizing temperature, the difference in the coefficient of thermal expansion (CTE) between the reinforcement ( $B_4C$ ) and the matrix (the Al - 4 wt.% Cu alloy) leads to large internal stresses and an enhanced dislocation density in the matrix. The enhanced dislocation density has a considerable effect on mechanical properties and aging characteristics. While these excess CTE dislocations can aid precipitation by serving as sites for heterogeneous precipitation, they can also impede precipitation by decreasing the number of quenched-in vacancies. GP zones are coherent precipitates which form at low temperatures, and their growth is controlled by the diffusion of copper atoms in the matrix.  $\theta'$  precipitates, on the other hand, are known to favor heterogeneous nucleation sites such as dislocations, for precipitation. The competition between the quenched-in vacancies and the excess CTE dislocations is thought to determine the overall aging response [61,69,75]. The CTE for pure aluminum is  $23.6 \times 10^{-6} (\text{°C})^{-1}$  where the CTE for  $B_4C$  is nearly five times smaller,  $5.3 \times 10^{-6} (\text{°C})^{-1}$  [113], indicating that CTE dislocations are very likely to occur in the  $B_4C$ -particle reinforced composites in this study. It should be noted that the number of CTE dislocations generated will greatly depend on the composite type; i.e. the matrix alloy and the reinforcement. Composites with larger differences in CTE should produce a

larger amount of CTE dislocations upon quenching from the solutionizing temperature.

Transmission electron microscopy (TEM) of the matrix alloy and the 10 vol.% B<sub>4</sub>C composite under two different heat treatments were conducted in order to understand the underlying precipitation mechanisms. Since 150°C was the critical temperature for the observed accelerated aging effect, samples aged at 125°C and 175°C were chosen for the TEM observations.

The TEM images of the composite and the unreinforced alloy aged at 125°C for 28 hours showed the presence of  $\theta'$  precipitates, varying in size (Figs. 4.10 and 4.11). The size variation of the precipitates was attributed to the fabrication route, which involves the mixing and sintering of elemental aluminum and copper powders to create the Al - 4 wt.% Cu matrix alloy. Very few dislocations were observed in the aged TEM samples; it is reported [68] that the contrast from the precipitates can be high enough to mask the dislocations present in the microstructures. The dark field image of the composite containing 10 vol.% B<sub>4</sub>C clearly showed the three perpendicular orientations of the  $\theta'$  precipitates. The existence of  $\theta'$  and its three orientations were also confirmed by SADP measurements. The precipitates appeared to have the shape of ellipses, rather than round discs. The average size of the precipitates were larger in the unreinforced alloy.

The TEM images of the matrix alloy and the 10 vol.% B<sub>4</sub>C composite aged at 175°C for 8 hours showed much smaller precipitates compared to those aged at 125°C for 28 hrs (Figs. 4.13 and 4.14). The hardness curves in Fig. 4.8 reveal that for this 8-hour aging treatment, peak hardness is only achieved in the composite containing 40 vol.% B<sub>4</sub>C reinforcement. It is therefore very likely that peak aging was not reached in the 0 vol.% and 10 vol.% B<sub>4</sub>C samples for this heat treatment. This explains why the average sizes of the precipitates were much smaller for this aging treatment. Both SADP and size measurements

indicated that the precipitates were  $\theta''$  for both specimens. Variations in size were again observed. The precipitates appeared to be only slightly larger in the composite, but much greater in number, indicating an enhanced precipitation rate.

The aging temperature of 150°C was found to be the critical temperature for the start of accelerated aging. Below 150°C, the aging curves of the matrix alloy and the composites were very similar, all showing a steady increase in hardness with aging time. The accelerated aging effect observed at the higher aging temperatures was confirmed by DSC experiments (scanned at 40°C/min). The  $\theta'$  formation temperature was approximately 50°C lower in the 40 vol.% B<sub>4</sub>C composite when compared to the matrix alloy (Fig. 4.9), which indicated accelerated precipitation in the composite. The DSC thermograms also showed a  $\theta$  formation peak at about 425°C, which was constant for all of the samples. The overlapping precipitations of the  $\theta'$  and  $\theta$  peaks prevented kinetics analyses, and increasing the heating rate (up to 100°C/min) proved to be ineffective in separating the two peaks.

The TEM micrographs occasionally showed the presence of large, undissolved  $\theta$  particles at the grain boundaries (Fig. 4.16), which indicated that full solutionization was not achieved in the samples. The incomplete solutionization was presumably caused by the use of elemental aluminum and copper powders for the fabrication of the materials. The complete dissolution of the  $\theta$  phase could have been achieved by choosing a solutionizing temperature slightly higher than the original solutionizing temperature of 515°C. The reason for not attempting higher solutionizing temperatures in this study was because of the risk of eutectic melting, which can significantly degrade the mechanical properties.

Transverse rupture tests clearly showed that the addition of B<sub>4</sub>C into the matrix resulted in a decrease in the flexural strength values (Fig. 4.17). This was

attributed simply to the angular shape of the B<sub>4</sub>C particles [114-116], which caused high stress concentrations to develop during straining. Poor particle/matrix bonding, which is common in MMCs produced by powder metallurgy methods, is another possible reason for the decreased flexural strength values. No remains of the aluminum matrix were seen on the B<sub>4</sub>C particles in the fracture surfaces (Figs. 4.23 - 4.30), which is an indication of particle/matrix debonding. Secondary electron images (SEI) of the fracture surfaces indicated that dimple fracture, involving void coalescence and growth, was the fracture mechanism for the matrix alloy (Figs. 4.31 - 4.32). In the composites, interface decohesion and particle cracking were additional mechanisms contributing to fracture (Figs. 4.33 - 4.40).

The flexural strength plots showed that the strength of the composites and the unreinforced alloy were greatly improved by heat treatment. Backscattered electron (BSE) micrographs of the fracture surfaces of the as-fabricated samples showed the presence of copper rich particles, which presumably belonged to the  $\theta$  phase. The BSE fractographs also showed regions lacking reinforcement, which were most likely due to through the incoherent  $\theta$  particles. The BSE fractographs of the heat treated samples, however, showed a more uniform distribution of B<sub>4</sub>C particles on the fracture surface (compare Figs. 4.29 and 4.30). During the solutionizing treatment, the existing  $\theta$  phase was dissolved along with other microstructural heterogeneities, and the following aging treatment resulted in a fine distribution of precipitates which were mostly coherent with the matrix, and strength was thus increased [74]. The heat treated composites also exhibited a more uniform distribution of B<sub>4</sub>C particles on the fracture surface, indicating that crack propagation in the peak aged samples occurred through the matrix/reinforcement interface, rather than the copper-rich particles.

Strain rate affected the flexural response for all of the materials, especially those with higher B<sub>4</sub>C volume fractions. A slight increase in flexural strength



followed by a decrease at higher ( $10^{-2} \text{ s}^{-1}$ ) strain rates was observed for all of the samples studied (Figs. 4.18 and 4.19). At strain rates higher than  $10^{-2} \text{ s}^{-1}$  all samples showed negative strain rate sensitivity, regardless of  $\text{B}_4\text{C}$  content. Because the unreinforced alloy also shows similar characteristics, the negative strain rate sensitivity cannot be attributed only to the presence of  $\text{B}_4\text{C}$  reinforcement.

The wrought 2024-T851 alloy showed higher flexural strength values than the heat treated matrix alloy and the composites (Fig. 4.20). Modification of the precipitates by the additional alloying elements was one of the reasons for its improved strength. The applied T851 temper, which included the steps of solutionizing, cold working, stress-relief stretching, and artificial aging, is also another reason for the differences in strength.

Only few studies exist regarding the effect of strain rate on mechanical behavior of discontinuously reinforced MMCs. In wrought and cast alloy systems it is generally observed that the strength increases with increasing the strain rate. For powder metallurgy systems - especially those involving MMCs, the effect of strain rate remains poorly understood [117,118]; and inconsistencies in strength with increasing strain rate have been widely reported [119-120].

Most studies conducted on monolithic materials at quasi-static strain rates indicate a positive strain rate sensitivity, i.e. an increase in strength with increasing strain rate, which is usually attributed to the thermally activated mechanisms governing dislocation glide. However for MMCs the effect of strain rate is not clear. While many studies indicate strain rate hardening similar to monolithic materials [122-124], there are other studies which show negative strain rate sensitivity [117,125]. Negative strain rate sensitivity is often attributed to dynamic strain aging, which is caused by the presence of fast-diffusing solute atoms interacting with dislocations. The strain rates

chosen for flexural strength tests in this study were all in the quasi-static range, and well below impact strain rates (that are usually of the order of  $10^3 \text{ s}^{-1}$ ). The primary cause for the decrease in strength with increasing strain rate in this study is believed to be not only due to fast-diffusing solute atoms, but also possibly due to entrapped oxides. The 30 vol.% and 40 vol.%  $\text{B}_4\text{C}$  composites showed particularly low flexural strength values at the higher strain rates. Increased  $\text{B}_4\text{C}$  particle fracture and/or decohesion along the reinforcement/matrix interface may have also played part in the fracture of these materials at the higher strain rates. The fracture surfaces at high strain rates however did not show apparent difference compared with those at low strain rates.

The ballistic test results in Fig. 4.41 showed that among the MMC composite armors tested, the 20 vol.%  $\text{B}_4\text{C}$  composite was most effective in decreasing the velocity of the armor-piercing (AP) projectile. The photographs of the impacted matrix alloy (Fig. 4.42) and MMC armors (Figs. 4.43 - 4.46) showed signs of petaling and ductile hole growth, especially in the matrix alloy and the 10 vol.%  $\text{B}_4\text{C}$  composite. In the composites containing 20 vol.%  $\text{B}_4\text{C}$  and more, radial cracking was additionally observed. Fragmentation of the petals, especially in the higher volume fraction composites, appears to have occurred, due to the high tensile stresses generated during perforation. It was clear from the ballistic tests that the P/M matrix and its composites were not ideal as facing plates against armor-piercing projectiles. The Al - 4 wt.% Cu matrix was clearly not strong enough to resist the 62 HRC penetrator and was easily deformed by shear, irrespective of  $\text{B}_4\text{C}$  volume fraction. The photograph of the perforated 20 vol.%  $\text{B}_4\text{C}$  composite in Fig. 4.44(a) showed that the matrix was still capable of stopping radial crack propagation. In the 30 vol.% and 40 vol.%  $\text{B}_4\text{C}$  composites, the radial cracks traversed through the entire thickness of the composite plate, resulting in the failure of the facing plate. The results obtained from the ballistic tests were in agreement with the results of the quasistatic flexural strength tests, in which the 30 vol.% and 40 vol.%  $\text{B}_4\text{C}$  composites

both showed low flexural strength values at the highest strain rates. Increased matrix/particulate decohesion and particle cracking are the most likely causes for the observed through-thickness cracks.

The only armor capable of stopping the AP projectile was the B<sub>4</sub>C ceramic armor. Fig. 4.47 showed that conoid formation in ceramic facing plates [93,98] has a very important role in the stopping of the AP projectile. The conoid that formed at the moment of impact distributed the load to a greater area on the backing material, and hence increased the absorbed energy. Conoid formation is generally observed in very brittle materials such as ceramics, and is due to Hertzian stresses generated during impact. A relatively large amount of bulging was detected on the backing plate of the B<sub>4</sub>C ceramic armor, confirming conoid formation. The P/M matrix alloy and its composites, containing a very ductile matrix, were deformed easily, and ductile hole growth was the governing mechanism. Ceramic fracture and fragmentation [89,97,126] is also considered as another effective mechanism in absorbing the energy of the projectile. This mechanism was also less effective in the the composites, due to the high ductility of the metal matrix.

## CHAPTER 6

### CONCLUSIONS

In view of the studies carried out, the following conclusions can be drawn:

- 1) The conventional hot pressing method was effective in producing substantially pore-free microstructures for both the Al - 4 wt.% Cu matrix alloy and its B<sub>4</sub>C containing composites.
- 2) The kinetics of aging of the Al - 4 wt.% Cu matrix was found to depend very sensitively on the aging temperature. Higher hardness values were obtained by using lower aging temperatures in the MMCs. The highest hardness attained was 193 HV in the 40 vol.% B<sub>4</sub>C composite after ageing at 125°C for 28 hours.
- 3) Accelerated aging was observed in the higher volume fraction composites at aging temperatures of 150°C and above. This result was confirmed by DSC analyses.
- 4) The TEM micrographs showed precipitates of  $\theta'$  type, for the samples isothermally aged at 125°C and for 28 hours and precipitates of  $\theta''$  type, for the samples aged at 175°C for 8 hours. Some undissolved  $\theta$  particles were also observed, indicating incomplete dissolution of the  $\theta$  phase during solutionization.
- 5) The flexural strength values for the composites decreased with increasing volume fraction of B<sub>4</sub>C reinforcement. This was believed to be due to high

stress concentrations occurring at the interface between the matrix and the sharp, angular B<sub>4</sub>C particles during straining. The highest flexural strength value recorded was 887 MPa for the matrix alloy at a strain rate of  $5 \times 10^{-3} \text{ s}^{-1}$ .

6) The flexural strength of the matrix alloy and its composites were greatly improved by heat treatment. In the quasi-static range ( $5 \times 10^{-4} \text{ s}^{-1}$  to  $5 \times 10^{-2} \text{ s}^{-1}$ ), strain rate had little effect on flexural strength. The flexural strength of the matrix alloy and the composite increased with increasing strain rate up to  $10^{-2} \text{ s}^{-1}$  after which it decreased. Entrapped oxides and B<sub>4</sub>C fracture were thought to be the cause of the decrease in flexural strength at high strain rates. A wrought 2024-T851 aluminum alloy tested at identical conditions did not show a decrease in flexural strength with increasing strain rate.

7) Fracture along copper-rich phases was evident in the as-fabricated samples which additionally exhibited reinforcement-free regions in their fractographs. Dimple fracture, involving void coalescence and growth, was the fracture mechanism for the matrix alloy and the composites, regardless of heat treatment. In the composites, additional mechanisms contributing to fracture were interface decohesion and particle cracking.

8) Powder metallurgy composites of the Al - 4 wt.% Cu alloy, produced by the conventional hot pressing method, were not found to be suitable candidates as facing plates for laminated composite armors. Their ballistic performance was inferior to that of hot-pressed B<sub>4</sub>C. Deformation in the MMCs predominantly occurred by the shearing of the metal matrix, which was additionally assisted by reinforcement fracture and interface debonding.

9) The only armor configuration capable of stopping the armor-piercing projectile was the hot-pressed B<sub>4</sub>C ceramic armor. For this armor, conoid formation, ceramic fracture and fragmentation played an important role in decreasing the velocity of the projectile. The ceramic facing plate was however

greatly damaged by fragmentation. In order to increase the multi-hit capability of the  $B_4C$  ceramic armor, a spall shield capable of providing structural integrity could be designed in the future.

## REFERENCES

- [1] Mazumdar, S.K., 2002. *Composites Manufacturing: Materials, Product, and Process Engineering*, CRC Press, Boca Raton.
  
- [2] Chawla, K.K., 1987. *Composite Materials*, Socorro, New Mexico.
  
- [3] Shwartz, M.M., 1984. *Composite Materials Handbook*, McGraw-Hill, New York.
  
- [4] Ed. Davis, J.R., 1993. "Aluminum Matrix Composites" in *Aluminum and Aluminum Alloys*, ASM Specialty Handbook, pp. 160-179, ASM Int., Ohio.
  
- [5] Terry, B., and Jones, G., 1990. *Metal Matrix Composites: Current Developments and Future Trends in Industrial Research and Applications*, Elsevier, Oxford.
  
- [6] Clegg, A.J., 1991. Cast metal matrix composites, *Foundryman*, pp. 314-319.
  
- [7] Srivatsan, T.S., Ibrahim I.A., Mohamed, F.A., Lavernia, E.J., 1991. Processing techniques for particulate-reinforced metal aluminum matrix composites, *J. Mater. Sci.*, 26, pp. 5965-5978.
  
- [8] Ray, S., 1993. Synthesis of cast metal matrix particulate composites, *J. Mater. Sci.*, 28, pp. 5397-5413.

- [9] Rohatgi, P., 1988. "Cast Metal Matrix Composites" in *Metals Handbook*, Vol. 15, pp. 840-854, ASM Int., Ohio.
- [10] Cornie, J.A., Chiang, Y.M., Uhlmann, D.R., Mortensen, A. and Collins, J.M., 1986. Processing of metal and ceramic matrix composites, *Am. Ceram. Soc. Bull.*, 65, pp. 293-297.
- [11] Lloyd, D.J., 1994. Particle reinforced aluminum and magnesium matrix composites, *Int. Mater. Rev.*, 39, pp. 1-23.
- [12] Pickens, J.R., 1981. Aluminum powder metallurgy technology for high-strength applications, *J. Mater. Sci.*, 16, pp. 1437-1457.
- [13] Tan, M.J., and Zhang, X., 1998. Powder metal matrix composites: selection and processing, *Mater. Sci. Eng.*, 244, pp. 80-85.
- [14] Banerji, A., Rohatgi, P.K. and Reif, W., 1984. Role of wettability in the preparation of metal matrix composites, *Metall*, 38, pp. 656-661.
- [15] Mortensen, A. and Jin, I., 1992. Solidification processing of metal matrix composites, *Int. Mater. Rev.*, 37, pp. 101-128.
- [16] Rohatgi, P.K., Asthana, R. and Das, S., 1986. Solidification, structures, and properties of cast metal-ceramic composites, *Int. Mater. Rev.*, 31, pp. 115-139.
- [17] Delannay, F., Froyen, L. and Deruyttere, A., 1987. The wetting of solids by molten metals and its relation to the preparation of metal matrix composites, *J. Mater. Sci.*, 22, pp. 1-16.



- [18] Howe, J.M., 1993. Bonding, structure and properties of metal/ceramic interfaces - part 1: chemical bonding, reaction and interfacial structure, *Inter. Mater. Rev.*, 38, pp. 233-256.
- [19] Lin, R.Y., 1993. Composite interfacial reactions, *JOM*, 45, p. 20.
- [20] Arsenault R.J. and Shi, N., 1986. Dislocation generation due to differences in coefficients of thermal expansion, *Mater. Sci. Eng.*, 81, pp. 175-187.
- [21] Derby, B. and Walker, J.R., 1988. The role of enhanced matrix dislocation density in strengthening metal matrix composites, *Scripta Metall.*, 22, pp. 529-532.
- [22] Kamat, S.V., Rollett, A.D. and Hirth J.P., 1991. Plastic deformation in alloy matrix-alumina particulate composites, *Scripta Metall. Mater.*, 25, pp. 27-32.
- [23] Taya, M. Lulay, K.E., and Lloyd, D.J., 1991. Strengthening of a particulate MMC by quenching, *Acta Metall. Mater.*, 39, pp. 73-87.
- [24] Gustafson, T.W., Panda, P.C., Song, G., and Raj, R., 1997. Influence of microstructural scale on plastic flow behavior of metal matrix composites, *Acta Mater.*, 45, pp. 1633-1643.
- [25] Lee, J., Kim, N.J., Jung, J.Y., Lee, E-S., and Ahn, S., 1998. The influence of reinforced particle fracture on strengthening of spray formed Cu-TiB<sub>2</sub> composite, *Scripta Metall. Mater.*, 1998, 39, pp. 1063-1069.
- [26] Christman T., Needleman, A., and Suresh, S., 1989. An experimental and numerical study of deformation in metal ceramic composites, *Acta Metall.*, 37, pp. 3029-3050.

- [27] Bao, G., Hutchinson, J.W., McMeeking, R.M., 1991. Particle reinforcement of ductile matrices against plastic-flow and creep, *Acta Metall. Mater.*, 39, pp. 1871-1882.
- [28] Shi, N., Bourke, M.A.M., Roberts, J.A. and Allison, J.E., 1997. Phase-stress partition during uniaxial tensile loading of a TiC-particulate-reinforced Al composite, *Metall. Mater. Trans.*, 28A, pp. 2741-2753.
- [29] Arsenault, R. J. and Taya, M., 1987. Thermal residual stress in metal matrix composite, *Acta Metall.*, 35, pp. 651-659.
- [30] Starink, M.J., and Syngellakis, S., 1999. Shear lag models for discontinuous composites: fibre end stresses and weak interface layers, *Mater. Sci. Eng.*, 270, pp. 270-277.
- [31] Yang, J., Pickard, S.M., Cady, C., Evans, A.G., and Mehrabian, R., 1991. The stress-strain behavior of aluminum matrix composites with discontinuous reinforcements, *Acta Metall. Mater.*, 39, pp. 1863-1869.
- [32] Llorca, J., Needleman, A., and Suresh, S., 1991. An analysis of the effects of matrix void growth on deformation and ductility in metal-ceramic composites, *Acta Metall. Mater.*, 39, pp. 2317-2335.
- [33] Bao, G. and Lin, Z., 1996. High strain rate deformation in particle reinforced metal matrix composites, *Acta Mater.*, 44, pp. 1011-1019.
- [34] Majumdar, B.S. and Pandey, A.B., 2000. Deformation and fracture of particulate reinforced aluminum alloy composites: part II, modeling, *Metall. Trans.*, 31A, pp. 937-950.

- [35] González, C. and Llorca, J., 2000. A Self-Consistent Approach to the Elasto-Plastic Behaviour of Two-Phase Materials Including Damage, *J. Mech. Phys. Solids*, 48, pp. 675-692.
- [36] Mummery P. and Derby B., 1991. The influence of microstructure on the fracture behavior of particulate metal matrix composites, *Mater. Sci. Eng.*, 135, pp. 221-224.
- [37] Miller W.S., Humphreys F.J., 1991. Strengthening mechanisms in particulate metal matrix composites, *Scripta Metall. Mater.*, 25, pp. 33-38.
- [38] Aikin, R.M., and Christodoulou, L., 1991. The role of equiaxed particles on the yield stress of composites, *Scripta Metall. Mater.*, 25, pp. 9-14.
- [39] Prangnell P.B., Downes T., Stobbs W.M., and Withers P.J., 1994. The deformation of discontinuously reinforced MMCs - I: The initial yielding behaviour, *Acta Metall. Mater.*, 42, pp. 3425-3436.
- [40] Kouzeli, M., Weber, L., SanMarchi, C., and Mortensen, A., 2001. Quantification of microdamage phenomena during tensile straining of high volume fraction particle reinforced aluminium, *Acta Mater.*, 49, pp. 497-505.
- [41] Nan, C.W. and Clarke, D.R., 1996. The influence of particle size and particle fracture on the elastic/plastic deformation of metal-matrix composites, *Acta mater.*, 44, pp. 3801-3811.
- [42] Nan, C.W., Birringer, R., and Gleiter H., 1997. On the effect of particle size distribution on the elastic/plastic deformation of metal-matrix composites, *Scripta Mater.*, 37, pp. 969-976.

- [43] Ramakrishnan, N., 1996. An analytical study on strengthening of particulate reinforced metal matrix composites, *Acta Mater.*, 44, pp. 69-77.
- [44] Cleveringa, H.H.M., Van der Giessen, E. and Needleman, A., 1997. Comparison of discrete dislocation and continuum plasticity predictions for a composite material, *Acta Mater.*, 45, pp. 3163-3179.
- [45] Kim, H.S., Bush, M. and Estrin, Y., 2000. A phase mixture model of a particle reinforced composite with fine microstructure, *Mater. Sci. Eng.*, 276, pp. 175-185.
- [46] Fleck, N.A., Muller, G.M., Ashby, M.F. and Hutchinson, J.W., 1994. Strain gradient plasticity: theory and experiment, *Acta Metall. Mater.*, 42, pp. 475-487.
- [47] Nix, W.D. and Gao, H., 1998. Indentation size effects in crystalline materials: a law for strain gradient plasticity, *J. Mech. Phys. Solids*, 46, pp. 411-425.
- [48] Gao, H., Huang, Y., Nix, W.D., and Hutchinson, J.W., 1999. Mechanism-based strain gradient plasticity - I. Theory, *J. Mech. Phys. Solids*, 47, pp. 1239-1263.
- [49] Huang, Y., Gao, H., Nix, W.D., and Hutchinson, J.W., 2000. Mechanism-based strain gradient plasticity - II. Analysis, *J. Mech. Phys. Solids*, 48, pp. 99-128.
- [50] Chen, S.H. and Wang, T.C., 2000. A new hardening law for strain gradient effect, *Acta Mater.*, 48, pp. 3997-4005.

- [51] Shi, M.X., Huang, Y. and Hwang, K.C., 2000. Plastic flow localization in mechanism-based strain gradient plasticity, *Int. J. Mech. Sci.*, 42, pp. 2115-2131.
- [52] Duan, D.M., Wu, N.Q., Slaughter, W.S. and Mao, S.X., 2001. Length scale effect on mechanical behavior due to strain gradient plasticity, *Mater. Sci. Eng.*, 303, pp. 241-249.
- [53] Dai, L.H., Ling, Z. and Bai, Y.L., 1999. A strain gradient strengthening law for particle reinforced metal matrix composites, *Scripta Mater.*, 41, pp. 245-251.
- [54] Tomita, Y., Higa, Y., and Fujimoto, T., 2000. Modeling and estimation of deformation behavior of particle reinforced metal-matrix composite, *Int. J. Mech. Sci.*, 42, pp. 2249-2260.
- [55] Murray, J.L., 1985. The aluminum-copper system, *Int. Metall.Rev.*, 30, pp. 221-233.
- [56] Eds. Massalski, T.B. et al., 1990. *Binary Alloy Phase Diagrams*, ASM International, Ohio.
- [57] Varley, P.C., 1970. *The Technology of Aluminium and its Alloys*, CRC Press, Ohio.
- [58] Martin, J.W., 1968. *Precipitation Hardening*, Pergamon, Oxford.
- [59] Ed. Van Horn, K.R., 1967. *Aluminum*, American Society for Testing Metals, Ohio.

- [60] Polmear, I.J., 1989. *Light Alloys: From Traditional Alloys to Nanocrystals*, 1989, Elsevier, Oxford.
- [61] Auvray, X., Geogopoulos, P., and Cohen, J.B., 1981. The structure of G.P. I zones in Al - 1.7 at.% Cu, *Acta Metall.*, 29, pp. 1061-1075.
- [62] Ashby, M.F., and Jones, D.R.H., 1999. *Engineering Materials 2: An Introduction to Microstructures, Processing and Design*, Butterworth-Heinemann, Oxford.
- [63] Taylor, A. and Kagle, B.J., 1963. *Crystallographic Data on Metal and Alloy Structures*, Dover, New York.
- [64] Chawla, K.K., and Metzger, M., 1972. Initial dislocation distributions in tungsten fiber-copper composites, *J. Mater. Sci.*, 7, pp. 34-39.
- [65] Vogelsang, M., Arsenault, R.J. and Fisher, R.M., 1986. An *in situ* HVEM study of dislocation generation at Al/SiC interfaces in metal matrix composites, *Metall. Trans.*, 17A, pp. 379-389.
- [66] Papazian, J.M., 1988. Effects of SiC whiskers and particles on precipitation in aluminum matrix composites, *Metall. Trans.*, 19A, pp. 2945-2953.
- [67] Christman, T., and Suresh, S., 1988. Microstructural development in an aluminum alloy-SiC whisker composite, *Acta Metall.*, 37, pp. 1691-1704.
- [68] Dutta, I., and Bourell, D.L., 1989. A theoretical and experimental study of aluminum alloy 6061-SiC matrix composite to identify the operative mechanism for accelerated aging, *Mater. Sci. Eng.*, 112, pp. 67-77.

- [69] Suresh, S., Christman, T., and Sugimura, Y., 1989. Accelerated aging in cast Al alloy-SiC particulate composites, *Scr. Metall.*, 23, pp. 1599-1602.
- [70] Chawla, K.K., Esmaceli, A.H., Datye, A.K., and Vasuvedan, A.K., 1991. Effect of homogeneous/heterogeneous precipitation on aging behavior of SiC<sub>p</sub>/Al 2014 composite, *Scr. Metal. Mater.*, 25, pp. 1315-1319.
- [71] Lin, J-S., Li, P-X., and Wu, R-J., 1993. Aging evaluation of cast particulate-reinforced SiC/Al(2024) composites, *Scr. Metal. Mater.*, 28, pp. 281-286.
- [72] Thomas, M.P., and King, J.E., 1994. Comparison of the aging behavior of PM 2124 alloy and Al-SiC<sub>p</sub> metal matrix composite, *J. Mater. Sci.*, 29, pp. 5272-5278.
- [73] Dutta, I., Harper, C.P. and Dutta, G., 1994. Role of Al<sub>2</sub>O<sub>3</sub> particulate reinforcements on precipitation in 2014 Al-matrix composites, *Metall. Mater. Trans.*, 25A, pp. 1591-1602.
- [74] Dutta, B., and Surappa, M.K., 1995. Age-hardening behaviour of Al-Cu-SiC<sub>p</sub> composites synthesized by the casting route, *Scr. Metall. Mater.* 32, pp. 731-736.
- [75] Badini, C., Marino, F. and Verné, E., 1995. Calorimetric study on the precipitation path in 2024 alloy and its SiC composite, *Mater. Sci. Eng.*, 191, pp. 185-191.
- [76] Sannino, A.P., and Rack, H.J., 1995. Effect of reinforcement size on the age hardening of PM 2009 Al-SiC 20 vol % particulate composites, *J. Mater. Sci.*, 30, pp. 4316-4322.

- [77] Janowski, G.M. and Pletka B.J., 1995. The effect of particle size and volume fraction on the aging behavior of a liquid phase sintered SiC/aluminum composite, *Metall. Mater. Trans.*, 26A, pp. 3027-3035.
- [78] Shakesheff, A.J., 1995. Aging and toughness of silicon carbide particulate reinforced Al-Cu and Al-Cu-Mg based metal-matrix composites, *J. Mater. Sci.*, 30, pp. 2269-2276.
- [79] Parrini, L. and Schaller, R., 1995. Cu precipitation in AlCu-Al<sub>2</sub>O<sub>3</sub> metal matrix composites, *Acta Metall. Mater.*, 43, pp. 2149-2156.
- [80] Chen, K.C., and Chao, C.G., 1995. Effect of  $\delta$  alumina fibers on the aging characteristics of 2024- based metal-matrix composites, *Metall. Mater. Trans.*, 26A, pp. 1035-1043.
- [81] Massardier, V., Pelletier, L., and Merle, P., 1998. Influence of the introduction of ceramic particles in Al-Cu alloys on GP zone formation, *Mater. Sci. Eng.*, 249, pp. 121-133.
- [82] Massardier, V. and, Merle, P., 1998. Mechanisms of interaction controlling the kinetics of zone formation in metal matrix composites: comparison of the effect of the reinforcement in Al-Cu and Al-Mg-Si matrix composites, *Mater. Sci. Eng.*, 249, pp. 109-120.
- [83] Zhou, J., and Duszcyk, J., 1999. Aging response of an AA2014-based composite prepared from an elemental powder mixture, *J.Mater.Sci. Lett.*, 18, pp. 1111-1113.
- [84] Varma, S.K., Salas, D., Corral, E., Esquivel, E., Chawla, K.K., and Mahapatra, R., 1999. Microstructural Development during aging of 2014 aluminum alloy composite, *J. Mater. Sci.*, 34, pp. 1855-1863.



- [85] Miserez, A., Stücklin, S., Rossol, A., San Marchi, C. and Mortensen, A., 2002. Influence of heat treatment and particle shape on mechanical properties of infiltrated Al<sub>2</sub>O<sub>3</sub> particle reinforced Al–2 wt.-% Cu, *Mat. Sci. Tech.*, 18, pp. 1461-1470.
- [86] Longtao, J., Min, Z., Gaohui, W., and Qiang, Z., 2005. Aging behavior of sub-micron Al<sub>2</sub>O<sub>3</sub>p/2024Al composites, *Mater. Sci. Eng.*, 392, pp. 366-372.
- [87] Ashby, M.F., 1993. Criteria for selecting the components of composites, *Acta Metall. Mater.*, 41, pp. 1313-1335.
- [88] Hull, D., 1981. *An Introduction to Composite Materials*, Cambridge University Press, Cambridge.
- [89] Kelly, A., and Macmillan, N.H., 1986. *Strong Solids*, Oxford University Press, Oxford.
- [90] Taya, M., and Arsenault, R.J., 1989. *Metal Matrix Composites: Thermomechanical Behaviour*, Pergamon Press, Oxford.
- [91] Ibrahim, I.A., Mohamed, F.A., and Lavernia, E.J., 1991. Particulate reinforced metal matrix composites - a review, *J. Mater. Sci.*, 26, pp. 1137-1156.
- [92] Budiansky, B., 1970. Thermal and thermoelastic properties of isotropic composites, *J. Comp. Mater.*, 4, pp. 286-295.
- [93] Rosen, B.W. and Hashin, Z., 1970. Effective thermal expansion coefficients and specific heats of composite materials, *Int. J. Eng. Sci.*, 8, pp. 157-173.

- [94] Turner, P.S., 1946. Thermal-expansion stresses in reinforced plastics, *J. Res. NBS*, 37, pp. 239-250.
- [95] Hashin, Z., and Shtrikman, S., 1962. A variational approach to the theory of the effective magnetic permeability of multiphase materials, *J. Appl. Phys.*, 33, pp. 3125-3131.
- [96] Miracle, D.B., 2005. Metal matrix composites - from science to technological significance, *Comp. Sci. Tech.*, 65, pp. 2526-2540.
- [97] Ogorkiewicz, R.M., 1976. Composite armor, *Composites*, 7, pp. 71-72.
- [98] Wilkins, M.L., 1978. Mechanics of penetration and perforation, *Int. J. Eng. Sci.*, 16, pp. 793-807.
- [99] Eds. James W. McCauley et al., 2002. "The Effect of Metal-Ceramic Bonding on Ballistic Impact" in *Ceramic Armor Materials by Design*, pp. 635-642, , American Ceramic Society, Ohio.
- [100] Hetherington, J.G., 1992. The optimization of two component composite armors, *Int. J. Impact Eng.*, 12, pp. 409-414.
- [101] Chin, E.S.C., 1999. Army focused research team on functionally graded armor composites, *Mat. Sci. Eng.*, A259, pp. 155-161.
- [102] Roeder, B.A., and Sun, C.T., 2001. Dynamic penetration of alumina/aluminum laminates: experiments and modeling, *Int. J. Impact Eng.*, 25, pp. 169-185.
- [103] O'Donnell, R.G., 1991. An investigation of the fragmentation behaviour of impacted ceramics, *J. Mater. Sci. Lett.*, 10, pp. 685-688.

- [104] Eds. James W. McCauley et al., 2002. “An Overview of Ceramic Armor Applications” in *Ceramic Armor Materials by Design*, pp. 3-21, American Ceramic Society, Ohio.
- [105] Eds. James W. McCauley et al., 2002. “Armor Ceramics under High-velocity Impact of a Medium-caliber Long-rod Penetrator” in *Ceramic Armor Materials by Design*, pp. 23-31, American Ceramic Society, Ohio.
- [106] Eds. James W. McCauley et al., 2002. “Practical Issues in Ceramic Armor Design” in *Ceramic Armor Materials by Design*, pp. 33-44, American Ceramic Society, Ohio.
- [107] Mayselles, M., 1987. Impact on ceramic targets, *J. Appl. Mech.*, 54, pp. 373-378.
- [108] International Organisation for Standardisation, 1992. *ISO Standards Handbook 31: Mechanical Testing of Metallic Materials*, ISO, Geneva.
- [109] Fenner, A.J., 1965. *Mechanical Testing of Materials*, Pilosophical Library, New York.
- [110] Liddicoat, R.T. and Potts, P.O., 1952. *Laboratory Manual of Materials Testing*, Macmillan, New York.
- [111] Everett, F.L., 1941. *Mechanical Properties of Materials*, University Lithoprinters, Michigan.
- [112] Alpay, S.P., and Gürbüz, R., 1993. *MET.E.316 Laboratory Manual*, METU, Ankara.

- [113] Hutchings, I.M., 1992. *Tribology: Friction and Wear of Engineering Materials*, CRC, Boca Raton.
- [114] Song, S. G., Shi, N., Gray III, G. T. and Roberts, J. A., 1996. Reinforcement shape effects on the fracture behavior and ductility of particulate-reinforced 6061-Al matrix composites. *Metall. Mater. Trans.*, 27A, pp. 1543-1940.
- [115] Poole, W.J. and Dowdle, E.J., 1998. Experimental measurements of damage evolution in Al-Si eutectic alloys, *Scripta Mater.*, 39, pp. 1281-1287.
- [116] Brechet, Y., Embury, J.D. and Tao, S., 1991. Damage initiation in metal matrix composites, *Acta Metall. Mater.* ,39, pp. 1781-1786.
- [117] Zhang, H., Ramesh, K.T. and Chin, E.S.C., 2004. High strain rate response of aluminum 6092/B<sub>4</sub>C composites, *Mater. Sci. Eng.*, 384, pp. 26-34.
- [118] Li,Y. and Ramesh, K.T., 1998. Influence of particle volume fraction, shape, and aspect ratio on the behavior of particle-reinforced metal-matrix composites at high rates of strain, *Acta Mater.*, 46, pp. 5633-5646.
- [119] Perng, C.C., Hwang, J.R. and Doong, J.L., 1993. High strain rate tensile properties of Al<sub>2</sub>O<sub>3</sub>p/6061-T6 metal matrix composite, *Mater. Sci. Eng.*, 171, pp. 213-221.
- [120] Lou, B.Y. and Huang, J.C., 1996. Failure Characteristics of 6061/Al<sub>2</sub>O<sub>3</sub> and 2014/Al<sub>2</sub>O<sub>3</sub> Composites as a Function of Loading Rate, *Metall. Mater. Trans.*, 27A, pp. 3095-3107.

- [121] Li, Y., Ramesh, K.T., and Chin, E.S.C. 2000. Viscoplastic deformations and compressive damage in an A359/SiCp metal matrix composite. *Acta Mater.* 48, pp. 1563-1573.
- [122] Li, Y., Ramesh, K.T. and Chin E.S.C., 2004. Comparison of the plastic deformation and failure of A359/SiC and 6061-T6/Al<sub>2</sub>O<sub>3</sub> metal matrix composites under dynamic tension, *Mater. Sci. Eng.*, A371, pp. 359-370.
- [123] Guden, M., and Hall, I.W., 1998. Dynamic properties of metal matrix composites: a comparative study, *Mater. Sci. Eng.*, A242, pp. 141-152.
- [124] Yadav, S., Chichili, D.R. and Ramesh, K.T., 1995. The mechanical properties of a 6061-T6 Al/Al<sub>2</sub>O<sub>3</sub> metal-matrix composite at high rates of deformation, *Acta Metall. Mater.*, 43, pp. 4453-4464.
- [125] Zhang, H., Chen, M.W., Ramesh, K.T., Ye, J., Schoenung, J.M. and Chin, E.S.C., 2006. Tensile behavior and dynamic failure of aluminum 6092/b<sub>4</sub>c composites. *Mater. Sci. Eng.*, 433, pp. 70-82.
- [126] Woodward, R.L., Gooch, W.A., O'Donnell, R.G., Perciball, W.J., Baxter, B.J., and Pattie, S.D., 1994. A study of fragmentation in the ballistic impact of ceramics, *Int. J. Impact Engng.*, 15, pp. 605-618.

## CURRICULUM VITAE

### PERSONAL INFORMATION

Surname, Name: Karakaş, Mustafa Serdar  
Nationality: Turkish (TC)  
Date and Place of Birth: 30 December 1977, Ankara  
Marital Status: Single  
Phone: +90 312 210 59 24  
Fax: +90 312 210 25 18  
email: skarakas@metu.edu.tr

### EDUCATION

Degree	Institution	Year of Graduation
MS	Istanbul Technical University Metallurgical and Materials Engineering	2001
BS	Istanbul University Metallurgical Engineering	1999
High School	Antalya Anadolu High School, Antalya	1995

### WORK EXPERIENCE

Year	Place	Enrollment
2001-2007	METU Department of Metallurgical and Materials Engineering	Research Assistant
1998	ETI Electrometallurgy Company	Intern Engineering Student

### FOREIGN LANGUAGES

Advanced English, Intermediate French, German and Arabic

### PUBLICATIONS

1. Ahlatci, H., Karakaş, S., Candan, E. and Çimenoglu, H., "Effect of Magnesium Addition on the Wear Behaviour of Al-70 vol.%Al<sub>2</sub>O<sub>3p</sub> Composites", Mater. Sci. Tech., 19, 949-954 (2003).
2. Karakaş, S., Yıldırım, O., Ögel, B., "Kompozit Zırhlara Genel Bakış ve Alüminyum/Bor Karbür Zırhlarının Üretimi", Zırh Teknolojileri Semineri Bildiriler Kitabı, 10-11 Mart 2005, MSB ARGE ve Tekno.D.Bşk.lığı, Ankara, 134-144 (2005).
3. Karakaş, M.S., Acır, A., Übeyli, M. and Ögel, B., "Effect of Cutting Speed on Tool Performance in Milling of B<sub>4</sub>C<sub>p</sub> reinforced aluminum metal matrix composites", J. Mater. Process. Technol., 178, 241-246 (2006).

### HOBBIES

Photography, Movies, Computing, Chess